The Hybrid Monopile

Design of a novel foundation structure for large offshore wind turbines in intermediate water depths

Master of Science Thesis

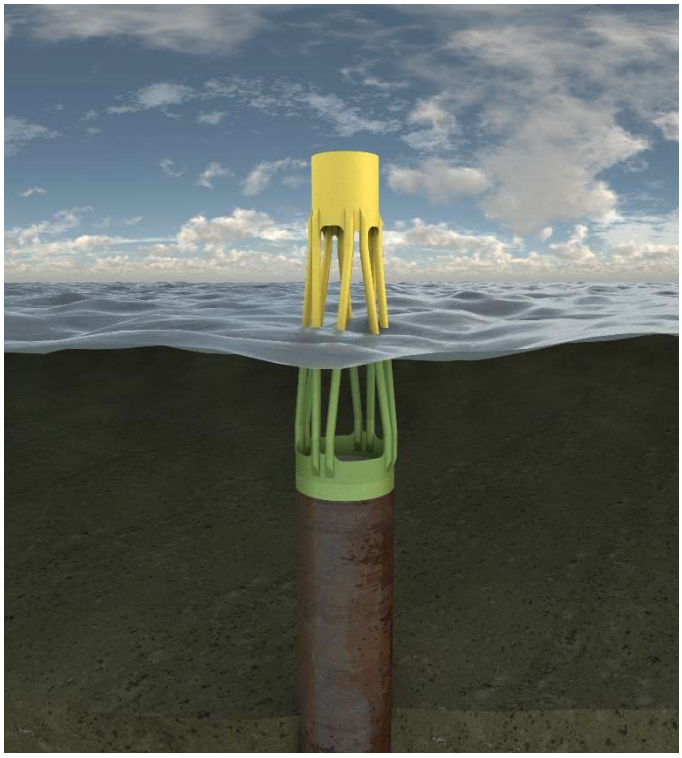

Author: Mary Carol Anderson

Supervisors:

Prof. Dr. A.V. Metrikine	TU Delft – Chairman
Dr. Ir. A. Tsouvalas	TU Delft
Dr. K. van Dalen	TU Delft
Ir. J.S. Winkes	Fistuca BV

FISTUCA

TU Delft Delft University of Technology

Abstract

In the 26 years since the first offshore wind farm was installed in Vindeby, Denmark, the offshore wind industry has undergone remarkable growth. Recently, this growth has accelerated, advancing farms rapidly into deeper water and utilizing larger turbines. As offshore wind farm developers continue to look towards heavier, higher capacity turbines, and harsher sites, improving cost-effectiveness will rely increasingly on support structure optimization. Monopile foundations remain the preferred option, but the "XL" monopiles required in deeper water are sensitive to wave-induced fatigue loads and exceed the weight capacity of many installation vessels.

The goal of the Hybrid Monopile support structure, is to provide a cost-effective alternative to the monopile in water depths greater than 30 meters. By providing an open structure in the key wave loading area of the water column, wave-induced fatigue damage can be reduced, allowing for a thinner monopile shell and a substantially lighter support structure. Design of the Hybrid Monopile began with the optimization of the brace member length and diameter for a specific location and turbine in the North Sea. Computations. were carried out using a Matlab-based model in which the structure is represented as a discretized Euler-Bernoulli beam.

Extreme load cases were applied in a static analysis to ensure that selected dimensions are able to resist buckling of either the monopile shell, or the brace members. An accompanying finite-element model of the structure was used to verify that the selected brace dimensions were sufficient under extreme loads. To estimate the fatigue life of the monopile shell, and the brace members, wave loads were handled in the frequency domain and wind loads in the time domain. Damage equivalent loads (DELs) for each were then combined using quadratic superposition. Wind and wave roses for the selected site were used in the fatigue analysis to capture the effects of misaligned wind-wave cases on the calculated fatigue life. In this design phase, the Hybrid Monopile was shown to experience sixty percent less wave-induced fatigue damage than the traditional monopile.

This baseline version of the design was then modified for 256 different combinations of water depth, turbine size, wave climate, and monopile diameter, to demonstrate the versatility of the concept and identify the design drivers. During the design process, the Hybrid Monopile was updated by altering the monopile shell thickness, brace diameter, and brace length. In each case, a traditional monopile was also designed in parallel, to serve as a basis for comparison. Optimization of each configuration was based on an iterative series of design checks during which the variable design dimensions were increased or decreased based on the structure natural frequency, response to an extreme load, or expected fatigue life at one of the critical locations; the mudline and the individual brace cross sections.

Results of the iteration showed that in more than 3/4 of the test cases, which covered water depths from 30-60 meters, and turbine sizes of 8-20 MW, a Hybrid Monopile could be established that offered lower structure weight and improved fatigue performance at an equal or reduced cost compared to a traditional monopile. Viable configurations showed average weight and cost reductions of 27% and 17% respectively. These results were used to establish a limited number of standardized Hybrid Monopile classes, which could be mass produced and assigned to a wind farm, based on only the water depth and turbine size. Looking forward, further work is required to determine the optimum connection detail at the brace-monopile interface, and to assess the fatigue risk at that junction.

Acknowledgements

The success of this project would not have been possible without the, guidance, insight, and expertise of a long list of individuals who offered support and recommendations throughout the process. I especially want to thank:

Professor Andrei Metrikine and Apostolos Tsouvalas for serving as supervisors from TU Delft. Thank you for helping me to refocus the scope of the work, and for reminding me not to let my "inner salesperson" overshadow my "inner engineer" during the design process.

The entire team at Fistuca BV for their support. Thank you to Jasper Winkes for entrusting me with this project, allowing me to make it my own, and encouraging me to think outside the box. I also appreciate the opportunities you arranged for me to present this work to major industry players, their feedback was truly invaluable. Special thanks should also be paid to Koen Cruesen and Maarten Vogel, for serving as my sounding board during frustrating days, and for their willingness to help me navigate ANSYS. Again, thank you to the entire Fistuca team for creating such a positive work environment. Hopefully a future offshore wind project will give us an opportunity to work together.

Finally, to the unsung heroes of this project. Thank you to my parents, for your unwavering belief in my ability to tackle this challenge and last but certainly not least, to Jack, for figuratively and literally holding my hand through each and every day of these last two years.

Contents

List of Figures

List of Tables

Symbols and Units

1P	rotation frequency of turbine	[Hz]
3P	blade passing frequency of three-bladed turbine	[Hz]
a	wave amplitude	[m]
A	cross sectional area	[m^2]
A_{brace}	cross sectional area of brace member	[m^2]
A_{rotor}	area of the turbine rotor disk	[m^2]
A_{tower}	cross sectional area at tower base	[m^2]
β	damping ratio	[-]
c_{damping}	system damping	[Ns/m]
$c_{\text{crtitical}}$	critical damping	[Ns/m]
$C_{damping}$	system damping matrix	[-]
C_d	drag coefficient	[-]
C_m	inertia coefficient	[-]
$C_M(z)$	inertia coefficient – diffraction adjusted	[-]
C_{red}	reduction coefficient	[-]
C_t	thrust coefficient	[-]
$C(\gamma)$	normalizing factor	[-]
d	water depth	[m]
D	diameter	[m]
D_{brace}	brace diameter	[m]
$D_{mudline}$	shell diameter at mudline	[m]
D_o	outer diameter	[m]
DEL	damage equivalent load	[Nm]
DFF	design fatigue factor	[-]
E	Young's modulus (general)	[GPa]
E_{steel}	Young's modulus steel	[GPa]
$E_{concrete}$	Young's modulus concrete	[GPa]
E_{fibers}	Young's modulus steel fibers	[GPa]
EIG	system eigenmatrix	[-]
E_{py}	stiffness per unit length (soil)	[Ns^2/m^3]
f	limiting shaft friction	[kPa]
f	frequency	[Hz]
f_1	1st natural frequency	[Hz]
f_p	wave peak frequency	[Hz]
f_v	wind frequency	[Hz]
$f_{Morison(x,z;t)}$	Morison force per unit length	[N/m]
$F_{Morison}(t)$	Morison force	[N]
F_{thrus}	thrust force on the rotor	[N]
$F_{Wind}(t)$	total wind force	[N]
h	full height of water column	[m]
$H_{a,n}(\omega)$	hydrodynamic transfer function	[-]
$H_n(\omega)$	mechanical transfer function	[-]
$H_{a,n}(z,\omega)$	combined transfer function	[$(m/rad)^{1/2}$]
H_S	significant wave height	[m]
$H(\omega)$	transfer function (general)	[varies]
$HSSR$	hot spot stress range	[MPa]

I	2nd moment of area	[m^4]
I_{brace}	2nd moment of area (brace)	[m^4]
$I_{centerline}$	2nd moment of area structure section	[m^4]
$I_{concrete}$	2nd moment of area, concrete core	[m^4]
$I_{mudline}$	2nd moment of area at mudline	[m^4]
I_{steel}	2nd moment of area brace steel	[m^4]
I_t	turbulent intensity	[%]
k	wave number	[m^{-1}]
k_S	soil internal friction coefficient	[-]
$\boldsymbol{K}$	stiffness matrix	[-]
$\boldsymbol{K_{modal}}$	modal stiffness matrix	[-]
K_n	modal stiffness (system)	[Ns^2/m^2]
K_{soil}	soil stiffness	[Ns^2/m^2]
l	element length	[m]
L_v	turbulent length scale	[m]
m	slope of the SN curve	[-]
$\boldsymbol{M}$	mass matrix	[-]
$\boldsymbol{M_{modal}}$	modal mass matrix	[-]
$M_{applied}$	applied bending moment	[Nm]
$M_{bending}$	bending moment in a cross section	[Nm]
$M_{resistance}$	design resistance to bending	[Nm]
m_{top}	turbine top mass	[kg]
n	anticipated cycles	[-]
N	total cycles	[-]
N_{axial}	axial load on a cross section	[N]
N_{Euler}	critical Euler buckling limit	[N]
N_k	knee point of SN curve	[-]
N_q	bearing factor	[-]
P_u	ultimate soil strength	[N/m]
q	limiting end bearing	[MPa]
R	rotor radius	[m]
$r(z)$	structural cross-section radius	[m]
$S_{aa}(\omega, z)$	acceleration spectrum, frequency domain	[m^2/rad^3]
$S_{excitation}(f)$	excitation spectrum (general)	[varies]
$S_{JW}(f)$	JONSWAP wave spectrum	[m^2s]
$S_{Kaimal(f)}$	Kaimal turbulent wind spectrum	[$(m/s)^2s$]
$S_{Morison}(\omega, z)$	linearized Morison forcing spectrum	[N^2s]
$S_{response}(f)$	response spectrum (general)	[varies]
$S_{vv}(\omega, z)$	velocity spectrum, frequency domain	[m^2/rad]
$S_{uu}(\omega, z)$	wave response spectrum	[m^2s]
$\boldsymbol{S_y}$	yield strength of steel	[MPa]
SCF	stress concentration factor	[-]
t	thickness	[m]
t_{brace}	brace thickness	[m]
t_{ref}	reference thickness	[m]
T_o	wave peak period	[s]
TE	thickness effect	[-]
$\ddot{u}_1$	node acceleration	[m/s^2]

u_1^{iv}	4th spatial derivative	[-]
$U_c(z)$	current velocity with respect to depth	[m/s]
$u_{total}(x,z;t)$	total water particle velocity	[m/s]
$u_w(x,z;t)$	wave particle velocity	[m/s]
$\dot{u}_w(x,z;t)$	wave particle acceleration	[m/s^2]
V_{10}	wind velocity 10 m above waterline	[m/s]
V_{hub}	wind velocity at hub height	[m/s]
V_w	wind velocity	[m/s]
$\boldsymbol{W}$	elastic section modulus	[m^3]
$\boldsymbol{\gamma_M}$	material safety factor	[-]
$\boldsymbol{\gamma_E}$	environmental safety factor	[-]
z	distance from water surface, negative down	[m]
z_o	surface roughness length	[-]
γ	peak enhancement factor	[-]
δ	interface friction angle	[deg]
ζ_{aero}	aerodynamic damping	[%]
ζ_{damper}	artificial damping	[%]
ζ_{hydro}	hydrodynamic damping	[%]
ζ_{soil}	soil damping	[%]
ζ_{struct}	structural damping	[%]
ζ_{total}	total system damping	[%]
Θ	wave approach angle	[deg]
λ	wavelength	[m]
λ_0	deepwater wavelength	[m]
λ_{tsr}	tip speed ratio of turbine	[-]
φ	phase angle	[rad]
φ_{soil}	internal friction angle	[deg]
φ_z	modal displacement	[m]
φ_z''	2nd spatial derivative of mode shape	[-]
$[\Phi]$	transformation matrix	[-]
$\eta(z,\omega_o)$	decay ratio of water particle acceleration	[-]
ρ	submerged weight of sand	[kN/m^3]
ρ	density (general)	[kg/m^3]
ρ_{air}	density of air	[kg/m^3]
ρ_{water}	density of water	[kg/m^3]
σ	spectral width parameter	[-]
$\sigma_{bending}$	standard deviation of bending moment	[Nm]
σ_{Vw}	standard deviation of wind speed	[m/s]
σ_{yield}	yield stress	[MPa]
ω	wave frequency	[rad]
ω_o	structure frequency, 1st mode	[rad]
ω_n	first natural frequency	[rad]
Ω	rotational frequency of turbine	[rpm]

1. Introduction

1.1. Offshore wind industry trends

In the 26 years since the first offshore wind farm was installed in Vindeby, Denmark, the offshore wind industry has undergone remarkable growth, particularly in the last decade, advancing rapidly into deeper water and utilizing larger turbines. Notably, as of 2007 on two wind farms, Alpha Ventus, and Beatrice, were installed in water depths over 25 meters [5], but in 2015, the average installed water depth was 27 meters, with a total of 34 farms currently installed or planned for site with depths exceeding 25 meters, per the EWEA annual report [64]. This is due to a combination of factors, including the development of larger, higher capacity turbines, a shrinking number of undeveloped shallow water sites, and a high demand for wind energy in deeper water regions. The market for wind energy in deeper water is substantial, particularly in North America where half the of the US population lives in coastal cities [5].

Despite the high demand for renewable energy sources, and the potential for offshore wind to meet that demand, dependence on subsidies to make offshore wind farms costs effective remains a major obstacle. These subsidies are frequently cited as arguments against further offshore development. In response to this, the wind industry has set a goal to reduce the levelized of cost of offshore wind energy, the LCOE, by 40% based on 2012 values, by 2020 [35]. As turbines continue to grow, less units are required to produce the same energy output, and the total number of moving parts decreased. This shifts a portion of the production costs away from operations and maintenance, onto the support structures required by these supersize turbines. The Det Norske Veritas (DNV) manifesto [35] indicates that the capital costs of support structures may present some of the biggest cost savings opportunities, accounting for 25-34% of overall project costs [12]. Looking to the future, optimization of support structures will only become more critical.

1.2. Existing support structure options

Of all offshore wind turbines installed prior to the end of 2012, 74% were on monopile foundations with gravity based foundations (16%), jackets (5%), tripiles (3%) and tripods (2%) making up the remainder [67]. Undeveloped wind farm sites with sufficiently shallow water, where gravity based structures are feasible, are becoming increasingly scarce, and the industry has all but abandoned the tripile and tripod concepts due to poor cost efficiency. As a result, monopiles have continued their dominance, accounting for 93% of 2015 installation [64], with jackets primarily being considered for sites where the water depth or turbine size pushes the technical or economic limits of a monopile support structure.

For prospective sites where water depths are excessive for any bottom-founded structure, floating turbine concepts continue to be developed. Though multiple prototype demonstration projects are in the works sites in very deep water (200 + meters) off Norway and California, floating concepts are estimated to be at least a decade away from being a competitive market option and will not be discussed further in this report [9], leaving jackets and monopiles as the remaining relevant options. Each of these options has its own inherent advantages and disadvantages.

1.3. Jackets

Latticed tower structures, jackets, are adopted from the oil and gas industry, and were once expected to be the go-to support structure for sites where the water depth exceeds 30-40 meters. Jackets structures have the benefit of being dynamically stiff, and therefore less susceptible to long term fatigue. The importance of fatigue in offshore structure design is discussed extensively later in the report.

Figure 1-1: Jacket (left) and monopile (right) support structures [5]

Additionally, the open structure of the jacket significantly reduces the available area for wave loading, and uses up to forty percent less steel than an equivalent monopile. However, despite using significantly less steel than monopiles, the number of required welds and the more intensive engineering effort that must go into each design make them expensive to produce. As offshore wind gains more traction in the US and Asian markets, where soils contain more rock or clay than in seen in the North Sea, and are therefore less friendly to monopile driving, the jacket may see a rise in popularity, but at this the hefty price tag has led the industry to instead focus on pushing the limits of monopile support structures [7].

1.4. Monopiles

Though it used to be a popular opinion that monopiles were not cost effective or feasible beyond 25 m water depths, the industry has continued to push the limits of its favourite foundation and in 2015, turbines were installed on monopile support structures in water up to 37 meters deep at the Gemini wind farm in the Dutch North Sea. Fabrication facilities are responding to the trend and have expanded their capabilities to produce monopiles as large as 10 meters in diameter, and are investing in equipment to produce 12-meter piles. Subsequently, in response to the increasing support structure dimensions, installation contractors are updating their fleets to meet the demand for large capacity vessels [7]. Considering these developments, the conversation regarding the maximum depth for monopile usage continues to evolve.

However, the so-called “XXL” monopiles, on the order of 8-10 meters in diameter, designed for intermediate water depths, have several drawbacks. Notably that they are dynamically “soft” and therefore very sensitive to fatigue damage from wind and wave loading. Issues relating to wave-induced fatigue become more noticeable with increasing water depth, due to the large available loading surface. The hefty structures required to resist fatigue loads push or exceed the capacity of the current installation fleet, and the quantity of steel required to produce them drives up the capital cost. Despite the obvious drawbacks, they remain the industry favourite.

1.5. Concept description & design objectives

This thesis presents the initial stages of design for an alternative support structure concept known as the "Hybrid Monopile". The goal of the design is to incorporate some of the advantageous attributes of a jacket support structure, into a monopile design to produce a new and attractive foundation option for large offshore wind turbines in intermediate water depths of 30-60 meters. A Hybrid Monopile consists of an open braced section situated between a standard monopile base and transition piece to reduce the wave loading on the structure, and the overall structure weight. Intermediate bracing in this open section is omitted to limit the amount of required welding during production.

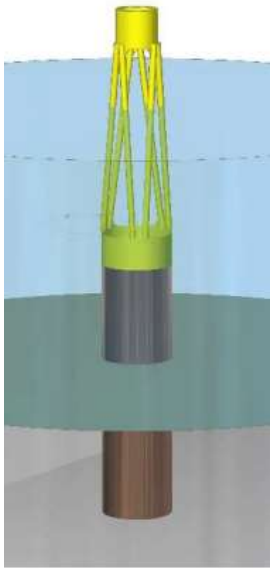

Figure 1-2: Hybrid Monopile concept render

To be a considered a practical market option, the structure must not only show equivalent or superior dynamic performance compared to its standard monopile counterpart, but provide a cost benefit. Achieving this requires a versatile structure that is suitable for use in a variety of water depths and loading conditions, with minimal modifications, thus making it possible to mass produce economically.

The design concept is made possible by major evolutions in offshore installation technology. Traditional pile driving methods would severely damage the brace members, but Fistuca BLUE Piling Technology, which produces longer, lower intensity blows, could feasibly drive the complete structure into place. Alternatively, it is proposed that the open Hybrid section be installed as a separate unit after the base monopile is driven into place, using an underwater connection between the monopile and brace section, currently under development by Fistuca BV.

1.6. Summary of previous concept feasibility reports

Initial concept feasibility studies were performed by Enersea and Huisman based on the original design geometry. The first iteration of the structure geometry designated a 30-meter Hybrid section extending 10 meters above mean sea level and 20 meters below, with a 6.5-meter monopile diameter at the top and a 10-m diameter at the base

The Enersea report focused on the global structure behaviour, possible alternative configurations, and some high-level loading calculations, while the Huisman report focused on design details and structure behaviour at the welded connection between the brace members and monopile sections.

1.7. Enersea

Two different member configurations were considered, one with 3 pairs of members (3x2) and one with 6 pairs, referred to as a 6x2. A traditional monopile support structure was also assessed as a basis of comparison. In both cases member diameters and thicknesses of 1000 mm/750mm and 50mm/38mm were investigated. A non-specific 8 MW reference turbine was used as the basis of design and a simplified extreme load check. Wind-induced fatigue damage was not assessed, but a deterministic analysis of the wave-induced fatigue damage under typical North Sea conditions was performed.

Additionally, pile penetration, and installation stress calculations (based on BLUE Piling) were addressed. Results of the study provided insights into the strengths and weaknesses of the concept, and were used to guide the initial iterations of the Hybrid support structure design.

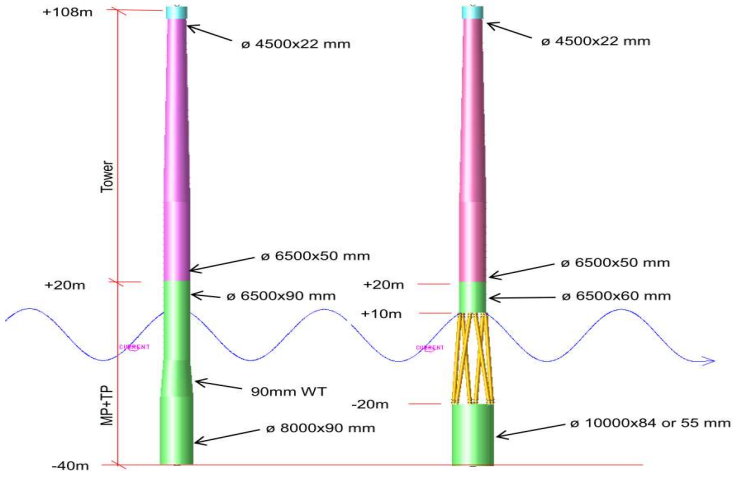

Figure 1-3: Enersea feasibility study basis of comparison

Under extreme load conditions with fully aligned wind and waves, the 6-pair configuration failed regardless of member diameter or thickness. This was attributed to the extremely low batter angle of the members which failed to adequately distribute axial loads, and made the members vulnerable to torsional failure as well. Increasing the dimensions for members in this configuration sufficiently to avoid failure under extreme conditions resulted an increase in wave loading compared to the reference case, defeating the purpose of the Hybrid design.

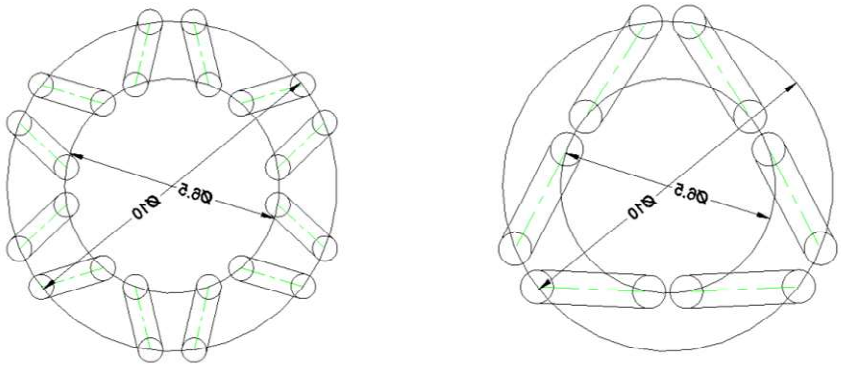

Figure 1-4: Top view 3x2 and 6x2 brace arrangements with associated dimensions

With respect to fatigue, the Enersea study highlighted the potential of the Hybrid structure to substantially reduce wave-induced fatigue damage in the monopile shell at the mudline. For small waves, reductions in loading of up to 75% were considered possible. A simplified, deterministic fatigue analysis, indicated that the 3x2 Hybrid section, with a 55-mm monopile shell, could have a wave-induced fatigue life at the

mudline of 1097 years, compared to 53 years for the base case monopile with a 90-mm shell, under the same unidirectional wave conditions, effectively making wave-induced fatigue negligible at the seabed.

The potential for cost savings on raw material is substantial, both from reducing the amount of steel in the in the wave loading area, and from potentially reducing the monopile shell thickness and required penetration depth. Depending on the selected monopile shell thickness, total structure weight was predicted to see reduction by 16-37%, though some of that savings would be lost to increased production costs.

Areas not addressed in the report, but important for progressing the design include, wind-induced fatigue, fatigue damage in the individual brace members and their connections, vibrations during driving, resistance to accidental impact loads, the effects of diffraction on the wave loads, cases with misaligned wind-wave loads, and the modal behaviour of the structure.

1.8. Huisman

The Huisman report served as the first mechanical validation of the Hybrid Monopile concept, utilizing the environmental loads and damage equivalent fatigue loads produced by Enersea. Applying the previously calculated loads to a finite element model of the initial Hybrid Monopile design, it was confirmed that the brace and shell dimensions determined by Enersea were sufficient, and that the axial installation loads exerted by the BLUE Piling hammer would not exceed the Euler buckling limit of the brace members. The study also produced a welded connection detail that survives under both extreme and fatigue loading. It was indicated in the report conclusions that the governing load case for that connection detail would be the stresses produced by the BLUE Piling hammer during installation.

Further investigation into the optimization of the connection between the brace members and monopile sections is still ongoing, so for the purposes of this report it was assumed that all iteration of the Hybrid Monopile use this same connection detail, and that the detail survives all load cases.

1.9. Design approach

The feasibility reports shed light on some of the key opportunities and challenges associated with the Hybrid concept, but are based on only one unoptimized geometric configuration. Varying the top and bottom monopile diameters, brace dimensions, and their arrangement, produces thousands of possible design iterations that may be the optimal combination. It would not be logical or feasible to perform a thorough assessment of every combination of brace number, arrangement, diameter, thickness, length, and material, so the design process was split into three phases.

In the first phase, a mathematical model of the structure is established, and simplified analyses, like those used in the Enersea report, are used to rapidly obtain data regarding the relative benefits of different design iterations under extreme loads at the sample North Sea site. This pre-screening data is used to complete a preliminary dimensioning of the updated Hybrid Monopile design, and elements of the mathematical modelled are verified before moving forward with the design.

In the second phase, the fatigue life of the structure is calculated under combined wind and wave loading, to ensure the adequacy of the proposed dimensions and quantify the benefits of the design with respect to wave induced fatigue. Extreme loads are then reapplied based on any dimension updates triggered by the fatigue life check. At this stage, serviceability limit state assessment, accidental loading, and installation load cases are also incorporated, and the option of filling the Hybrid members with concrete is discussed. This phase culminates in a Hybrid Monopile configuration that is optimized for a specific location and turbine.

The last phase is to determine a configuration that is not necessarily optimal for, but will perform successfully, in multiple locations under various loading conditions. This is done using a sensitivity analysis to determine the most critical design dimensions, and how they must be modified for new environments and turbines. The result is a set of simple guidelines for iterating the structure based on a limited set of site parameters.

1.10. Report Outline

This thesis follows the above process after first providing some general background. Chapter 2 introduces the reference turbine that the initial Hybrid Monopile structure is designed to support, as well as detailing the environmental conditions of interest at the design site. Basic calculation methods for aerodynamic and hydrodynamic loading are introduced, and the reference monopile that serves as a basis for comparison, is provided.

Chapter 3 discusses general design methodology and industry design standards, and outlines the key design checks that are to be undertaken. Also discussed in this section are the inherent assumptions in the modelling methods, and some additional assumptions specific to this design process. Subsequently, Chapter 4 details the early design checks that were used to select the new member dimensions and arrangement for the baseline version of the Hybrid Monopile. The environmental loads and modal behaviour determined in this section are then verified using an offshore wind turbine simulation software known as FAST, the process of which is explained in Chapter 5.

In the sixth and seventh chapters, this updated Hybrid design is put through more detailed fatigue and extreme load assessments. Fatigue behaviour proves to be a governing element of the design, and is far less straightforward to calculate than extreme loads, so Chapter 6 gives an overview of different procedures for performing the fatigue calculations, including the relative merits of each. The determination of extreme load cases and the results of the ULS analyses are then seen in Chapter 7.

During the design process, the option of filling the Hybrid brace members with fibre-reinforced concrete was discussed. Chapter 8 describes the implications of this design option, repeating the analyses performed in the previous two chapters for an alternative Hybrid Monopile using concrete-filled members, and outlines the pros and cons of the configuration.

To validate the results of the modal analysis and ULS assessments, and assess additional load cases of interest, a finite element model of the updated Hybrid Monopile was created in ANSYS and is presented in Chapter 9. In addition to verifying that the structure would survive under ULS loading, the ANSYS

model was also used to investigate the response to loads exerted by the Fistuca BLUE Piling hammer during installation, and to accidental loading from boat impact, the results of which are given in Chapter 10. This chapter further discusses the installation considerations for the Hybrid Monopile with respect to the ANSYS results and the structure weight.

Chapter 11 delves into the third phase of the design process, during which the Hybrid Monopile design was iterated for over 200 combinations of water depth, turbine size, base diameter, and wind/wave spectra. Results of these iterations were then used to reduce all possible combinations to a set of two possible Hybrid Monopile "Classes" for each size of turbine, which can be mass produced and easily selected for a wind farm project based only on the water depth and turbine size.

Lastly, Chapter 12 summarizes the conclusions of this work and provides recommendations for continued research and development of the structure concept.

1.11. List of software used

The following software packages were used for the analyses presented in this thesis:

MATLAB R2015a, general purpose mathematical modelling

FAST v8.16, open-source multi-physics wind turbine engineering software tool developed by the National Renewable Energy Laboratory

ANSYS v17.1 (APDL Mechanical)**,** general purpose finite element program,

2. Design Basis

2.1. Wind turbine basics

Offshore wind turbines are complex multi-component systems in which the components form sub-systems that interact with each other and the external loading environment. Figure 2-1 outlines the key subsystems and the relationships between them. For more theoretical background related to offshore wind turbines and their operations refer to reference items [45-46].

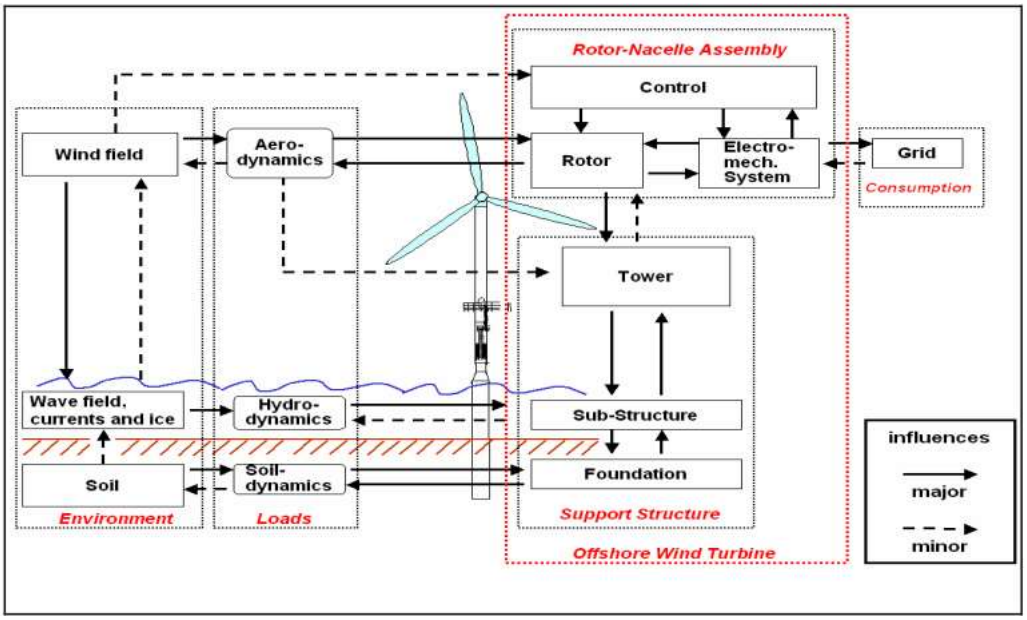

Figure 2-1: Offshore wind turbine system components and interactions [1]

The Hybrid monopile contains both the foundation and sub-structure sections, which are joined to the tower using a transition piece. Throughout this report, the rotor nacelle assembly may be referred to as the RNA. In the offshore wind industry, the RNA and the tower are designed and engineered independently from the support structure. However, since the aerodynamic loads on these upper sections drive the design of the lower structure, the intended turbine should be selected prior to the detailed structure design.

2.2. Reference turbine

Since the Hybrid Monopile support structure concept is geared towards larger offshore wind turbines, the baseline structure design is based on a generic 8 MW turbine, based on limited data available from the Vestas V164-8.0 MW model, currently the largest commercially available turbine. Turbine or tower parameters not available from Vestas, are approximated using Enersea in-house data and public papers. Relevant parameters for the support structure design are listed in Table 1. For the support structure design, the 1P and 3P operating frequency ranges are of particular interest, as they will result in a limited band of frequencies band, within which the first natural frequency of the structure must fall. This is described in more detail in Chapter 3.

Table 1: Relevant reference turbine parameters

Turbine parameter	*Value*	*Unit*
Rated power	8.0	MW
Rotor diameter	164	m
Mass of rotor and nacelle	460	tonnes
Tower mass	375	tonnes
Cut-in wind speed	4.0	m/s
Cut-out wind speed	25.0	m/s
Lower bound rotor speed	5.4	rpm
Upper bound rotor speed	11.5	rpm
Nominal rotor speed	10.6	rpm
1P frequency range	.09-.192	Hz
3P frequency range	.27-.575	Hz
Nominal operating frequency	.177 (1P), .530 (3P)	Hz
Tower diameter - top	4.5	m
Tower diameter – base	6.5	m
Tower thickness - top	22	mm
Tower thickness – base	50	mm
Hub Height (above sea level)	108	m

It is assumed for the purposes of this report that the tower has a taper angle of 2.0 degrees, and that the thickness varies linearly along the entire length of the tower. This set of parameters is sufficient to model the geometry of the reference turbine, and to produce reasonably accurate time series of aerodynamic forces on the operational rotor. The load calculation procedure is discussed further in Chapter 3.

2.3. Reference location and design elevations

In determining the wave loading parameters for the hypothetical wind farm location, a water depth of 40 meters was selected to represent some deeper portions of the North Sea. As previously stated, a key design objective for the project is to produce a design that is suitable for a variety of project sites, so rather than use site-specific data at this stage, a generic set of environmental parameters, were selected to represent “typical” North Sea conditions in the 40-meter region, shown in Figure 2-2. Site-specific environmental data from meteorological buoys at potential project location, both in North Sea and the Atlantic Ocean on the east coast of the United States, are used during a sensitivity analysis later in the report.

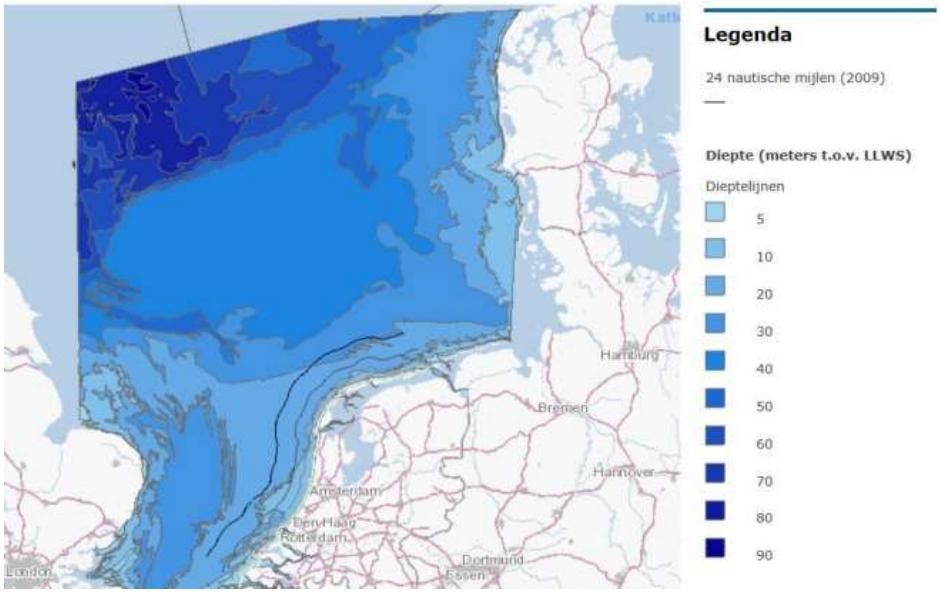

Figure 2-2: North Sea bathymetry [Noordzee-loket]

Besides depth, other water level elevations that are relevant to the design are shown in Figure 2-3: Design elevations of interest [28]and listed below. Values refer to the distance above the seabed.

- Interface Level 54.00 m
- Mean Sea Level (MSL) 40.00 m
- Max 50-yr level 42.50 m
- HAT 41.25 m
- LAT 38.75 m

Generalized North Sea wave, tide and storm surge data in the study was taken from the OSPAR Quality Status Report of 2000 for Region II Greater North Sea to establish a set of lumped "sea states" to describe the full set of wind and wave behaviours at the site.

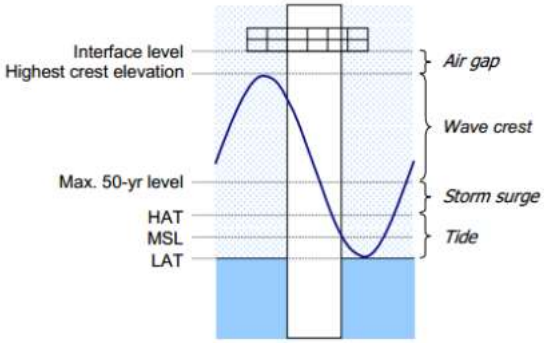

Figure 2-3: Design elevations of interest [28]

Sea states are determined by discretizing hindcast data from the North Sea, validated with measurements from the numerous research and industry platforms present there, into two and three-dimensional histograms. These histograms are created with evenly spaced bins, and the data in each bin defines a characteristic "sea-state". For the purposes of this analysis, a sea state is defined by a wind speed, significant wave height, peak wave period, and wave direction, each with a similar probability of occurrence. Wave heights are distributed into 1.0-meter bins and wind speeds into 2.0-m/s bins.

2.4. Wave spectra

Wave conditions defined in the lumped sea states are represented using wave spectra. Measurements performed during the Joint North Sea Wave Project resulted in what is known as the JONSWAP spectrum, a popular method for modelling and predicting wave conditions in the offshore industry. The JONSWAP spectrum is used in the offshore industry to model sea states that are not fully developed, or have a "limited fetch", i.e. have not reached their full potential at the present wind speed [11]. For locations relatively close to shore, this is often the case. Fully developed sea states are modelled by the Pierson-Moskovitz spectrum, which differs from the JONSWAP spectrum by a peakedness factor γ, derived from the peak wave period. A γ value of 1 would result in the Pierson-Moskovitz and JONSWAP spectra being identical. The area under the spectrum indicates the energy density in the sea for a given wave height.

Using the scatter parameters of H_S, the significant wave height (approximately 4 ties the standard deviation of the wave height) and T_P, the peak wave period corresponding to that wave height, the spectrum can be computed using the following equations [25].

$$S_{JW}(f) = C(\gamma) * 0.3125 * \mathrm{H_S^2} * f_p^5 * f^{-5} * \exp\left[-\frac{5}{4} * \left(\frac{f_p}{f}\right)^4\right] * \gamma^{\exp(\alpha)}$$

$$\sigma = \begin{cases} .07 \; for \; f \leq f_p \\ .09 \; for \; f > f_p \end{cases}$$

$$C(\gamma) = 1 - 0.287 * \ln(\gamma)$$

$$\alpha = \frac{(f - f_p)^2}{2 * \sigma^2 * f_p^2}$$

with

S_{JW}	JONSWAP wave spectrum	[m²s]
γ	peak enhancement factor	[-]
H_S	significant wave height	[m]
f_p	wave peak frequency	[Hz]
f	frequency	[Hz]
$C(\gamma)$	normalizing factor	[-]
σ	spectral width parameter	[-]

The conversion from sea state date to wave spectra is shown as follows. Table 2 shows the Enersea provided sea state parameters.

Table 2: Typical North Sea sea-states [17]

Hs (m)	T0 (s)	n cycles (25 yrs.)	Probability (n)
0.5	3.2	10305098	9.608E-02
1	4.3	59092332	5.510E-01
2	5.9	30269367	2.822E-01
3	6.9	5779211	5.388E-02
4	7.8	1326349	1.237E-02
5	8.6	345151	3.218E-03
6	9.2	96626	9.009E-04
7	9.8	28093	2.619E-04
8	10.3	8322	7.759E-05
9	10.8	2498	2.329E-05
10	11.2	762	7.105E-06
11	11.6	238	2.219E-06
12	12	76	7.086E-07
13	12.3	25	2.331E-07
14	12.6	8	7.459E-08
15	12.9	3	2.797E-08
16	13.2	1	9.324E-09
17 (ULS)	13.8	.5	4.662E-09

The values for significant wave height and peak period are used to produce the JONSWAP wave spectra shown in Figure 2-4.

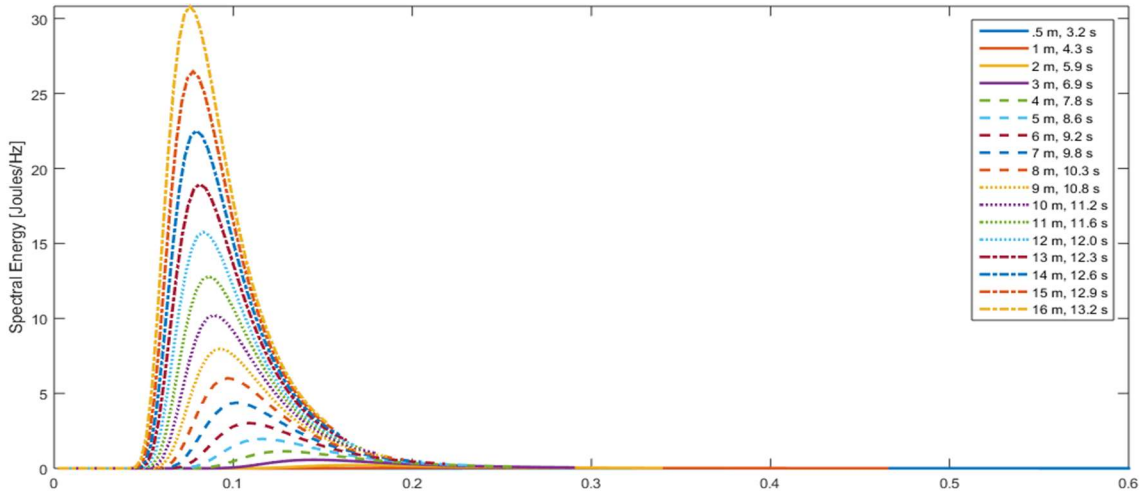

Figure 2-4: JONSWAP wave spectrum for typical North Sea conditions

The produced spectrum can then be used to calculate wave loads on a structure, either directly in the frequency domain, or by producing time series of wave loads with the help of an inverse Fourier transforms to move between the frequency and time domains. A 600 second time history for a 4-meter wave, produced from the wave spectra in Figure 2-6 is shown below.

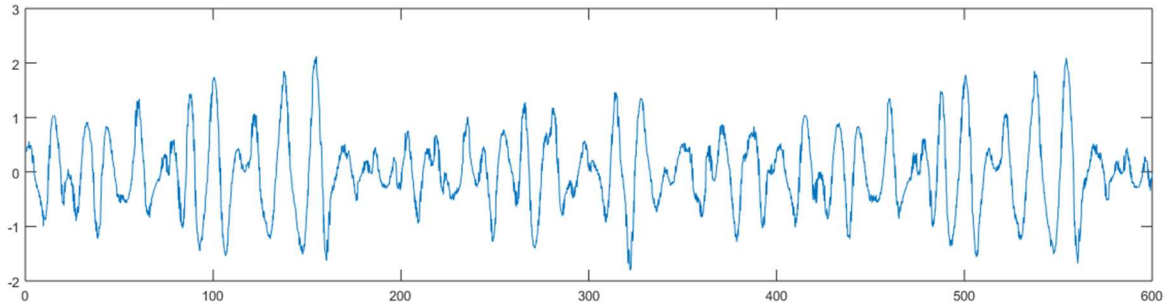

Figure 2-5: Irregular wave time history produced from JONSWAP wave spectrum

These irregular waves are produced by superimposing the individual sinusoidal components, each with an amplitude and frequency derived from the spectra. At any point in the time history the water surface elevation is summation of each of the harmonic components. Further discussion of the kinematic behavior of, and load exerted by, these waves follows in Section 2.7.

2.5. Current

Tidal current is taken to be 1.4 m/s at the still water line and decays with depth. The decay follows the power law function below, where z is the elevation from the water surface, negative downward, and h is the height of the water column.

$$U_c(z) = 1.0 * \left(\frac{h+z}{h}\right)^{\frac{1}{7}}$$

Loads exerted by the current on the structure are included in the ULS analysis, but as they fluctuate at a rate that is well below that of wind or wave excitation, they are omitted during any fatigue assessments [11].

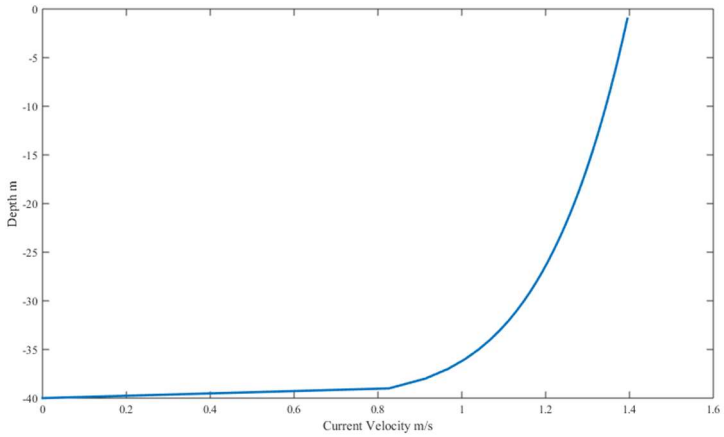

Figure 2-6: Current velocity profile with respect to depth

2.6. Extreme/breaking waves

For the 40-meter water depth considered in the baseline analysis, even the 17-meter significant wave height considered as the 50-year wave, still falls below the breaking criteria of .78*depth, so breaking waves are not anticipated and will not be discussed further.

2.7. Hydrodynamic loads on structures

The most common method for determining individual water particle motions within a wave is to use Linear/Airy wave theory, but depending on the depth of the water of size of waves, there are instances where it may not be the most appropriate. Using Figure 2-7 it was determined that some of the larger waves in the baseline data would be more aptly described using the Stokes' 5th order equations. Stokes waves are characterized by steeper peaks and shallower troughs compared to linear waves. However, calculations during the preliminary assessment, run using both theories, showed less than 4 percent different in the resulting loads on the structure, so the remaining calculations were performed using the simpler theory. For a more in-depth discussion of the relevant wave theories, refer to [45].

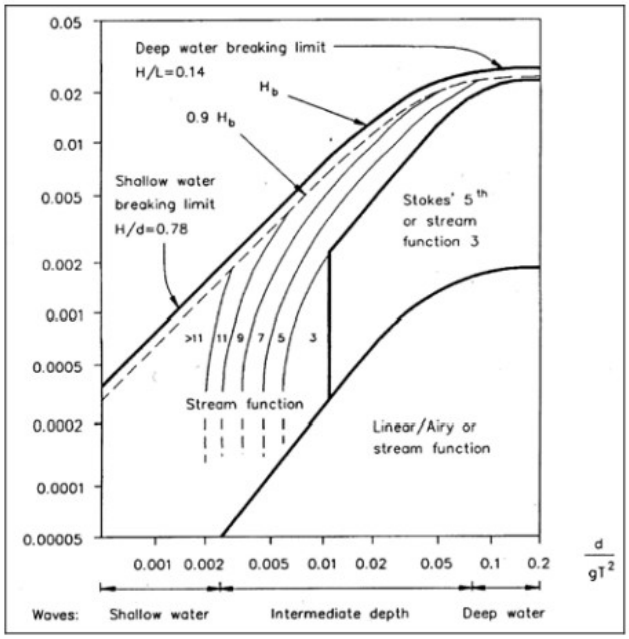

Figure 2-7: Determination of applicable wave kinematic functions [17]

2.8. Wave kinematics and the Morison equation

The wave-induced forces on the support structure are dependent on the wave particle kinematics. Airy wave theory [26] describes every wave as a super-positioned series of harmonic sinusoids, each characterized by a wave number *k*, wavelength λ, and phases angle φ, in which the individual water particles move in circles as the wave propagates.

When water is not sufficiently deep with respect to the wavelength of the wave, bottom friction at the seabed will causes the particle orbits to flatten into ellipses instead of circles. In both cases, particle motion has the highest magnitude at the sea surface and decays with depth. Notable for the Hybrid design concept, is that this decay occurs more quickly in deeper water, such that deeper water will likely not required a longer Hybrid section to achieve the same wave load reduction. This decay with depth is visualized in Figure 2-8.

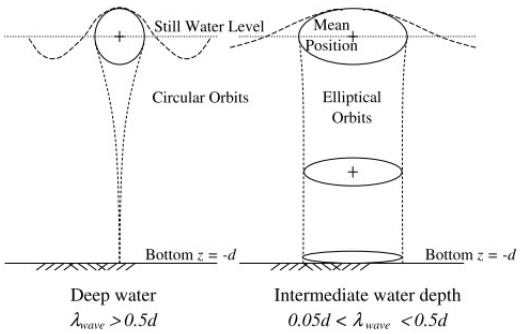

Figure 2-8: Water particle motion with respect to depth [46]

Velocity and acceleration of the particles are described by:

$$u_w(x,z;t) = a\omega * \frac{\cosh\big(k(z+d)\big)}{\sinh(kd)} * \cos(kx - \omega t + \varphi)$$

$$\dot{u_w}(x,z;t) = a\omega^2 * \frac{\cosh\big(k(z+d)\big)}{\sinh(kd)} * sin(kx - \omega t + \varphi)$$

Where:

$\boldsymbol{a}$	Wave amplitude *(.5*Height)*	[m]
$\boldsymbol{\omega}$	Wave frequency (1/T)	[rad]
$\boldsymbol{k}$	Wave number	[1/m]
$\boldsymbol{z}$	Position in water column, negative downwards	[m]
$\boldsymbol{d}$	Total water column height	[m]
$\boldsymbol{\varphi}$	Random phase angle	[rad]

These linear wave theory equations are only valid up to the still water level, so for this study, the method of Wheeler stretching [45] is applied to described the kinematics of the wave particles above the still water level. The stretching process redistributes the calculated velocity and acceleration so that the maximum values occur at the highest point on the water surface at each time step, instead of the still water line.

To calculate the hydrodynamic forces resulting from the waves, Morison's equation for forces exerted by wave on vertical cylinders [25], shown below, is applied. The full form of the Morison equation also incorporates the relative motions of the structure on which the loads are applied, but in this case those values are assumed to be small with respect to the water particle velocity and acceleration, and are therefore excluded unless specifically stated.

$$f_{Morison(x,z;t)} = C_d * \frac{1}{2}\rho_{water} D * |u_{total}(x,z;t)| * u_{total}(x,z;t) + C_m * \frac{\rho_{water}\pi D^2}{4} * \dot{u}_w(x,z;t)$$

In the first term of the equation, $u_{total}(x, z; t)$ refers to the sum of the water particle velocity from both waves and current. The acceleration term is only comprised of a wave acceleration component, as the current velocity is considered relatively constant. D is the effective diameter on which the load is being applied including any marine growth, and C_d/C_m are the drag and inertia coefficients. For large diameter cylinders, such as those used in the wind turbine support structures, the inertia loads will tend to dominate, accounting for more than 90% of the resulting force. These inertia loads are quadratically proportional to the structure diameter, which contributes to the increased importance of wave loads in the assessment of large offshore support structures.

The drag coefficient C_d may vary between .6 and 1.05 over the structure lifetime, based on the roughness of the cylinder, influenced by marine growth. Generally, the inertia coefficient C_m is taken as 2.0, but may be adjusted to account for diffraction effects that are relevant for small waves on large structures, discussed further in 2.10.

For the purposes of this analysis, the inclined members in the Hybrid structure and the inclined face of a tapered monopile section, are treated as vertical. This means that no phase shift between loads applied at the top and bottom of the sections is accounted for, and no vertical loads are applied to the inclined member faces.

2.9. Linearized Morison for frequency domain calculations Wave kinematics

Later analyses to assess the response of the structure to fatigue waves are to be performed entirely in the frequency domain, where the non-linear drag term of the Morison equation presents an issue. In Seidel [8] the drag term is eliminated from the computations entirely, given the inertia dominance. For this study however, it is important to maintain the term, as the smaller diameter brace members of the Hybrid section that are less inertia dominated than a large diameter monopile, so drag forces may still be relevant.

To handle this non-linear drag in the frequency domain, the linearization procedure outlined in Borgman [31] is applied, in which the velocity and acceleration are treated as response spectra to the JONSWAP spectrum of the loading wave. In this method, the non-linear term is instead approximated by the first term of the Fourier series expansion.

$$S_{vv}(\omega, z) = \omega^2 * [\cosh^2(k * z)/\sinh^2\ (k * d)] * S_{JW}(\omega)$$

$$S_{aa}(\omega, z) = \omega^4 * [\cosh^2(k * z)/\sinh^2\ (k * d)] * S_{JW}(\omega)$$

These velocity and acceleration spectra can be used to reformulate the Morison equation as:

$$S_{Morison}(\omega, z) = \left(C_d * \frac{1}{2}\rho_{water} D\right) * S_{vv}(\omega, z) + \left(C_m * \frac{\rho_{water}\pi D^2}{4}\right)^2 * S_{aa}(\omega, z)$$

This linearized form of the equations allows for the full computation of the hydrodynamic transfer function in the frequency domain without omitting the drag forces.

2.10. Diffraction Considerations

Since it is already known that the inertia term will dominate the loading calculations, it is critical to correctly select the corresponding inertia coefficient. Morisons equation [26] is intended for calculating forces on "slender" piles where the pile diameter is less than 1/5 the wavelength of the forcing wave. When this criterion is not met, diffraction theory for the wave forces as established by MacCamy & Fuchs [27] is more appropriate.

As an alternative to switching entirely to the MacCamy & Fuchs method for load calculations, it is common to incorporate it as a correction to the inertia coefficient C_m. The correction curve for this coefficient is shown in Figure 2-9, where λ_o represents the wavelength of the wave in deep water and $D(z)$is the structure diameter at elevation z.

$$C_M(z) = -2.5 * \left(\frac{D(z)}{\lambda_0}\right)^3 + 7.53 * \left(\frac{D(z)}{\lambda_0}\right)^2 - 7.9 * \left(\frac{D(z)}{\lambda_0}\right) + 3.2 \leq 2.0$$

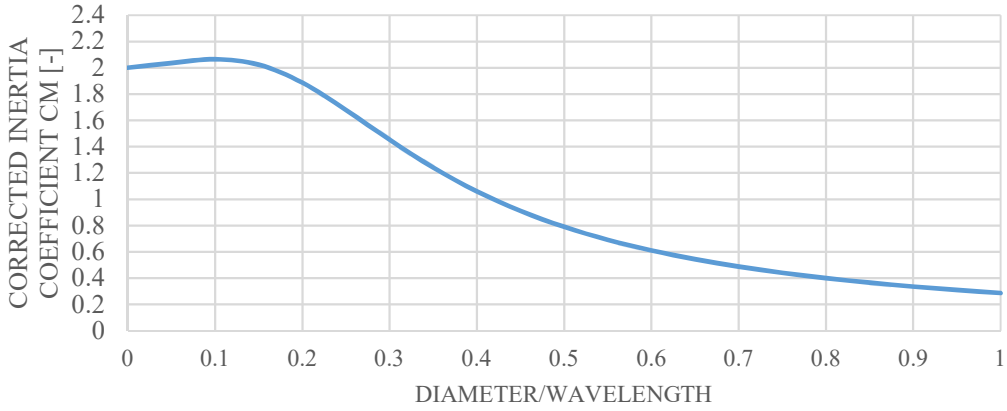

Figure 2-9: Computing the MacCamy-Fuchs diffraction correction coefficient

Initially, for wave cases where the diffraction criterion was not met, i.e. $\lambda_o < 5*D(z)$, the load was recalculated using the full McCamy-Fuchs formula, in lieu of the inertia coefficient correction. The difference in the calculated loads was less than 4%, so the remainder of the calculations were carried out using the inertia coefficient correction method. The total wave load at a point of interest on the structure can then be calculated by integrating the results of the Morison calculation with respect to the elevation *z*.

2.11. Wind profiles

Measurements of mean wind speed are typically denoted by a subscript that indicates the height above the earth's surface at which the measurement was taken, most commonly at 10 meters or V_{10}. Close to the surface, wind speed profiles are slowed and distorted by frictional forces that introduce turbulence to the flow. To determine the actual wind speed at hub height for a large offshore wind turbine, logarithmic

scaling of the V_{10} measurement is performed. The logarithmic profile of wind speed is shown in the equation below:

$$V_{hub} = V_{10} * \frac{\ln\left(\frac{10}{z_o}\right)}{\ln\left(\frac{hub\ heigh}{z_o}\right)}$$

with z_o representing the surface roughness length, taken as .002 for an offshore environment according to Germanischer Lloyd (GL) wind turbine certification guidelines [47].

For the generic North Sea location, wind speeds were extrapolated from the mean wind speed for the region. Using the mean wind speed, scaled to the applicable hub height, the probability of various wind speed at the site can be approximated from a Weibull distribution about the mean wind speed at the rotor using shape and scale parameters as defined by the designated IEC wind type. The scale parameter relates to the mean annual wind speed, and the scale parameter to its variance. For this study, IEC Class B winds are assumed, lending to shape and scale parameters of 1/7 and 2.2 respectively [23]. Figure 2-10 shows the wind speed probability distribution for a mean wind speed of 11 meters per second.

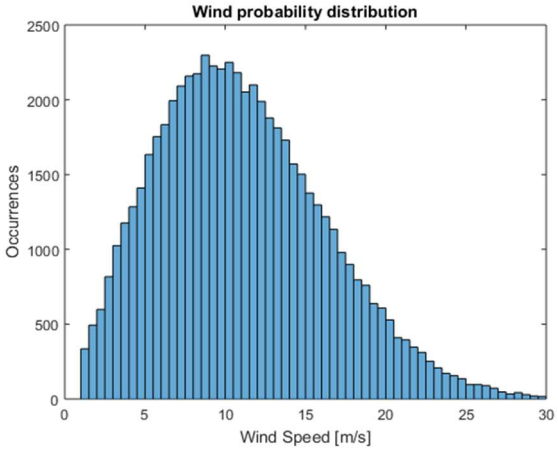

Figure 2-10: Weibull distribution of wind speeds for average speed of 8 m/s

From the histogram, based on a sample size of 60000, it is apparent that extreme wind conditions above cut-out conditions are rare, and that the most probable wind speed falls below the mean wind speed in the spectra [33]. Given these conditions, wind-induced fatigue damage is not caused by the wind loads themselves, but by the rapid fluctuations in wind loads caused resulting from turbulent wind conditions.

2.12. Wind spectra & turbulence

Even at hub heights of over 100 meters, wind speeds still contain turbulence and do not flow steadily at a mean speed, but fluctuate about the mean. Based on the surface roughness and altitude at a prospective wind farm location, design standards assign a presumed turbulent intensity as a function of the local wind speed and its standard deviation according to:

$$I_t = \frac{\sigma_{Vw}}{V_w}$$

A turbulent intensity of 15%, corresponding to the IEC Class B winds assumed for this report, is used to generate the turbulent wind spectrum [23]. This turbulent wind can be approximated from the Kaimal spectrum, the accepted method in Denmark for loads on offshore wind turbines, based on the standard deviation of the wind speed σ the mean wind speed V_w and a model dependent turbulent length scale L_v, also assigned in the design standards [34].

$$S_{Kaimal(f)} = \frac{\sigma_{Vw}^2 * 4 * \frac{L_v}{V_w}}{\left(1 + 6 * f_v * \frac{L_v}{V_w}\right)^{\frac{5}{3}}}$$

Figure 2-11 compares this theoretical Kaimal spectrum, indicated by the smooth black line, to the spectrum produced by Fourier transforming a time history of wind speed measurement data. The noisy spectrum from the directly transformed wind data is difficult to work with for loading calculations, as small changes in the time or frequency step can dramatically change the resulting signal, as shown by the red line, which shows an attempt at filtering the noise by averaging adjacent frequency bins. The signal becomes less noisy, but also has low resolution. The implications of this are discussed further during the fatigue assessment method comparison in Chapter 6.

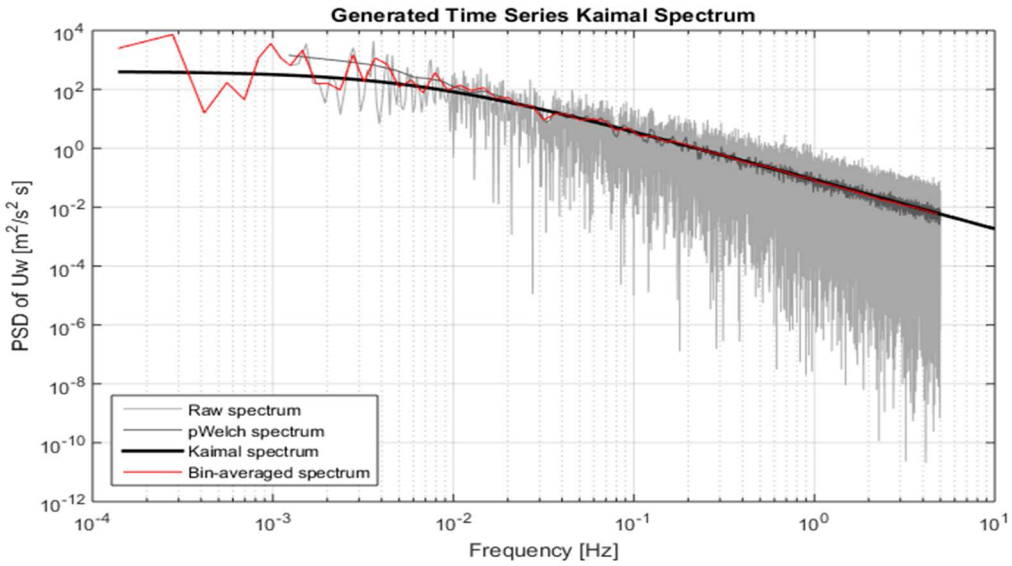

Figure 2-11:Kaimal turbulent wind spectrum for time series generation

For each sea state, a realistic time series of turbulent wind speeds is generated from the theoretical spectrum using inverse Fourier transformation. Figure 2-12 shows the times series corresponding to the mean wind speed of 11 m/s. A detailed description of the process may be found in [34].

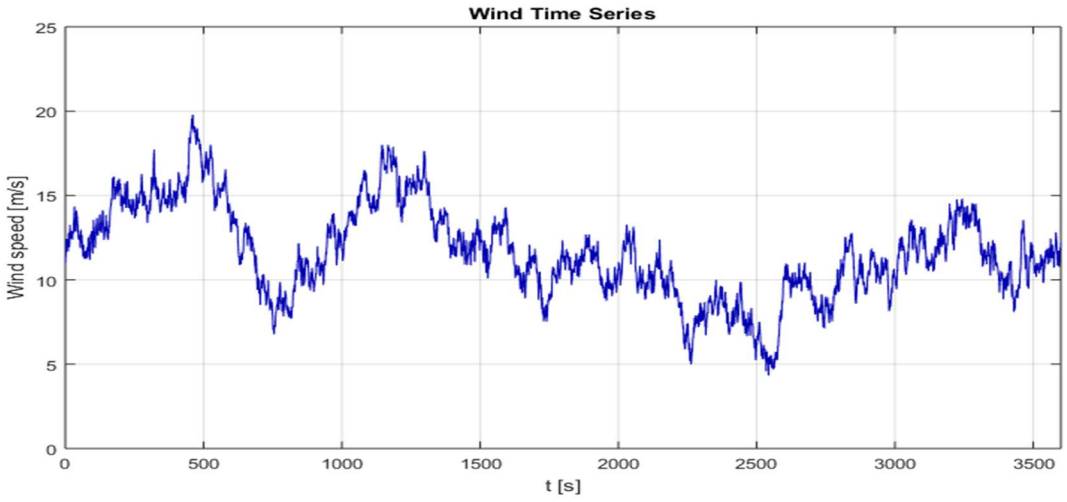

Figure 2-12: Realistic wind time series generated from the Kaimal spectrum for mean wind speed 12 m/s

2.13. Wind loads on structures

Computing the forces exerted on an offshore wind turbine by the turbulent wind field is done using the Blade Element Momentum Theory, or BEM. Details of the theory can be found in [46], but the basis of the theory is to consider the incoming air to be an incompressible force, and to calculate the change in momentum of the flow. By conservation of momentum, the change in the momentum of the wind field must be converted into lift and drag forces on the rotor blades.

For the purposes of the support structure design, the individual components are of less interest than the total force on the operational rotor. This thrust force can be calculated using;

$$F_{thrus} = \frac{1}{2} * A_{rotor} * \rho_{air} * V_w^2 * C_t$$

With

ρ_{air}	1.225	[kg/m^3]
V_w	Incident wind speed	[m/s]
A_{rotor}	Area of the rotor as a disk	[m^2]
C_t	Thrust coefficient	[-]

The dimensionless thrust coefficient C_t accounts for the difference between the velocity of the incoming wind and the velocity of the rotor blades at an instantaneous moment in time. C_t is a function of the tip speed ratio λ; the tangential velocity of a blade tip divided by the incoming wind velocity.

$$\lambda_{tsr} = \frac{\Omega R}{V_w}$$

At wind speeds near the rated wind speed for a turbine, where the tip speed ratio is optimal, the thrust coefficient C_t is at its maximum value of .88.

Though the incident wind field also exerts loads on the tower, the area of the tower is less than 5% that of the operational rotor area, so at operational wind speeds, no aerodynamic loads on the tower are accounted for. During non-operational conditions where wind speeds fall either below the cut-in or above the cut-out wind speed, wind forces on the tower have been included using the same thrust equation, but replacing A_{rotor} with the sum of the tower area and individual stationary blade areas.

Additionally, since the maximum shear forces and bending moments in the structure resulting from wind loading will occur when the wind strikes the rotor in the primary direction, all load cases for this report take the wind to be fully aligned with the rotor to further reduce the number of required simulations. Incorporating wind misalignment and the possible effects is considered an area for potential future research.

2.14. Soil

The horizontal loads exerted on the offshore by wind and waves, as well as the vertical loads from the weight of the structure, must then be transferred to the soil through the foundation pile. This load transfer is primarily the result of frictional forces between the pile surface, and the surrounding soil. A driven monopile is unrestrained at the mudline, and may rotate or translate as it transfers the horizontal forces. To effectively stabilize the dynamic wind turbine, foundation piles must be long enough to provide an interaction surface with the soil that fully transfers the load, without the pile deflecting excessively at the mudline or the pile tip.

Soils in the offshore environment are stratified and may be composed of layers of either sand, clay or a combination thereof, and then further characterized as loose, medium, or dense. The compactness of the soil is an indicator of how well suited it is to transfers the applied loads, but due to varying properties between layers.

2.15. Soil parameters

Data to accurately describe soil conditions at a wind farm site is relatively difficult to obtain. Soils may show significant variability, not just between wind farms, but between turbines within a single development. Detailed design therefore typically relies on in-situ samples taken from the proposed turbine locations.

Due to the highly site-specific nature of soil conditions, and the impact of the soil parameters on the support structure behavior, for the purposes of this report, a simplified, homogenous, single type soil profile of dense sand, characteristic to the North Sea, is assumed. The lateral resistance of this profile is determined using the API method with the following design parameters.

- Interface friction angle (sand) $\varphi_{soil} = 35^\circ$
- Interface friction angle between sand & steel $\delta = 30^\circ$
- Limiting shaft friction $f = 67$ kPa
- Bearing factor $N_q = 40$

- Limiting end bearing $q = 9.6$ MPa
- Submerged unit weight of sand $\rho = 10$ kN/m^3

The force exerted by the soil onto the foundation pile is expressed as an added stiffness in the structure below the seabed. Determining the value of this stiffness is discussed further in Chapter 4.

2.16. Additional environmental considerations

2.17. Marine growth

Marine growth is also incorporated into the design calculations. Density of the marine growth is taken as 1325 kg/m³. The table below shows the thickness of the growth with respect to MSL as provided in the applicable DNV standards.

Table 3: Marine growth elevations and thicknesses

Level [m]	*Thickness [mm]*
MSL+2 – MSL -10	100
MSL -10 to mudline	50

2.18. Scour

During the structure lifetime, motion of the pile at the seabed, along with the movement of the water profile, will cause looser soil and material to displace around the pile base, resulting in a form of erosion known as scour. Significant scour around the pile base may lead to a result in foundation stiffness which would require additional pile penetration to meet industry requirements for stability.

Common practice to limit the negative effects of scour, is the application of protective measures, such as dumping heavy rocks around the base, to hold down the smaller sand and gravel particles. The implementation of a Hybrid support structure will not affect the rate of scouring at the pile base, so for the purposes of this analysis it is assumed that some form of scour protection is applied, and is sufficient to prevent scour from altering the sub-structure performance, therefore scour will not be discussed further.

2.19. Corrosion

Steel in seawater is highly susceptible to corrosion. Similar to scour, for the purposes of this report is is assumed that some form of corrosion protection is present and that it has negligible effects on this analysis.

2.20. Basis of comparison monopile support structure

One issue with the Enersea report is that the selected base case support structure used for the comparison, shown in Figure 1-3, did not have equivalent bottom dimensions compared to the Hybrid option. Therefore, some of the perceived benefits of the Hybrid support structure, such as decreased pile penetration depth and shell thickness, may be attributed to the wider foundation base and not the reduced loading at the braced section. To better assess the potential benefits of the Hybrid concept, a new basis of comparison monopile support structure was established, with a 10-meter diameter base, tapering to a 6.5-meter diameter top section.

Initial dimensions for the shell thickness, taper angle, and embedded length, were established using the design guidelines for XL monopiles laid out in report ECN-E-16-069 by the Energy Research Center of the Netherlands [43]. The resulting support structure, shown in Figure 2-13, has a 10-meter base and an 84-mm shell thickness at the mudline, compared to the original Enersea reference monopile of 8.0 meters in diameter with 90 mm shell thickness.

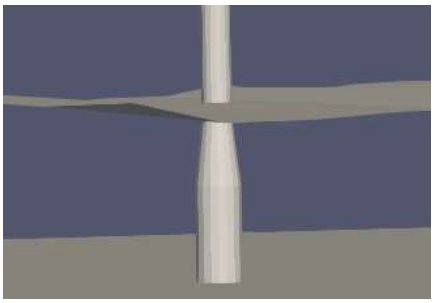

Figure 2-13: Reference monopile render with respect to waterline

3. General support structure model considerations

3.1. Modelling offshore wind turbines

Creating accurate mathematical models of offshore wind turbines can be difficult due to the wide variety of load types acting on the structure at different timescales, and with varying levels of predictability. An offshore wind turbine must be able to reliably perform under any of the load combinations that may be reasonably anticipated during its operational life. To guide designers through the process, engineering standards have been developed to prescribe the most relevant combinations to be assessed. Due to the dynamic interaction between the structural, mechanical, and electrical components of the structure during operations, two primary sets of standards are relied upon to model and design support structures; *Design requirements for offshore wind turbines,* from the International Electrotechnical Commission [23], and *Design of offshore wind turbine support structures* from Det Norske Veritas [11].

3.2. Sources of excitation

A compilation of the possible loads on an offshore wind turbine is shown in the Table 4 below. The loads in red are addressed in this report.

Table 4: Forms of loading on an offshore wind support structure

		Excitation Type			
		Steady	*Periodic*	*Stochastic*	*Transient*
Excitation Source	*Aero-dynamic*	• Average wind speed on rotor	• Aerodynamic imbalance from pitch misalignment	• Wind turbulence	• Extreme gusts
	Hydro-dynamic	• Current loads • Tidal fluctuations	• Breaking ice (not applicable)	• Irregular wave forces	• Extreme waves • Breaking waves
	Operational	• Dead weight loads of tower and nacelle, secondary steel, marine growth • Bending due to weight eccentricity	• Mass imbalance loads from blade passing • Tower shadow		• Braking forces • Grid cut-out • Yaw and pitch motions • Ship impact • Installation driving

3.3. Sources of model uncertainty in offshore wind turbine models

A comprehensive discussion of uncertainty in the mathematical modelling of offshore wind turbines is presented in [1], but those most relevant for this procedure are presented here.

3.4. Beam theory selection

An offshore wind turbine may be mathematically modelled simply as cantilevered beam, typically using either Euler-Bernoulli or Timoshenko beam theory, without yielding substantially different results [2]. Work by Arany and Bhattacharya et al. showed that even attempts to use more sophisticated beam models, with the inclusion of Rayleigh-beam inertia and shear deformation effects, improved model agreement with in-situ test data by less than 1%, indicating that the basic theories are sufficient to model the offshore wind tower. Some models elect to further simplify, by assuming a constant cross section representing an average over the entire length. This has been shown to result in both over, and underestimation, of structure stiffness and will be avoided in this analysis.

To further account for the changes in structural properties at the interface between the support structure and turbine tower, the connection is assumed to be a flanged, bolted connection, and is represented by a local added mass at the appropriate location in the beam model.

3.5. Soil Representation

Uncertainty relating to soil properties is harder to manage, both due to the uncertainty in the assigned soil properties, and uncertainty in the accuracy of the design codes themselves. Standard practice makes use of either the DNV or American Petroleum Institute (API) methods [11][36] for estimating soil stiffness, using P-Y curves, further discussed in Section 4.8. In recent years, the validity of the p-y curves for large monopile structures has been called into question, inspiring the Pile Soil Analysis (PISA) project to developed improved design methods for large piles. Until the completion of PISA, however, the old design codes still govern. The questionable validity of the current method, when applied to large offshore wind structures, comes from three main sources.

Models used to calculate soil-structure interaction for oil and gas jacket platforms, are calibrated using a relatively small number of cycles, as few as 200, but an offshore wind turbine is likely to experience upwards of 10^8 load cycles during a 25-year operable lifetime. The current models also predict soil stiffness degradation in the upper layer over the structure lifetime, but more recent work discussed in [13] indicates that densification of soil near the pile may instead result in increased soil stiffness for turbines supported on monopiles. Lastly, the models are based on oil and gas platforms with relatively low platform height and high mass, leading to a very different ratio of axial, shear, and bending loads, compared to an offshore wind turbine.

Despite their shortcomings, P-Y curves have been used in this analysis, but it is noted that this may lead to an overly conservative foundation design. To limit errors based on inaccurate soil modelling, soil is kept constant in this assessment of the Hybrid concept, but future investigation into the effects of different soil conditions on the structures performance is recommended, following the completion of the PISA project.

3.6. Damping estimation

Another notable source of uncertainty estimating the overall system damping ratio. System damping may come from five sources, in order of relevance, aerodynamic, structural, soil, hydrodynamic, and artificial damping from added motion dampers.

$$\zeta_{total} = \zeta_{aero} + \zeta_{struct} + \zeta_{hydro} + \zeta_{soil} + \zeta_{damper}$$

Aerodynamic damping is the result of the change in relative wind speed at the rotor due to the rotors own motion. When the wind exerts a force on the rotor, the rotor translates backwards, causing the relative wind speed with respect to the blades to go down, along with the resulting thrust force. As the turbine then recovers and moves back towards the wind, the relative speed increases, along with the applied force. The changing thrust force decreases the overall motion of the RNA as is oscillates. In the fore-aft direction, aerodynamic damping is variable with wind speed, but for the purposes of this report is taken to be an average 4% of critical, based on the recommended engineering estimate discussed in [22], based on the Blyth offshore wind farm. Aerodynamic damping still exists in the side-side direction, but is far less prominent, taken to be 1% for the purposes of this assessment. As a result, load cases in which waves are misaligned from the wind, will lead to greater fatigue damage than aligned cases in the fore-aft direction.

Incorporating the effects of aerodynamic damping is critical to not overestimating the damage caused by wave loads, as any structure motion in the fore-aft direction from the applied load, will be substantially reduced by rotor damping. Per industry best practices, it is also assumed at that for 10% of the operational life of the turbine, it is non-operational [52]. In fatigue calculations, these non-operational periods are represented by reducing the aerodynamic damping to the minimum value in all directions. Due to the reduced damping, these non-operational intervals may account for a substantial proportion of the overall fatigue damage accumulation. Regardless of direction, the structural damping ratio contribution to the overall system damping is taken to be constant at 1.0 % of critical damping, per standard industry practice.

Hydrodynamic damping for a structure this size is generally very small. Motions of the structure are substantially smaller than those of the water particles themselves, so small vibratory waves induced on the incoming waves by structure oscillation will not be noticeable. The second source of hydrodynamic damping, the shedding of vortices off the structure perimeter, will also be largely unnoticeable. Vortex shedding is the result of drag forces on the structure, which are an order of magnitude smaller than the inertia forces that dominate wave loading on large monopiles [38].

With respect to soil damping, there is considerable variation, with modelled values ranging from .17% up to 3% [54], therefore it has been omitted from this analysis. Lastly, no artificial damping has been introduced, so the last term may also be taken as zero.

3.7. Modal Analysis

The support structures peak response to dynamic loading will occur at the structures own natural frequency, so an accurate estimate of that frequency is critical for accurately estimating the resulting fatigue damage. It is also critical to design the support structure such that the first natural frequency lies

within the frequency band between the 1P and 3P operational frequencies of the turbine, to avoid resonance or resonance-related effects.

In shallower water, the structure frequency is governed by the RNA mass, tower stiffness properties, and soil stiffness, but as monopile diameter and length increase for larger turbines in deeper water, the support structure has a greater impact on the overall behaviour of the assembly. A simple first natural frequency calculation can be performed using the below equation, where L is the total structure length above the seabed, plus the effective fixity depth of the pile below the seabed, and φ is an approximation of the structure mode shapes.

$$f_1 = \left(\frac{1}{2\pi}\right) * \sqrt{\int_0^L EI(\varphi_z'')^2 dz / (m_{top} + \int_0^L m\,\varphi_z^2 dz)}$$

$$\varphi_z = 1 - \cos(\frac{\pi z}{2L})$$

The formula however does a poor job of capturing the effects of varying stiffness over the complete structure length. Structure stiffness near the water line especially, is a key indicator of vulnerability to wave induced fatigue, so a more refined computation of the natural frequency and mode shapes is required. An alternative calculation method for determining the first natural frequency of the structure by treating it as a discretized Euler-Bernoulli beam is provided in Chapter 4.

Uncertainty in determining the structure frequency arises not just from the calculation method, but from the fact that the structure frequency may not be consistent throughout its lifetime. Added mass from marine growth, changes in soil stiffness, and accumulated displacements form long term loading, may all effect the frequency. Therefore, assuming the natural frequency to be constant for the full operational lifetime may not be completely accurate.

3.8. Effects of increasing turbine size

As turbines continue to grow, designed structures in the "soft-stiff" band between the 1P and 3P frequency bands will present additional challenges. Larger turbines have longer blades, but due to tip speed limitations, operate at a lower rotational frequency. This low rotational frequency shifts the region between the 1P and 3P blade passing frequencies, to a lower frequency. Furthermore, as the rated power of the turbines increases, the turbines have taller towers and larger top masses, both of which lead to a reduction in the structure natural frequency. Figure 3-1 shows the 1P and 3P operation intervals for several common offshore wind turbines and shows the significant shift in soft-stiff region from a 2 MW turbine to an 8 MW turbine.

The allowable structure frequency band for the 2 MW turbine lies approximately between .4 and .5 Hz, and as shown in the figure, both the wind and wave spectra contain a negligible amount of energy in this range. In contrast, the soft-stiff region for the 6 and 8 MW turbines clearly overlaps with the wave energy spectrum. This overlap produces a dynamic amplification of the structure response to wave loads, and makes larger turbines much more sensitive to wave-induced fatigue damage.

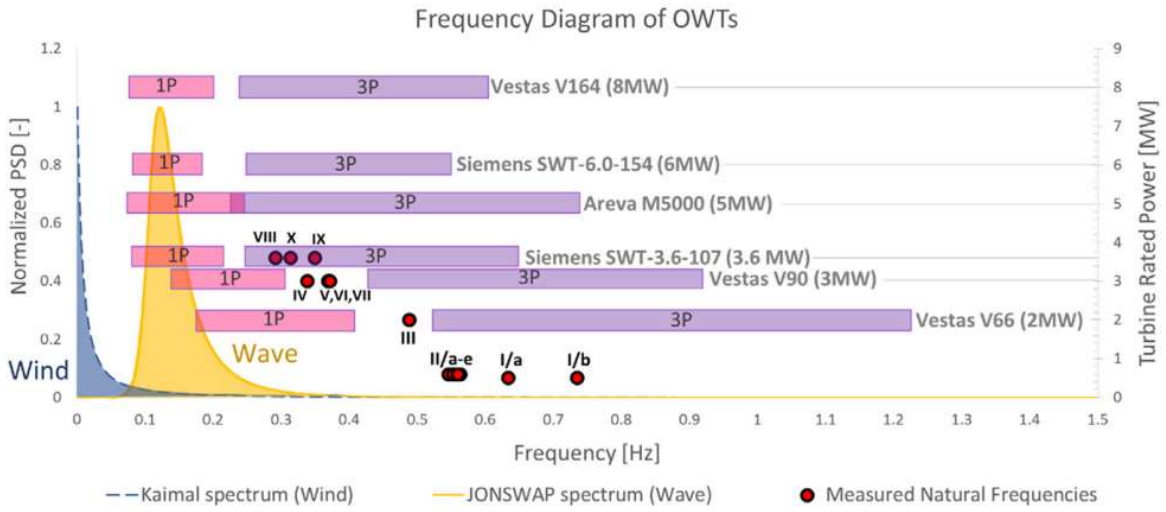

Figure 3-1: Excitation and operating frequencies for turbines ranging from 2 MW to 8 MW [1]

DNV Guideline [11] recommend that structures be design within the region bounding by the 1P and 3P excitation intervals with an added 10% buffer zone. It would technically be safer to design turbine supports in the stiff-stiff region, above the 3P excitation frequency, but to do so would require a cost-prohibitive quality or quantity of material to achieve adequate rigidity. Based on the assigned operating frequencies of the Vestas V164 turbine, and the 10% safety factor prescribed by DNV, the target soft-stiff design region for the Hybrid Monopile and reference monopile frequencies lies between .194 and .258 Hz.

3.9. Limit states

Beyond the frequency requirement for the offshore wind turbine, the structure must past a series of four limit state checks, composed of varying load combinations as prescribed by the standards [11][23].

- *Ultimate Limit State (ULS)* – the ability to withstand extreme loads
- *Fatigue Limit State (FLS)* – the ability to withstand cyclic loading over the structure lifetime
- *Serviceability Limit State (SLS)*- the ability to perform the intended function, for OWTs this refers to the displacement or rotation of the RNA with respect to the seabed
- *Accidental Limit State (ALS)*- the ability to withstand an unusual load, for OWTs, impact from a service vessel

Design of different components is generally driven by either the ULS or FLS state, so both are assessed during the early design stages, with the SLS and ALS conditions only investigated later in the process.

3.10. Ultimate limit state

In practice, the “extreme” loads used to determine the ultimate limit state result from assessing extreme environmental loads from wind and waves, with varying operating conditions of the turbine. IEC

standards designate a list of several key scenarios for which loads on the OWT should be assessed, including start-up, regular power production, fault during production, normal shut down, emergency shut down, and standstill/idling conditions. Combining these operating conditions with varying combinations of 1-year, 5-year, and 50-year maximum wind and wave loads leads to upwards of 50 load cases to assess.

Assessing these load cases however requires not only an immense amount of computational time, but detailed information regarding the control systems and specifics of the turbine itself. For early design of support structure, when this information may not be fully available, DNV provides a reduced set of load cases by which to perform the ULS assessment. For the purposes of this analysis, this reduced set of load cases, shown in Table 8, is used.

Table 5: Load combinations for simplified ULS assessment – return periods

Load	Water Level	Wind	Waves	Current
1	50-year	50-year	5-year	5-year
2	50-year	5-year	50-year	5-year
3	50-year	Cut-Out	5-year	5-year

As seen in Table 8, load cases where the 50-year wind and wave loads occur simultaneously are not considered. In a sea state where the maximum wave height would occur, wind speeds would be above the cut-out threshold of the turbine, leaving it in an idling state, so the 50-year, 50-year wind-wave combination would lead to an overly conservative design.

For the considered cases, it has been assumed that the wind and waves are fully aligned and approach the OWT directly. For the 40-meter North Sea site presented in Chapter 2, these load levels correspond to the following values.

Table 6: Wind, wave, and current values for ULS assessment

Load	Water Level	Wind	Waves	Current
1	42.5 m	36 m/s	13.5 m	1.4 m/s
2	42.5 m	28 m/s	17.0 m	1.4 m/s
3	42.5 m	24 m/s	13.5 m	1.4 m/s

The strength and stability of the monopile may be assessed using two different methods depending on the shell thickness. Initial monopile dimensions use a thickness corresponding to a D/t ratio of 120, the maximum allowable ratio for the NORSOK standard [37] to be valid. However, preliminary results from the Enersea report, and later confirmed by Matlab-based calculations, show that the reduced hydrodynamic loads on the Hybrid structure may allow for a thinner monopile shell, in which case DNV-RP-C202 [39] is applied.

3.11. Fatigue Limit State

The highly dynamic nature of offshore wind turbines results in a fatigue-driven design, whereby failure of the structure is due to long term damage accumulation from repeated cyclic loading, not from a single extreme incident. Unfortunately for designers, calculating the expected fatigue life of a structure requires the ability to predict all loading conditions over the course of the structure life, make computing fatigue loads accurately, a challenging and computationally expensive process. For a large offshore wind turbine, installed in deeper water, the process is particularly challenges, as the wind and wave loads will both contribute substantially to the overall fatigue damage.

3.12. Wind-Induced fatigue

For turbines installed on jackets and monopiles in shallow water, fatigue design is governed by wind loading on the rotor. Turbulent fluctuations in wind loads may lead to 10^9 load cycles in the structure lifetime, in contrast to waves which have lifetime load counts on the order of 10^7. The rapid fluctuations from turbulent wind are the primary design driver for engineering the turbine blades and tower. As turbines continue to stretch towards higher hub heights, and larger rotors, the resulting bending stresses also increase. Moving a turbine into deeper water further extends this moment arm, further increases the wind-induced bending stresses, coupled with an increase in wave loads.

3.13. Wave induced fatigue

In deeper water, for a large enough monopile, wave loads can overtake wind loading in terms of fatigue contribution [7]. Placing a turbine in deeper water has a compounding effect on the hydrodynamic loading. Deeper water can accommodate larger waves that would otherwise break in shallower water. Furthermore, deeper water provides a larger area on which to apply wave loads, and a larger moment arm for those wave loads, leading to larger mudline stresses in the support structure. In these cases, the water depth, structure geometry in the primary wave loading zone, and the structure frequency are all key parameters in determining wave-induced fatigue damage. As discussed in Section 3.4, the natural frequency of these large monopiles is likely to coincide with the wave excitation frequencies, resulting in an amplified response, and making wave-induced fatigue loads the governing design case.

Figures 3-2 and 3-3 compared the normalized contributions of wind and wave loading, to the fatigue loads in the longitudinal and lateral structure welds, for two different wind turbines installed at different water depths. For a 3.0 MW turbine installed in shallow water (10 meters), fatigue contributions from waves are only half that of the contributions from wind loading. Increasing the turbine size to 6.0 MW and the water depth to 40 meters results in a full reversal of the relationship, whereby the expected fatigue damage induced by wave loads is double that of wind loading.

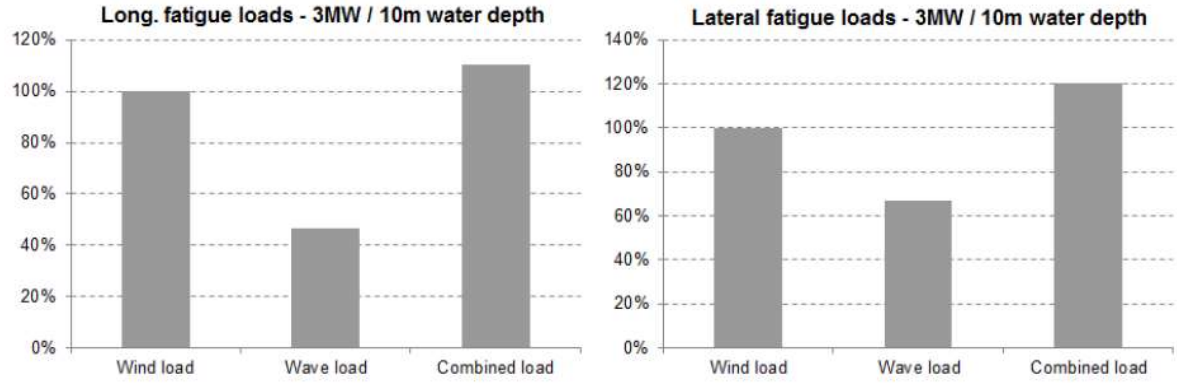

Figure 3-2: Fatigue contributions from wind and wave on a 3 MW turbine in shallow water [7]

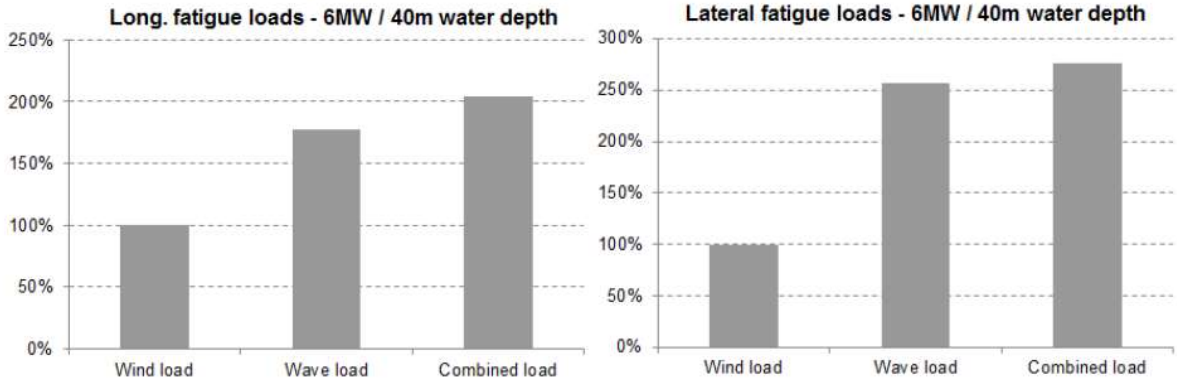

Figure 3-3:Fatigue contributions from wind and wave on a 6 MW turbine in intermediate water [7]

3.14. Fatigue calculation methods, time domain versus frequency domain

Since a key advantage of the Hybrid Monopile is the possibility to reduce wave-induced fatigue, wind and wave fatigue damage are calculated separately and then combined, as is common in the industry. Currently in the offshore wind industry, time domain methods are used for all detailed designs, as they are considered the only way to adequately account for non-linearities of the wind loading on the operational turbine. These methods, though highly accurate, are time consuming, computationally expensive, and require in depth knowledge of the specific aerodynamic and electrical components of the selected turbine. Furthermore, for certification of certain OWT components, the number of load cases required to assess fatigue damage accumulation over a structures lifetime rises well into the thousands, an unrealistic prospect for rapidly iterating through many configurations early in the early design phases.

The streamlined alternative to lengthy time domain simulations, is to instead perform the fatigue calculations in the frequency domain, by which results can be obtained in a matter of seconds or minutes as opposed to days. This reduction in time is due to the fact that fatigue damage calculated in the time domain is associated with a specific stochastic process, so numerous simulations must be run to cover all processes that the structure may experience. Alternatively, in the frequency domain, a single result covers

all possible stochastic processes in the frequency range [22]. In these methods, the response of a structure to an excitation is represented by a transfer function ,or functions, corresponding to a location of interest on the structure, i.e. the mudline or transition piece. A transfer function, often denoted by the symbol H describes the ratio between inputs and outputs of a system in the frequency domain.

$$H(\omega) = \frac{Output}{Input} \qquad i.e. \qquad \frac{Displacement}{Force} \qquad or \qquad \frac{Rotation}{Moment}$$

The spectrum of responses can then be calculated directly from the spectrum of possible excitations via the generic transfer function $H(\omega)$.

$$S_{response}(f) = |H(\omega)|^2 * S_{excitation}(f)$$

For this analysis, the most useful transfer functions are those that relate the bending stress at an elevation point along the structure, to the amplitude of the environmental load to rapidly evaluate several different sea states.

$$H(\omega) = \frac{WaveAmplitude}{Mudline\ Bending\ Stress} \qquad or \qquad H(\omega) = \frac{WindSpeed}{Mudline\ Bending\ Stress}$$

The derivation of these transfer functions is discussed further in later chapters. It is commonly accepted in the industry to treat wave loads in this manner. Wind loads however, exhibit non-linear behaviour do not lend themselves as clearly to frequency domain computations. Several researchers have worked to further develop these decoupled fatigue calculation methods.

Work by Kuhn [24], provides a framework for combining frequency domain based wave load calculations, with time-domain computations for wind loads. Van der Tempel [22] instead presents a method in which the loads are still decoupled, but are both handled in the frequency domain, the results of which showed good agreement with time-domain data from four operational wind farms in the North Sea. Each of these methods is utilized and discussed further in the later chapters of this report. To perform the initial rapid assessment of fatigue from waves only, on numerous potential iterations of the Hybrid Monopile design, the method presented by Seidel [8], which only considers the first mode of the structure and disregard aerodynamic damping, was used and is explained further in Chapter 4.

3.15. Serviceability limit state

Serviceability limit state criteria are defined by individual turbine manufacturers and may vary based on hub height or generator type, but DNV codes also offer generalized guidelines than can be used for non-turbine specific design. Recommendations include:

a) Maximum pile deflection at the mudline of .03*pile diameter [11].

b) Maximum nacelle tilt of .25 degrees*, or a maximum RNA displacement of 2.0 % of the distance from the seabed* [12].

*Individual manufacturers have specific requirements for the maximum nacelle displacement, but b) may be used as a rule of thumb in the absence of that information.

3.16. Accidental limit state

The accidental limit state check examines the response of the structure to an inadvertent collision by a maintenance vessel. The purpose of the assessment is to confirm that the accidental load can be absorbed by the plastic deformation of the steel, and that the total effect of the impact does not exceed the plastic limit, or risk the overturning of the structure towards the vessel, because of the load.

For detailed design, the codes provide formulas for the estimation of the impact load which considers the size, shape, and speed of the incident vessel. When the detailed of the vessel are not available, Germanischer Lloyd recommends assigning a transient impact load of 5 MN [12].

4. Determining initial Hybrid Monopile configuration

4.1. Section length

One of the obvious problems with the initial Hybrid design, highlighted by the Enersea report, was the vulnerability of the brace members to buckling. The 30-meter brace lengths, led to members with high slenderness ratios, 89 and 119 for the 3x2 and 6x2 configurations respectively. Comparatively, offshore jacket members are typically designed with a slenderness ratio on the order of 60-90. Therefore, the first step in the design iteration was to determine a range of shorter section lengths that would reduce the buckling risk, without significantly compromising the demonstrated benefits of the Hybrid design, with respect to structure weight and wave loading reduction.

To minimize the brace length and still maintain the fatigue benefits, the length was set to target the area in the water column where the wave groups that contribute substantially to the fatigue life calculations act. Based on the S-N curve for steel in seawater, provided in DNV-RP-C203 [58], wave states without a minimum of 10^6 anticipated cycles over a 27-year structure life, were not considered.

This threshold corresponds to the end in the SN-curve where the slope changes, known at the knee-point N_k, and limits the considered waves to those with significant wave height H_s between .5 and 5 meters. For each wave, the acceleration and velocity profiles were plotted against water depth to identify a depth beyond which increasing the hybrid section length does not provide significant additional benefits. Figures 4-1 and 4-2 show the resulting profiles for water depths of 30, 40 and 50 meters.

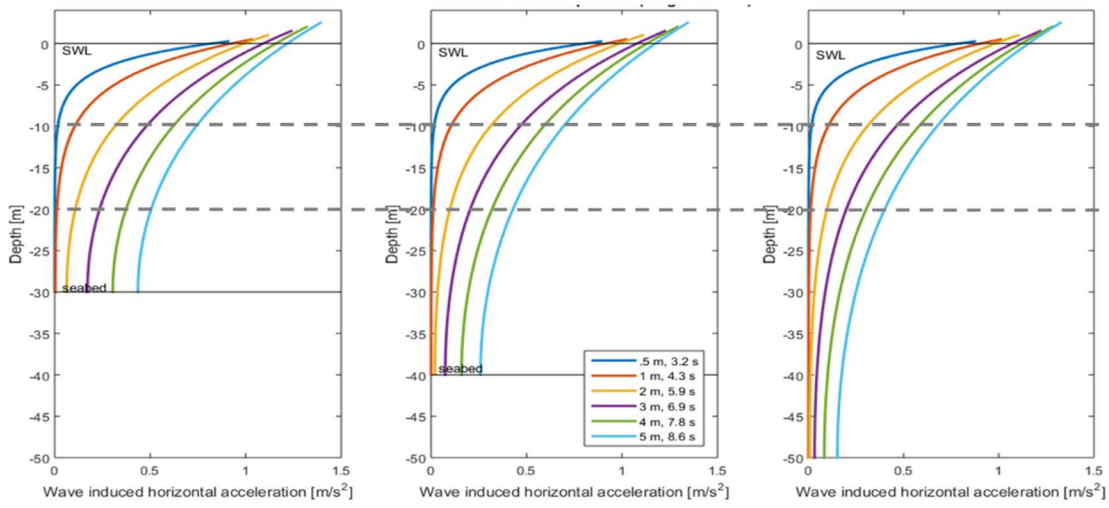

Figure 4-1: Wave particle acceleration with respect to depth for primary fatigue wave states

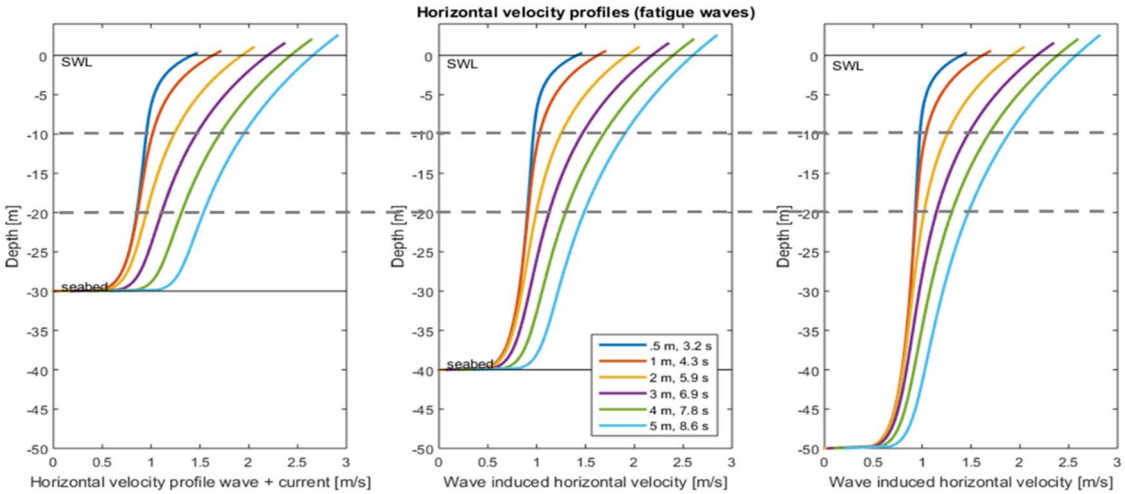

Figure 4-2:Wave particle velocity with respect to depth for primary fatigue wave states

Attention was paid primarily to the acceleration profile due to the inertia dominance of the wave loads discussed previously. Comparing the profiles for the different waves, it was possible to visually approximate a region in which the values level off. The region, located between 10 and 20 meters below the still water level, is consistent across 30, 40 and 50-meter water depths.

The initial upper bound of the hybrid section was selected to be:

$$Tidal\ range + \frac{1}{2} * H_{s(5.0\ m)} = 6.0\ m$$

Using the 10-20 range as the lower bound resulted in a possible Hybrid section length range of 16 - 26 meters.

4.2. Member number and arrangement

Though the Enersea report did not recommend increasing the number of members, due to the previously mentioned concerns regarding insufficient batter angles, a 4x2 configuration was introduced into the analysis. The reduction in length of the hybrid section, without altering the top and bottom ring dimensions, makes it possible to still achieve a desirable batter angle even with the additional member pair.

Shifting from a 3x2 to 4x2 configuration is wise from both ULS and FLS perspectives. In the ULS case, there are certain orientations of the 3x2 structure which result in a single pair of members carrying all the compressive or tensile loads in response to the environmental loading, whereas in the 4x2 configuration, two brace pairs are available to carry the tensile or compressive loads, regardless of the wind-wave loading direction. The 4x2 distribution about the ring is also desirable in that despite the addition of two additional members, the wave loading area from most approach directions does not substantially increase, due to a substantial overlap of the members, known as sheltering.

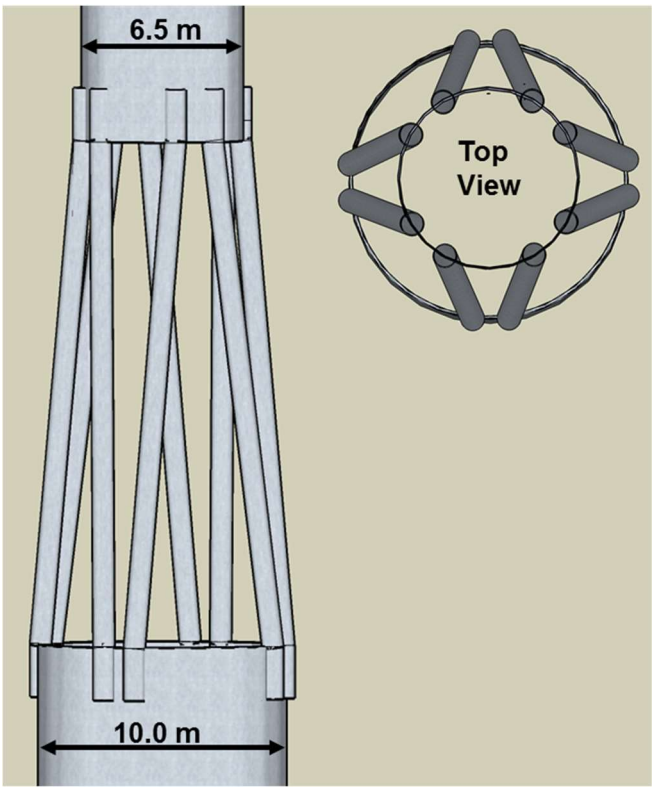

Figure 4-3: Side and top views of 4x2 Hybrid arrangement

Sheltering values were calculated as a function of the distance between the upper and lower rings, as there is more overlap near the top where the members are closer together. Figure 4-3 shows side and top views of the 4x2 configuration, with the side view corresponding to the approach angle where the maximum available wave loading area occur.

Additionally, the symmetric 4x2 option is advantageous from a design perspective, as the natural frequencies in the fore-aft and side-side directions will more likely converge to a single value. In the case of an asymmetric design, the natural frequencies of the structure on the principle axes form two separate peaks to be excited by wind and waves. A two-peak structure does have the potential to spread the structure fatigue response across two different frequencies, but it can be difficult to create an asymmetric design in which both peaks lie in the soft-stiff region. In a symmetric design, these peaks converge, simplifying the design process.

4.3. Member size – initial dimensioning

Initial brace dimensioning is based on the goal of maintaining the same load carrying area as the monopile shell, while also keeping the outer diameters of the braces as small as possible to reduce the available wave loading area. This results in using very thick-walled members with a D/t ratio of 20, as limited by the applicable design codes [11][23][37]. For the 4x2 configurations the required brace area per member is 1/8 the area A of the turbine tower base.

$$A_{tower} = \frac{\pi}{4} * \left(D_o^2 - \left(D_o - 2 * \frac{D_o}{20} \right)^2 \right) = 1.0132\ m^2$$

Required brace cross section diameters:

$$\textbf{4x2 -}\ A_{brace} = \frac{A_{tower}}{8} = .12665\ m^2 \Rightarrow D = .9212\ m\ \ and\ t = 46.1\ mm$$

Resulting in selected dimensions of

4x2: 850 x 42.5 mm

For the purposes of reducing the number of variables in the simplified concept evaluation stage, the D/t ratio of 20 is kept constant throughout this report.

4.4. Equivalent beam model

The dimensioned structure is then modelled mathematically as an Euler-Bernoulli beam discretized into 1-meter elements, each with a defined mass and stiffness, with the following equation of motion.

$$\rho A\ddot{u}_1 + EIu_1^{iv} = 0$$

These elements form five distinct sections with different properties, highlighted in Figure 4-5.

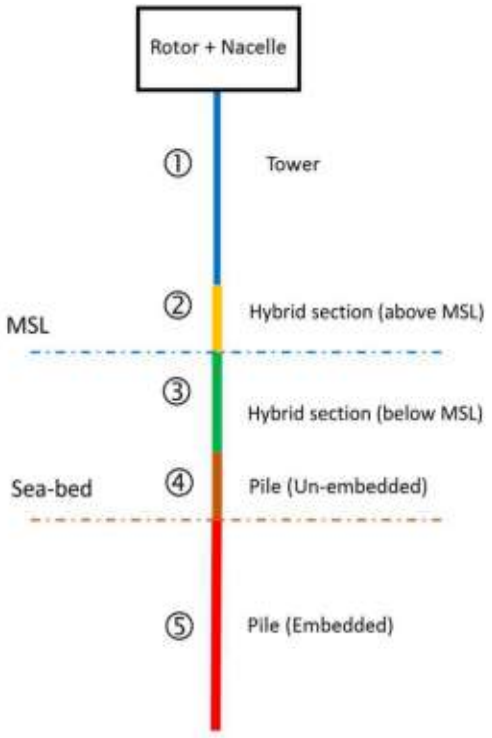

Figure 4-5: Equivalent beam model discretization – modified from [59]

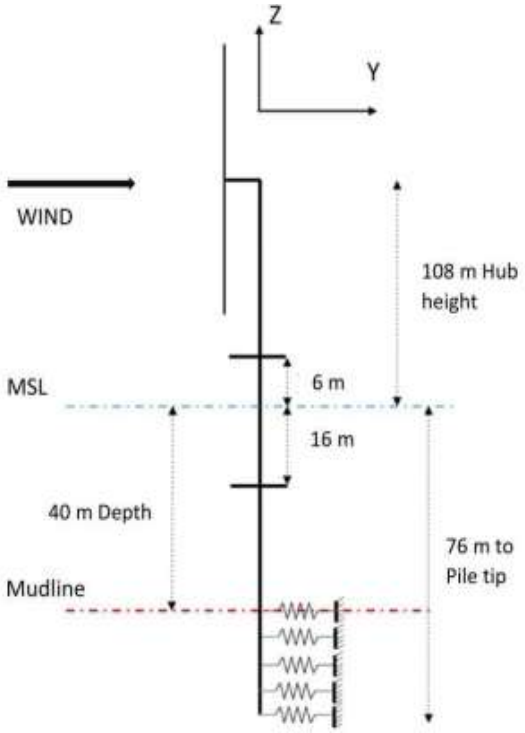

Figure 4-4: Equivalent beam model, relevant design elevations – modified from [59]

At the top, the rotor nacelle assembly is simply defined as a concentrated point mass. Added masses of 1500 kilograms are also included at the 1:2 and 3:4 junctions to account for the added mass of a flanged connection at these junctions. Diameter and thickness distributions along the blue "tower" section, are taken from the Enersea report. The embedded (red) and unembedded (orange) pile sections have identical geometry, but the embedded section requires the additional of springs to define the soil stiffness. The yellow and green segments depict the hybrid section. Mass per unit length in this section is easily calculated using the cross-sectional area of the members and the material density. To calculate the 2nd moment of area I, and the resulting stiffness, in each slice of the braced region, the parallel axis theorem is applied,

$$I_{centerline} = I_{brace} + A_{brace} * r(z)^2$$

with,

$$I_{brace} = \left(\frac{\pi}{64}\right) * (D_{brace}^4 - (D_{brace} - 2t_{brace})^4)$$

where $r(z)$ is the distance from the centreline of each member to the centre of gravity of the segment as it varies with the elevation z. Having defined the properties of each 1.0 meter element, the beam model can be reworked into the matrix form of the standard equation of motion, shown below.

$$\boldsymbol{M}\ddot{u} + \boldsymbol{K}u = 0$$

The mass term can be handled directly. A diagonal mass matrix populated by the product of the material density of streel and the cross-sectional area of each 1.0-meter section along the beam, and then adding the rotor-nacelle mass to the final corner element of the matrix. Added masses for the flanged connection point are added to the corresponding elements.

To construct the stiffness matrix ***K***, an expression must be derived for the fourth spatial derivative u_1^{iv} in terms of the displacement u, such that,

$$u_1^{iv} = [\Phi] * u$$

To compute this matrix $[\Phi]$ to transform the equation, the finite difference method was applied, assuming the structure acts as a fixed-free cantilever beam.

4.5. Derivation of stiffness matrix using the finite difference method

The 4th spatial derivative term can be derived in terms of the displacement u of each discretized element using the finite difference method. Using this method, the 4th slope of an element can be found using lower order derivatives of four neighboring elements. This can be visualized using the 5-element subsection of the beam in the figure below.

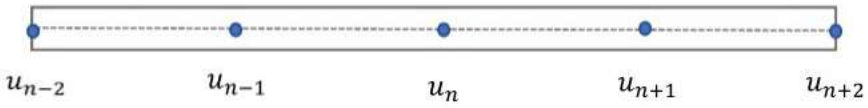

Taking the node location *n* to equal 3, the second spatial derivative between u_2 and u_4 can be found by the difference in the adjacent first derivatives.

$$u'_a = \frac{u_3 - u_2}{l} \quad and \quad u'_b = \frac{u_4 - u_3}{l}, \qquad \xrightarrow{yields}$$

$$u'' = \frac{\frac{u_3 - u_2}{l} - \frac{u_4 - u_3}{l}}{l} = \left(\frac{1}{l^2}\right) * (u_4 - 2 * u_3 + u_2)$$

Extending this process to other adjacent nodes and higher order derivatives follows the form of a Taylor series expansions, leading to an expression of the 4th derivative at node *n*=3 in terms of five adjacent nodal displacements such that,

$$u^{iv} = \left(\frac{1}{l^4}\right) * (u_5 - 4u_4 + 6u_3 - 4u_2 + u_1)$$

which can then be extended to all elements in the discretized beam model to produce the corresponding stiffness matrix.

$$\frac{EI}{l^4} * \begin{bmatrix} 1 & -4 & 6 & -4 & 1 & 0 & 0 & 0 & 0 & 0 \\ 0 & 1 & -4 & 6 & -4 & 1 & 0 & 0 & 0 & 0 \\ 0 & 0 & 1 & -4 & 6 & -4 & 1 & 0 & 0 & 0 \\ 0 & 0 & 0 & 1 & -4 & 6 & -4 & 1 & 0 & 0 \\ 0 & 0 & 0 & 0 & 1 & -4 & 6 & -4 & 1 & 0 \end{bmatrix} \ldots..]$$

Since computing this stiffness at a node requires information from two additional nodes in each direction, at the ends the beam, the formulation of the stiffness at nodes *1, 2, N, and N-1,* would require information for non-existent nodes. Eliminating those non-physical nodes from the formulation requires additional equations in the form of boundary conditions at the seabed and the rotor. A more complete derivation of the matrix and the corresponding boundary conditions can be found in [55].

The mass and stiffness matrices may then be used to compute the eigenvalues and vectors from the following.

$$EIG = M^{-1} * K$$

The real components of the square roots of the eigenvalues give the undamped structure natural frequencies and the eigenvectors provide the mode shapes. The derivation of a matrix to represent the assigned damping percentages, discussed earlier in Chapter 3, could be done using,

$$\beta = 1\% = \frac{c_{\text{damping}}}{c_{\text{crtitical}}} = \frac{C_{damping}}{(2\sqrt{K * M})}$$

Damping terms are excluded for the purposes of the modal analysis, but are introduced for the fatigue assessment.

4.6. Determining soil stiffness

NEN-EN-ISO 19902 and DNV offshore standards [60][11] both advise that a finite element model based on p-y curves be used to assess the soil resistance for laterally loaded foundation piles, wherein the pile is modelled as a series of slices each supported by a non-linear spring, the stiffness of which is calculated using the previously discuss P-Y curves. The stiffness of the soil varies with depth, so even though a single homogeneous soil condition has been assumed, it must be discretized into several layers to obtain an accurate result. It was determined that the subsequent modal analysis converges when five or more layers are considered. After dividing the soil into those five layers, corresponding to six springs, as shown in Figure 4-6, the stiffness per unit length can be calculated at the mid-point of each layer as follows,

$$K_{soil} = \frac{P(n+1) - P(n)}{y(n+1) - y(n)}$$

where n is the soil layer number and the P and y values at the different layer heights are determined using the formula below, where A is a dimensionless value calculated from the DNV/API codes, P_u is the ultimate strength of the soil in [N/m], and k_S is a function of the internal friction angle.

$$p = Ap_u \tanh\left(\frac{k_S H y}{AP_u}\right)$$

The stiffness per unit of length E_{py} is calculated at each layer using the simple relation below, where y is a value of displacement.

$$E_{py} = \frac{p}{y}$$

This produces the stiffness values at each of the 6 layers (shown Table 7). For each element of the Euler-Bernoulli beam model that lies below the seabed, this stiffness value E_{py} is added to the modulus of elasticity E in the stiffness matrix formulation.

Table 7: Soil layer stiffness

Layer	Stiffness [N/m]
1	4.809E+07
2	1.443E+08
3	2.404E+08
4	3.364E+08
5	4.321E+08
6	5.272E+08

The embedded pile length to which the springs are applied is estimated as 3.5 pile diameters, as recommended in [43]. With the addition of the soil springs below the seabed, the equivalent beam model is fully formulated.

4.7. Initial ULS Evaluation

To determine the optimum braced section length within the determined range, confirm the adequacy of the selected brace dimensions, ULS wind and wave loads were calculated for each possible section length. This preliminary ULS check is based on a conservative combination of the maximum expected with and wave loads. For convenience and speed, a deterministic approach to the analysis is used whereby variable loads are considered to have a single value and then assigned a safety factor, taken from the applicable DNV design codes [11]. Wind, wave and current loads are treated as all being fully aligned and the environmental loads are assigned a safety factor of 1.35. Computations of the cumulative base shear and overturning moment loads on the structure are then calculated for each possible Hybrid section length from 15-25 meters as established in Section 4.1.

For this case, the maximum factored operational wind load is taken as 2.4 MN applied at the rotor, and the wave loading per unit length corresponds to the 17.0 meter, 50-year extreme wave.

Figure 4-6 shows the shear accumulation in the structure below the transition piece. Since the rotor load is the only force applied above the crest of the extreme wave, the shear load in the structure is constant between those points. The reduction in available wave loading area from the Hybrid section, shows noticeable reduction in shear accumulation near the waterline and a total base shear reduction at the mudline. These reductions range from 7.5% to 20.2 % as shown in Table 8.

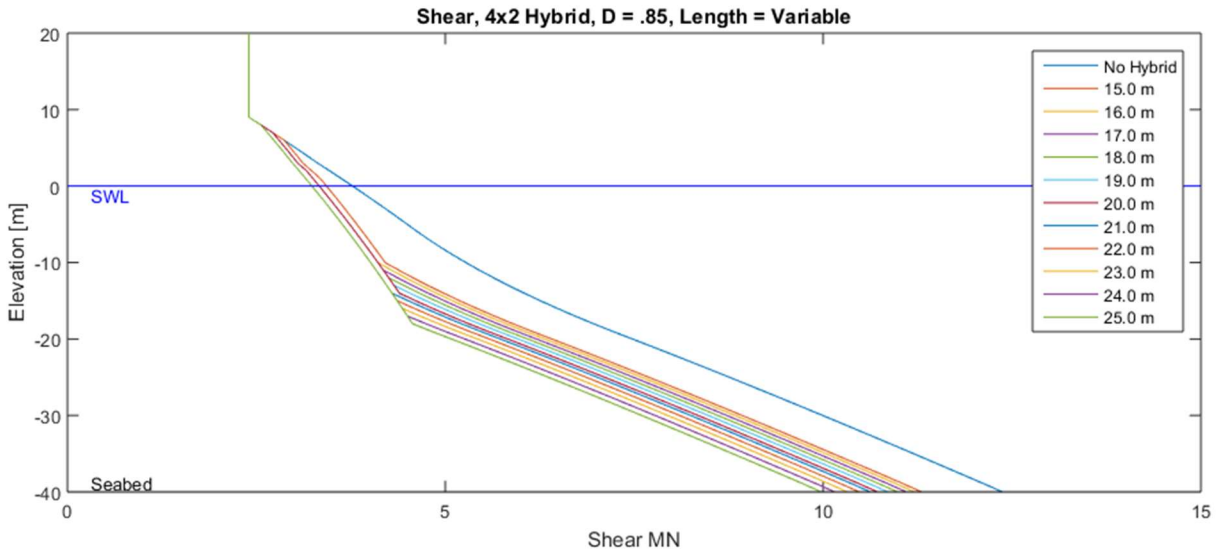

Figure 4-6: Shear accumulation in MN with respect to Z for a range of Hybrid section lengths

The corresponding for the moment accumulation in the structure is shown in Figure 4-7.

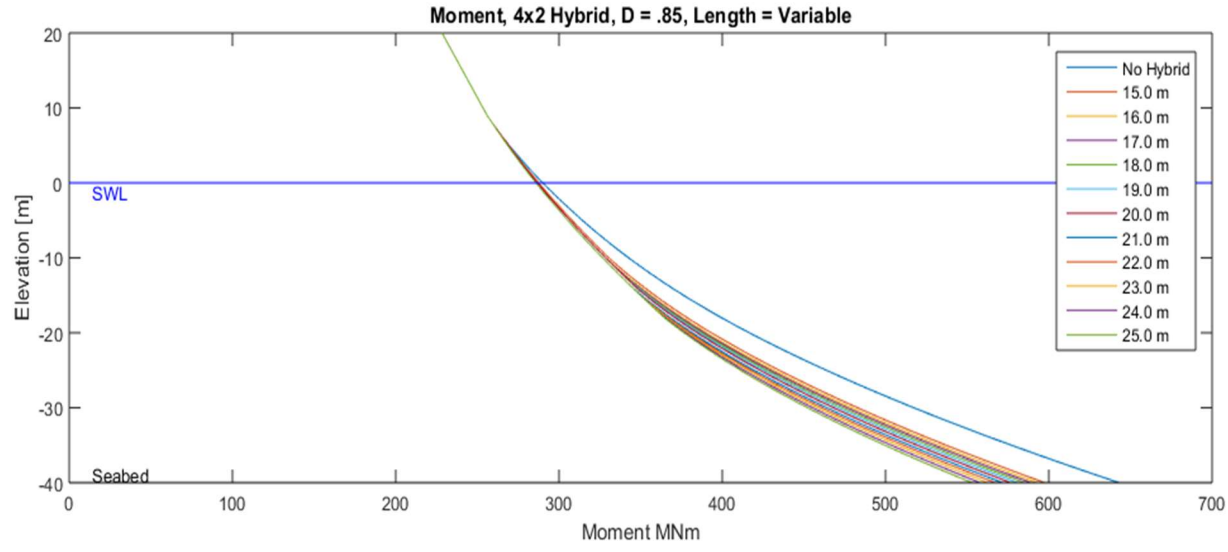

Figure 4-7: Moment accumulation in MN with respect to Z for a range of Hybrid section lengths

The overturning moment depends not only on the applied load, but also the distance from the mudline of that application. Wind loading is more dominant in this cases in this case due to the high hub heights, so though wave loading accounts for 80% of the total base shear, it accounts for only 40% of the overturning moment. Since the Hybrid configuration has no effect on the wind loading, mudline moment reductions are more modest, ranging between 6.9 and 13.9% for 15 and 25-meter Hybrid section lengths, respectively.

Table 8 shows the base shear and mudline moment results for each iteration of the structure and the percent reduction compared to the reference case.

Table 8: ULS load reduction for various Hybrid section lengths (4x2 arrangement)

Hybrid Length (m)	Base Shear (MN)	% Reduction	Mudline Moment (MNm)	% Reduction
No Hybrid	12.38	0.0%	642.00	0.0%
15	11.45	7.48%	597.41	6.95%
16	11.30	8.72%	592.57	7.70%
17	11.15	9.97%	588.85	8.28%
18	10.99	11.23%	584.96	8.89%
19	10.83	12.50%	580.81	9.52%
20	10.68	13.77%	576.52	10.20%
21	10.52	15.05%	571.50	10.98%
22	10.36	16.34%	567.05	11.67%
23	10.20	17.63%	562.47	12.39%
24	10.04	18.93%	557.7	13.13%
25	9.88	20.23%	552.96	13.87%

Prior to selecting an optimum brace length, it was necessary to confirm that the initial brace dimensions computed in Section 4.3 can sufficiently carry the applied ULS loads.

4.8. NORSOK check for individual member loads

To determine the behaviour of the individual members under ULS loading, the NORSOK N-004 design standard for tubular members was applied. The complete standard can be found in [37], but a summary of the relevant computation is provided here. Calculations were performed under the assumption of S355 steel with the following properties.

$$E = 2.1e5\ MPa, \quad \rho = 7850\frac{kg}{m^3}$$

The maximum applied loads on the braces were taken as the shear and bending loads presented in the previous section, with the addition of an axial dead weight load from the tower top mass, and tower mass above the brace members. Maximum loading is taken to occur at the member cross section just above the connection point with the base monopile, where the moment arms for wind and wave loads are the

longest. The complete load in each this structure segment is then distributed across the 8 brace members. Axial loads are assumed to be shared equally across the members. Bending loads are distributed based on the distance from each members centerline to the neutral bending axis, with members farthest from the neutral bending axis, in this case the X-Z plane, carrying a larger share of the bending moment. The validity of this sharing scheme is discussed further in Chapter 5.

Recalling the top view of the structure in Section 4.2, the member pairs at the front and back of the ring are all equidistant from the X-Z plane, so the in the case of a fully aligned load, any one of them may be considered the governing member. The selected governing member is assessed in compression, bending, shear, and torsion. Then the member is evaluated under combined axial compression and bending, and required to meet two unity conditions to assess vulnerability to local buckling.

The first unity condition simply sums the strength utilization of the member under axial and bending loads separately, ignoring any interaction between them,

Condition 1:

$$\frac{N_{applied}}{N_{resistance}} + \frac{M_{applied}}{M_{resistance}} \leq 1.0/y_M$$

where $N_{resistance}$ is the design axial compressive force, and $M_{resistance}$ is the design bending moment, and y_M is the material safety factor for steel. Results showed most of strength utilization to come from resisting the applied bending loads, with resistance to dead weight loads accounting for less than 10% of the total utilization.

In the second unity condition, a reduction factor is applied to account for a decrease in the members ability to resist bending as a result of the concurrent axially compressive load.

Condition 2:

$$\frac{N_{applied}}{N_{resistance}} + \left(\frac{1}{M_{resistance}}\right) * \left[C_{red} * \frac{M_{applied}}{1 - \frac{N_{applied}}{N_{Euler}}}\right] \leq 1.0/y_M$$

With C_{red} as the reduction factor assigned in the code, equal to .85 in this case, and N_{Euler} equal to the critical Euler buckling limit of the tubular.

$$N_{Euler} = \pi^2 * \frac{EA}{\left(\frac{kl}{i}\right)^2}$$

with A as the cross-sectional area of brace member, and the denominator $\left(\frac{kl}{i}\right)^2$ as the slenderness ratio of the brace, making the calculation sensitive to changes in the brace length or diameter. To determine the minimum brace diameter and maximum brace length which would still resist local buckling, the NORSOK criteria checks were repeated for brace lengths of 15-25 meters in length and with outer diameters of .7 to 1.05 meters. The results of the iterative checks are shown in Figure 4-9.

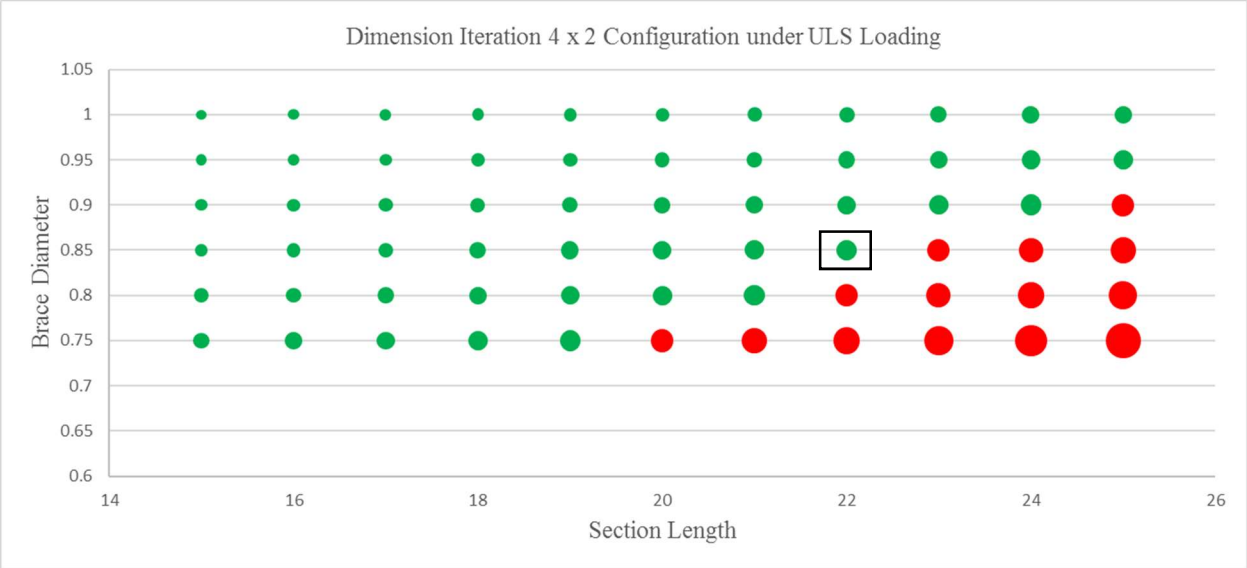

Figure 4-8: Results of iterative NORSOK unity check to identify viable member dimensions

Green dots represent length-diameter pairings which successfully meet both NORSOK conditions, thus making them viable Hybrid Monopile brace options and red dots show combinations that failed one or both conditions. Markers are scaled with respect to the unity check results. Markers along the diagonal separating the viable and non-viable configurations have values just below or above the unity limit. Based on these results, a brace length/diameter combination of 22/.85 meters was selected, as indicated by the squared data point.

4.9. Yield check

Though the brace members are a critical design location in the structure, the local and global stability of the complete structure must also be performed. Using the extreme loads corresponding to the selected 22-meter Hybrid section length, a yield check is performed to ensure that the stress at any point in the structure does not exceed the yield strength of steel $\boldsymbol{S_y}$. For each discretized segment of the beam model the following inequality is assessed.

$$\frac{N_{axial}}{A} + \frac{M_{bending}}{W} < \frac{S_y}{y_M}$$

with,

N_{axial}	Vertical load from turbine and structure weight	[MN]
A	Cross-sectional area	[m^2]
$M_{bending}$	Bending moment	[MNm]
W	Elastic section modulus	[m^3]
S_y	Yield strength steel (355)	[MPa]
y_M	Material safety factor (1.1)	[-]

yielding,

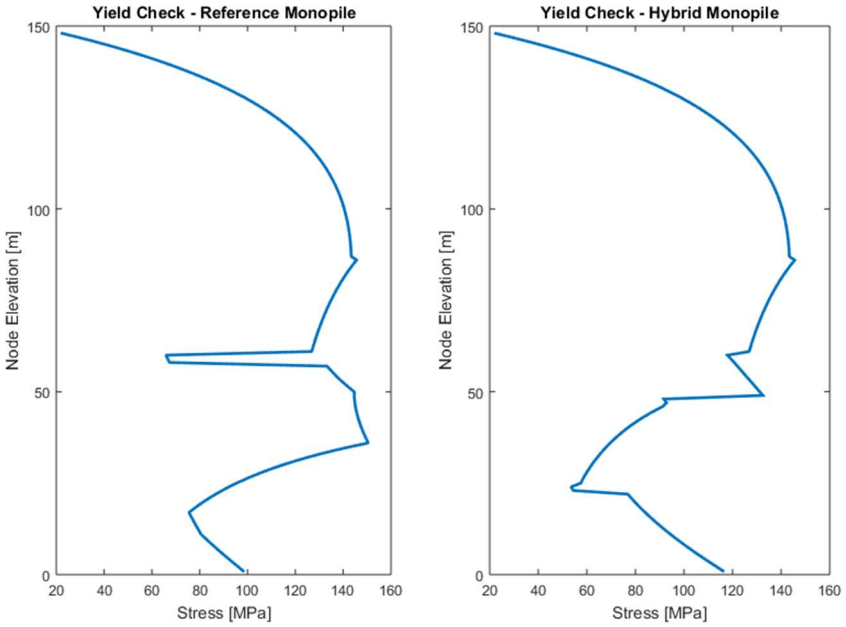

Figure 4-9: Yield check results under ULS loading for reference monopile and initial Hybrid Monopile

As can be seen in Figure 4-8 above, the cross-section stress throughout both the reference monopile and Hybrid structures does not approach the yield stress.

4.10. Pile embed length

After confirming that the applied ULS loads do not result in plastic hinge failure of the monopile shell, the stability of the foundation is assessed to ensure that the applied loads do not exceed the foundations' ultimate lateral capacity. Again, applying the base shear and overturning moment corresponding to this 22-meter section length, and the soil stiffness values established in Section 4.5, the displacement and rotation of each embedded pile element is calculated using the Matlab-based Foundation Pile Analysis Tool developed at TU Delft [51]. The pile penetration length for each of the two structures is then adjusted to achieve compliance with three criteria under the applied load.

i. $Mudline\ displacement < .03 * D_{pile}$
ii. $Mudline\ rotation < .025\ degrees$
iii. $Pile\ toe\ displacemn \quad .02\ meters$

To comply with all three criteria, the base case monopile requires an embedment depth of 37 meters, compared to the Hybrid Monopile which only requires 33 meters of pile penetration. Based on these results, the soil stiffness springs are updated applied to the appropriate foundation length in the equivalent beam model. The mass matrix of each model is also updated to reflect the corrected length.

4.11. Modal analysis

Using the updated mass and stiffness matrices, the first three natural frequencies for the both the reference monopile and Hybrid Monopile were calculated. As a validation step, second modal analysis was performed on the structure, modeled as a Timoshenko beam, using an offshore wind support structure analysis program currently being developed at TU Delft [59]. The results from the two methods were nearly identical for the first structure natural frequency in the reference and Hybrid case. Figure 4-10 depicts the calculated 1st natural frequency for each with respect to the environmental spectra, turbine operational regions, and the DNV prescribed safety limits.

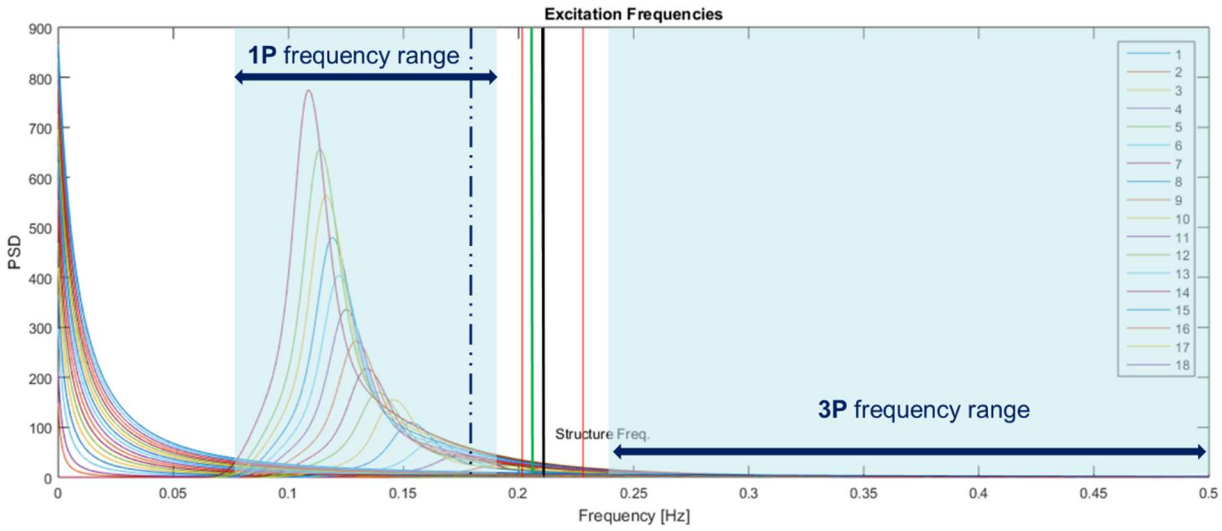

Figure 4-10: Base case (black) and Hybrid structure (green) frequencies & DNV limits (red) against excitation spectra and turbine operating intervals

Though the Hybrid Monopile configuration results in a low natural frequency of .205 Hz compared to .226 Hz for the reference monopile structure, both fall within the allowable soft stiff region, including the ten percent DNV buffer.

To determine which structural modes to include in the fatigue assessment, the 2nd and 3rd vibratory modes were also calculated using both each beam formulation. Results are shown in Table 9 and the mode shapes are plotted in Figure 4-11.

Table 9: Calculated frequencies for different beam models

Frequency	Euler-Bernoulli	Timoshenko
1st	.205	.202
2nd	.789	.735
3rd	1.636	1.708

The normalized mode shapes in Figure 4-11 would indicate substantial potential for vibration about the waterline in the 2nd mode, and would indicate that the 2nd mode is important for fatigue assessment.

However, it is apparent from the results shown in Table 8, that the second and third modal frequencies of the structure fall well above the wave forcing spectra, and above the maximum limit of the 3P operational range.

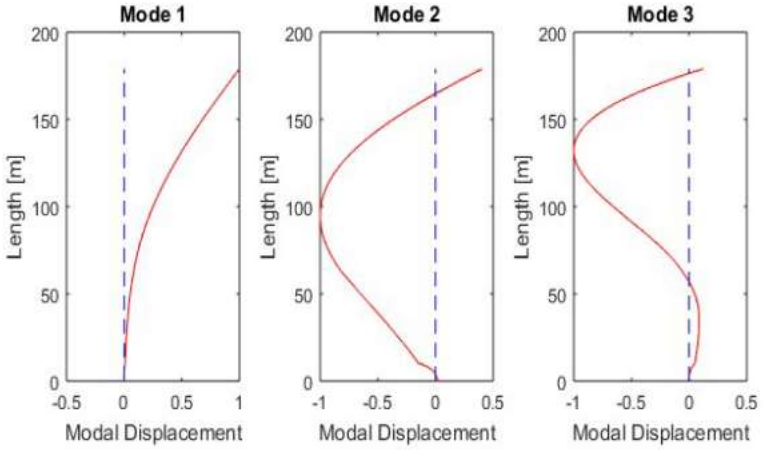

Figure 4-11: First three normalized mode shapes for the Hybrid Monopile

Based on this result, the 1st mode will drive the structure response and is the only mode retained in the fatigue analysis. Furthermore, since it has been assumed that the structure is axially symmetric, and each axis may be reduced to a 1-DOF system for the purposes of this report. Prior to proceeding with a fatigue life assessment, ULS load and modal analysis results from this Chapter are verified using a dynamic three-dimensional model of the structure.

5. Model verification using simulation software

To validate the initial environmental loading calculations, modal analysis results, and gain additional insight into the behavior of the hybrid monopile, a dynamic model of the 4x2 Hybrid Monopile support structure, with the established 22-meter section length, was prepared using the open-source software FAST, developed by the National Renewable Energy Laboratory in Boulder, Colorado. The FAST program is based on advanced engineering models and allows for the modeling of offshore wind turbines under coupled loading, joining models for aerodynamic loads, hydrodynamic loads, and control/electrical system dynamics.

FAST is an extremely powerful program, capable of producing highly accurate simulation results, suitable for detailed design certification in accordance with Germanischer Lloyd design standards. This accuracy comes with a high computational price tag. A simulation for 600 seconds of turbine operation can take up to two hours to complete on a standard PC, depending on the complexity of the selected load models. For the purposes of this project is was not feasible to use the dynamic simulation model for all the relevant load cases. Instead a selection of load cases, including wind only, wave only, and coupled loading, with varying degrees of misalignment were run to validate and calibrate the Matlab-based equivalent beam model.

5.1. Structure modelling using FAST

Extensive descriptions of the modelling assumptions made in the FAST program are available in the cited user and theory manuals [48-49], but for this set-up the most relevant are listed below:

1. 3-Dimensional turbulent wind field with user-defined turbulent intensity and turbulent length scale per IEC B and Kaimal spectrum criteria
2. Aerodynamic forces calculated using blade element theory
3. Turbine equipped with Bladed-style DLL control, blades may pitch and feather during simulations
4. Stochastically generated irregular waves from the JONSWAP spectrum, user-defined wave height, peak period, propagation direction and wave spreading
5. Vertical stretching of wave forces.
6. Hydrodynamic forces calculated using Morison, and diffraction theory applied when Morison criteria are not met
7. User defined marine growth mass, density and thickness is included in all calculations
8. Four structural modes are retained, the 1st and 2nd in both the fore-aft and side-side directions.
9. Structural damping is incorporating by designating the damping ratios of the 1st and 2nd modes in the fore-aft (FA) and side-side (SS) directions. Initially all four ratios were set to 1% of critical.
10. Soil stiffness represented using the previously derived soil spring stiffness values.

Renderings of the Hybrid monopile model, with the modelled reference 8 MW turbine are shown in Figure 5-1.

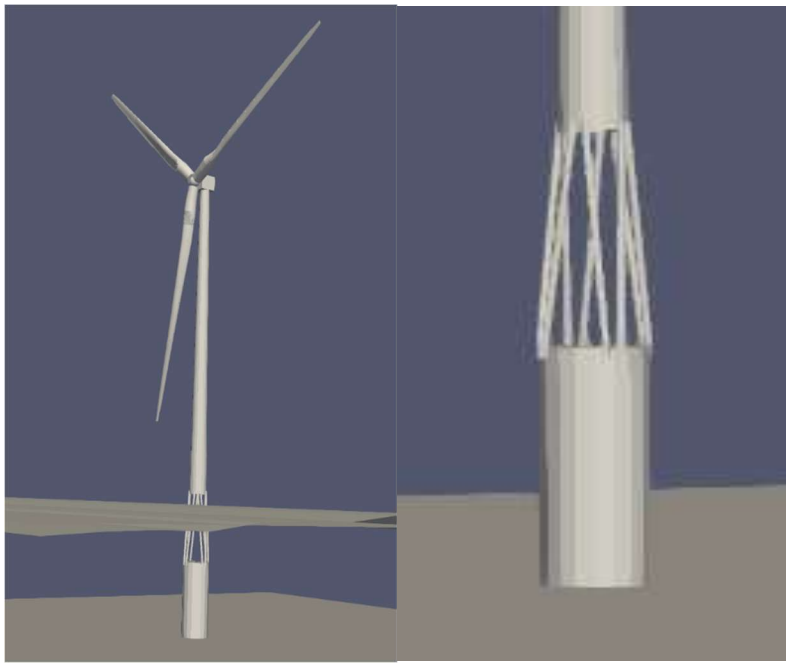

Figure 5-1: FAST model renderings of Hybrid Monopile model with 8 MW turbine

5.2. Validation of Matlab modelling

A modal analysis was performed on the model and compared to the previously calculated natural frequencies of the Matlab-based equivalent beam model.

Table 10: Modal analysis results comparison - FAST model

Frequency	Euler-Bernoulli	Timoshenko	FAST
1st (fore-aft)	.205	.202	.203
1st (side-side)	[-]	[-]	.206
2nd (fore-aft)	.789	.735	.728
2nd (side-side)	[-]	[-]	.733

From the results of the modal analysis shown in Table 10, it can be said that the Matlab-based equivalent beam model, derived from the finite difference method, provides an accurate approximation of the structure frequencies. Additionally, the results of the FAST modal analysis confirm that the mode shapes are not significantly influenced by the eccentricity of the rotor mass with respect to the structure centerline. The assumption of axial symmetry, with respect to mode shapes, is valid.

The next step was to validate the estimation of hydrodynamic loads on the structure, particularly as the sheltering factors discussed in Chapter 4 were computed using some degree of visual estimation and hand calculations. It was anticipated that the FAST simulations would show the Matlab-based wave forces to be overestimated.

Wave loads in the Matlab model are simplified to assume that the wave propagation direction is constant and that the loads are incident at the same angle at all points on the support structure. This will inherently lead to slightly conservative results.

Figure 5-2 shows the resulting mudline moment in MNm during a 1200 second simulation of loading from a fully aligned 17.0-meter ULS wave.

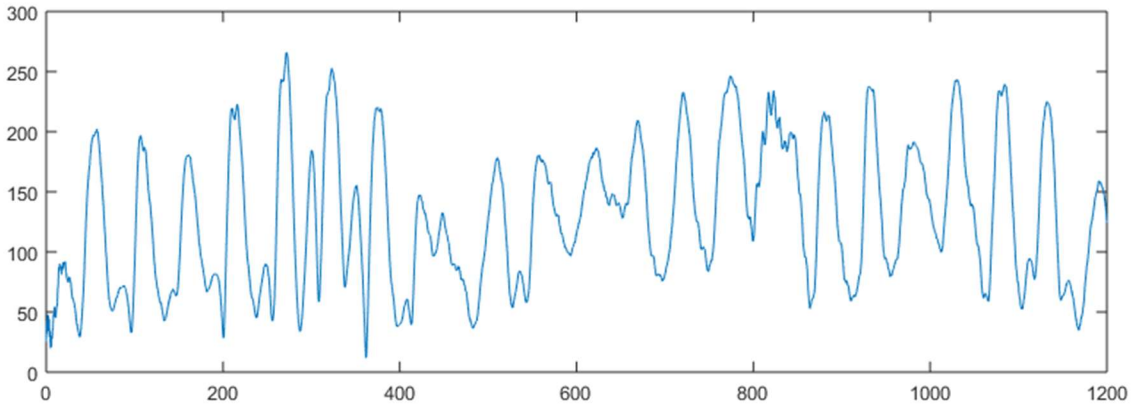

Figure 5-2: FAST simulation, aligned ULS wave only

The maximum wave-induced mudline moment during the simulation is 268 MNm, approximately 8% less than the 285 MNm predicted in the Matlab model. This discrepancy between the two models was shown to range between 6.2 and 10.1 % over twenty test cases, confirming that the simplified estimates are on the conservative side. Wave loads in the Matlab model were subsequently calibrated with a scaling factor of .94 based on the results.

5.3. Distribution of loading across members

The remaining simulations were used to provide general insight into the dynamic response of the brace members, and to assess the accuracy of the previously established method for estimating the percentage of the total applied load shared by brace, dependent upon the load application angle and the resulting neutral bending axis.

A total of thirty-six different load combinations were run, covering sea states with wind speeds below cut-in, above cut-out, and in the rated speed range, as well as wind-wave misalignment angles of 0, 30, 45, 60, 90, and 120 degrees. For each simulation, the average normalized proportion of the total load carried by each brace over the 600 second time series was calculated and compared to the Matlab estimate based on the distance from the bending axis. Though the portion of the load carried by each brace varies dynamically as the turbine moves, the time-averaged values deviated from the static Matlab estimations by an average of only 2-5% over the eight braces. Normalized brace reaction forces in the fore-aft and side-side directions for one of these simulations are plotted in Figures 5-2 and 5-3.

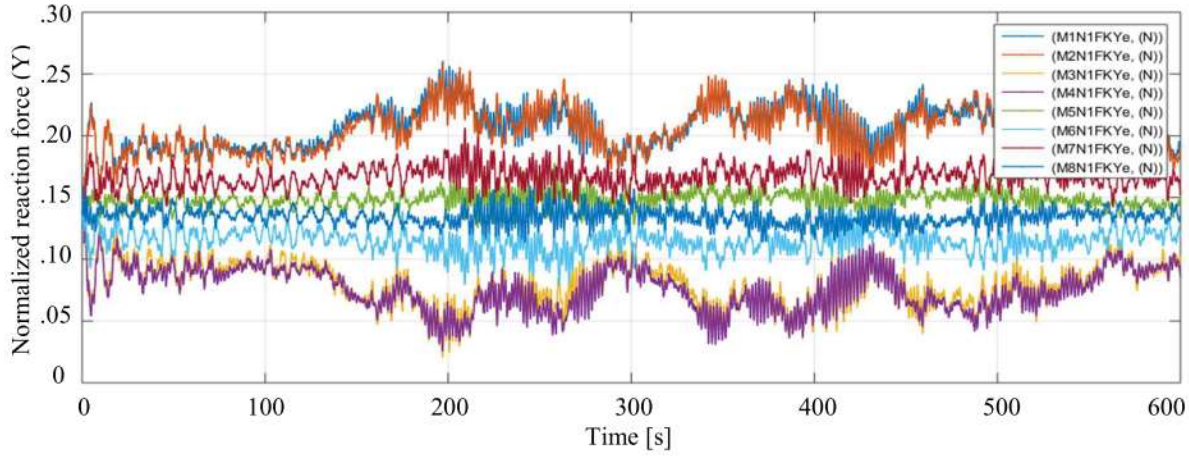

Figure 5-3: Resultant force in Y-direction per brace for 45-degree misaligned sea state, 3.0-meter wave

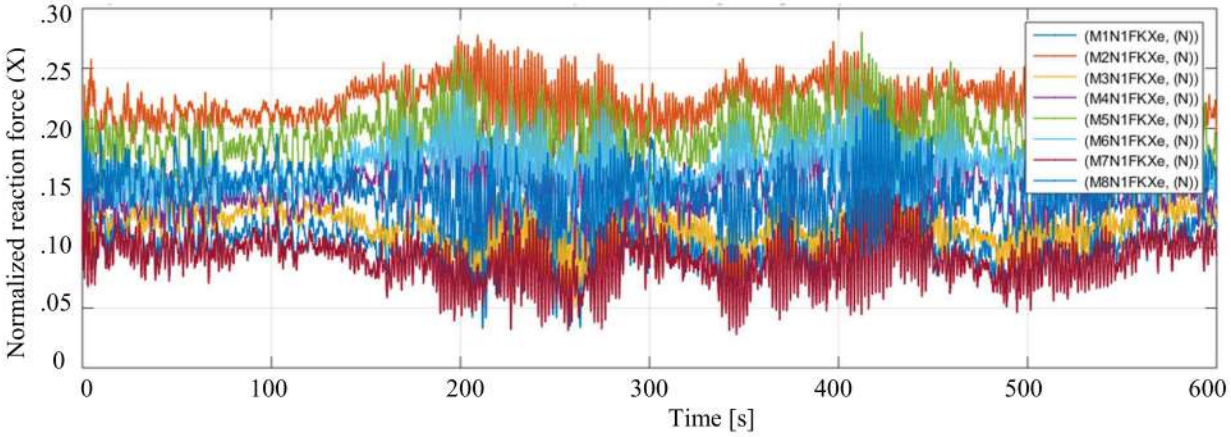

Figure 5-4: Resultant force in X-direction per brace for 45-degree misaligned sea state, 3.0-meter wave

Examining the dynamic component of the reaction force in the fore-aft direction shown in Figure 5-3 and recalling the top view of the 4x2 Hybrid Monopile configuration shown in Figure 4-2, it is apparent that the member pair at the back of the ring carries a sizeable portion of the load, with some assistance from the member pairs located on either side.

Insight from these simulations prompted a change in the orientation of the brace members around the shell perimeter, rotating the entire arrangement by 45 degrees such that four brace members are arranged along the fore and aft sides of the shell, to more evening distribute the applied loads. This updated arrangement is depicted in Figure 5-5, along with the brace numbering convention used for the remainder of the report.

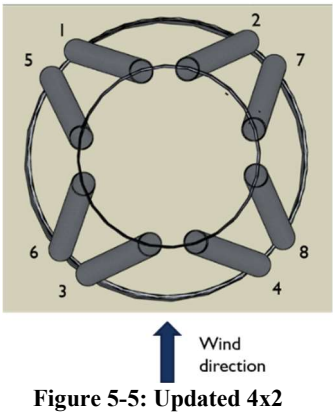

Figure 5-5: Updated 4x2 member arrangement

6. Fatigue assessment of Hybrid Monopile support structure

6.1. Method summary

To compute the expected fatigue life at critical locations in the support structure, the structure responses to wind and wave loads are decoupled, and the wave-induced fatigue damage is handled entirely in the frequency domain. Wind-induced fatigue is handled in the time-domain. Lifetime wind loading is approximated by applying a rainflow counting algorithm to a time history of thrust loads and extrapolating the signal for the full structure life. The corresponding wave load response for each sea state is represented by a frequency-dependent structure response spectrum. In both cases, the lifetime response for each sea state may be expressed as a damage equivalent load (DELs), and the DELs from wind and waves are combined using the principle of quadratic superposition. This method for combining the frequency and time domain fatigue computations is outlined in the flow chart shown in Figure 6-1 below.

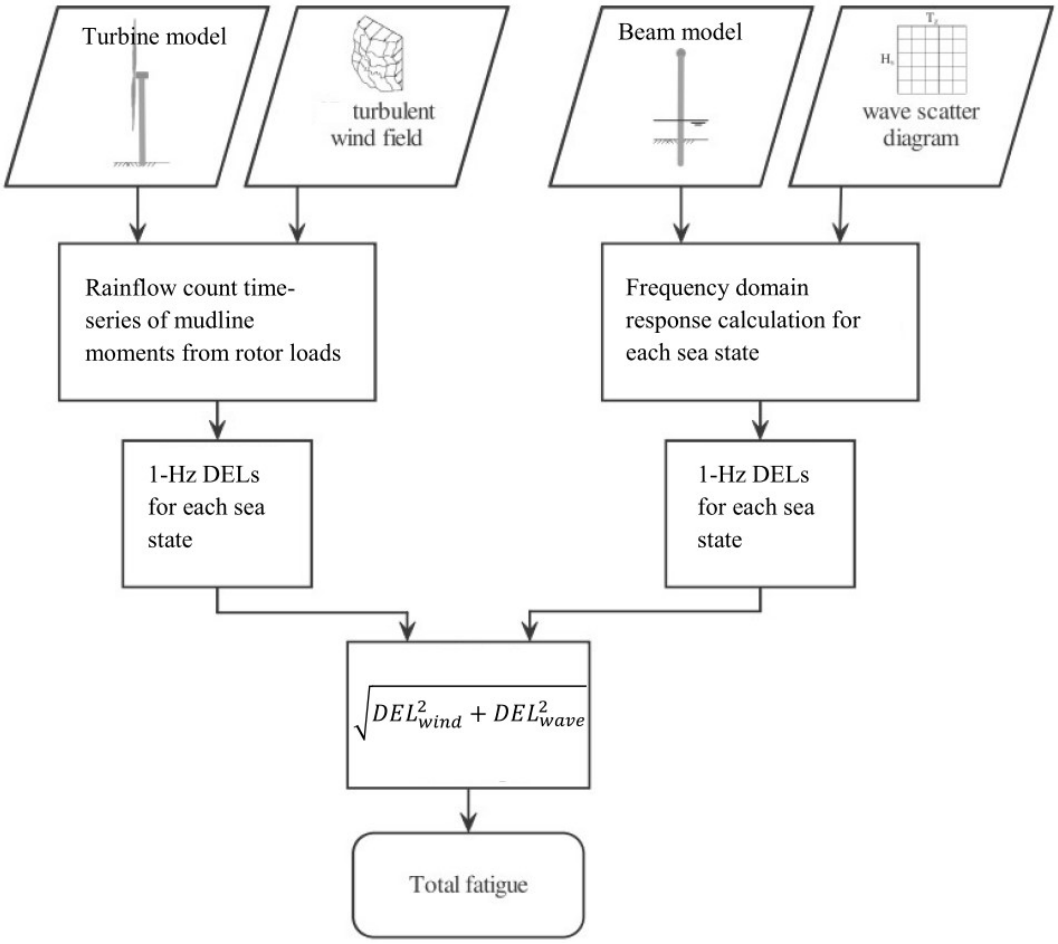

Figure 6-1: Flow chart of proposed fatigue assessment methodology I - adapted from [22]

Bending moments applied at the mudline result in stresses in the monopile shell which will vary around the circumference. A certain point on the circumference will undergo the maximum stress and will become the governing location for the fatigue assessment. The stress at any point in the cross section produced by the wave-induced bending moment is as follows.

$$\sigma = \frac{M_y}{I_y} * x + \frac{M_x}{I_x} * y = \frac{M_y}{I_y} * rcos(\Theta) + \frac{M_x}{I_x} * rsin(\Theta)$$

Where Θ is the axis between the point of interest on the circle and the axis of the applied load, and r is the radius of the shell as shown in the figure below.

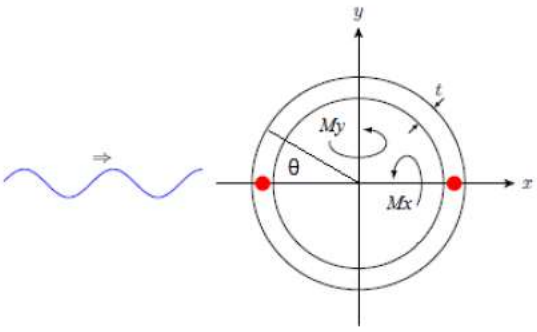

Figure 6-2: Maximum fatigue locations for fully aligned load [51]

The red spots indicate the locations with the maximum distance from the neutral bending axis and therefore the locations that will experience the greatest fatigue damage from the aligned load. Since the support structure in this assessment has been assumed to be axisymmetric, for this mudline fatigue assessment.

$$I_x = I_y = I_{mudline}$$

Furthermore, this simplified assessment assumes that the wind and waves are always align and approach along the x-axis leading to,

$$M_x = 0$$

and reducing the equation to,

$$\sigma = \frac{M_y * D_{mudline}}{2I_{mudline}}$$

At locations considered critical or governing for fatigue life assessment, there is usually an additional stress that arises from a rapid change in physical properties or environmental loads over a short physical distance. Examples include welded joints between members, or the point where a monopile shell transitions from being embedded in soil to above the mudline. These critical junctions are known as “Hot Spots” and the additional stress at those points is accounted for by computing the hot spot stress range, or HSSR.

The HSSR is found by multiplying the stress from the damage equivalent bending moment by a stress concentration factor, *SCF*, and an equivalent thickness factor *TE*. Stress concentration factors are prescribed in the design standards based on the type of cross section, and the location of the section with respect to the waterline. A value of 1.5 is assigned for the mudline assessment. The equivalent thickness factor accounts for unseen internal deformations and imperfections that occur in thicker shells during fabrication. Calculated by

$$TE = \left(\frac{t}{t_{ref}}\right)^{k}$$

Where t_{ref} refers to a reference shell thickness of 25 millimetres and k is a dimensionless constant [11]. From this Hot Spot Stress Range, the number of cycles that can be endured at that level before fatigue failure occurs, *N,* is determined using material specific S-N curves. For this report, the S-N curve C1 for steel in seawater with cathodic protection, available from DNV standard DNV-OS-J101 [11], is used.

$$\log_{10}(N) = \log_{10}(a) - m * \log_{10}(HSSR$$

Values for $\log_{10}(a)$, and *m* correspond to parameters characteristic to the selected SN curve for the material. Additionally, *m* and $\log_{10}(a)$ each have two different values, 3.0/5.0 and 12.0/16.1, corresponding to whether the number of allowable cycles *N* at a given stress range is less than or greater than the knee-point in the SN curve referred to in Section 4.1 where slop changes from 3 to 5, occurring at 10^6 cycles.

Once the allowable cycles are computed, Palmer-Miner's rule is applied to find the damage accumulation at each sea state [11]. Damage is found by a summation of the ratio of the number of occurrences of each stress range compare to the allowable number of cycles at that stress before failure, extracted from the appropriate S-N curve.

$$Damage = \sum_{i=1}^{k} n_i/N_i$$

Since the HSSRs were computed using 1-Hz DELs, instead of multiplying by the number of cycles prescribed in the sea state data, the associated damage is multiplied by the product of the total seconds in the structure lifetime, and the probability of occurrence of that sea state. Fatigue failure will occur when D exceeds 1.

Due to the high level of uncertainty in fatigue calculations, DNV prescribes an additional safety factor known as the design fatigue factor by which to multiple the calculated damage. The factor varies from 1.0 to 3.0 depending on the location of the point of interest with respect to the waterline or seabed. At the mudline, the *DFF* is taken to be 3.0 such that the estimated fatigue life in years is calculated by:

$$FatigueLi \qquad \frac{Life_{operational}}{3.0 * Dama_{\ total}}$$

6.2. Key assumptions

6.3. Governing shell location

For the purposes of this analysis, even in cases where the wind and wave loads are misaligned, the critical fatigue locations identified in the previous section are still considered the governing locations for the assessment. As the misalignment angle between the applied wind and wave loads increases, the orientation of the neutral bending axis with respect to the X-Z plane will shift accordingly, also shifting the point at which the highest bending stresses occur. However, the bending moment at the mudline due to wind loading will always exceed that produced by wave loads, due to the substantial moment arm, except in the case of extreme wave loading at wind speeds above cut-out. Extreme events like this are rare, and therefore will not contribute substantially to fatigue damage accumulation, so even though the critical location for a specific load case may move around the monopile circumference, the points on the shell intersecting the fore-aft axis will incur the greatest cumulative fatigue damage.

Additionally, since the maximum shear forces and bending moments in the structure resulting from wind loading occur when the wind strikes the rotor in the primary direction, all load cases for this report take the incoming wind to be aligned with the rotor, further reducing the number of required simulations. Incorporating wind misalignment and the possible effects is considered an area for potential future research.

6.4. Accounting for aerodynamic damping

Third it assumed that the total system damping, will vary linearly with the angle Θ in degrees about a quadrant of the structure due to varying influence of aerodynamic damping in each direction. As discussed in Chapter 3, aerodynamic damping is set at the recommended engineering estimate value, 4% of critical damping. The total system damping ratio is considered to vary linearly with the angle Θ between the maximum value of 6.0 % in the fore-aft direction and 2.0 % in the side-side orientation according to:

$$Damping\ \%\ (\Theta) = 6.0\% - \frac{6.0\% - 2.0\%}{90\ degrees}$$

Since the damages occurring from wind and wave loads are to be treated separately, it is important to independently address the effect of aerodynamic damping on the structure response to wave loads. In determining the response to wave loading in each alignment bin, the aerodynamic damping in that excitation direction is incorporated into the total structure damping.

For sea states with characteristic wind speeds above or below the cut-out/cut-in speeds, the turbine is considered parked/idling and the damping ratio is assumed to be the minimum value of 2.0 percent. Aside time intervals during sea states with characteristic wind speeds outside the operational range, turbines experience other instances of being parked or idling, due to malfunctions. Due to the reduced damping, these intervals can contribute considerably to the overall fatigue calculation. Industry standard practice is to assume that a turbine will spend at least 10% of its life in a non-operational state and that assumption is also used in this analysis.

6.5. Computing wave-induced fatigue damage in the frequency domain

As discussed in Chapter 3, wave-induced loads on offshore structures are the result of the individual wave particle kinematics, which are a function of the wave amplitude, frequency, and phase. The phase angle, varying between 0 and 2π radians, represents the location along the circles or elliptical orbit of the particle at an instant in time. This means that the force exerted on a structure by a wave of a certain size, does not have a single value, but a range of values as a function of the wave phase angle. Figure 6-3 plots the base shear and overturning moment loads on reference monopile as a function of wave phase.

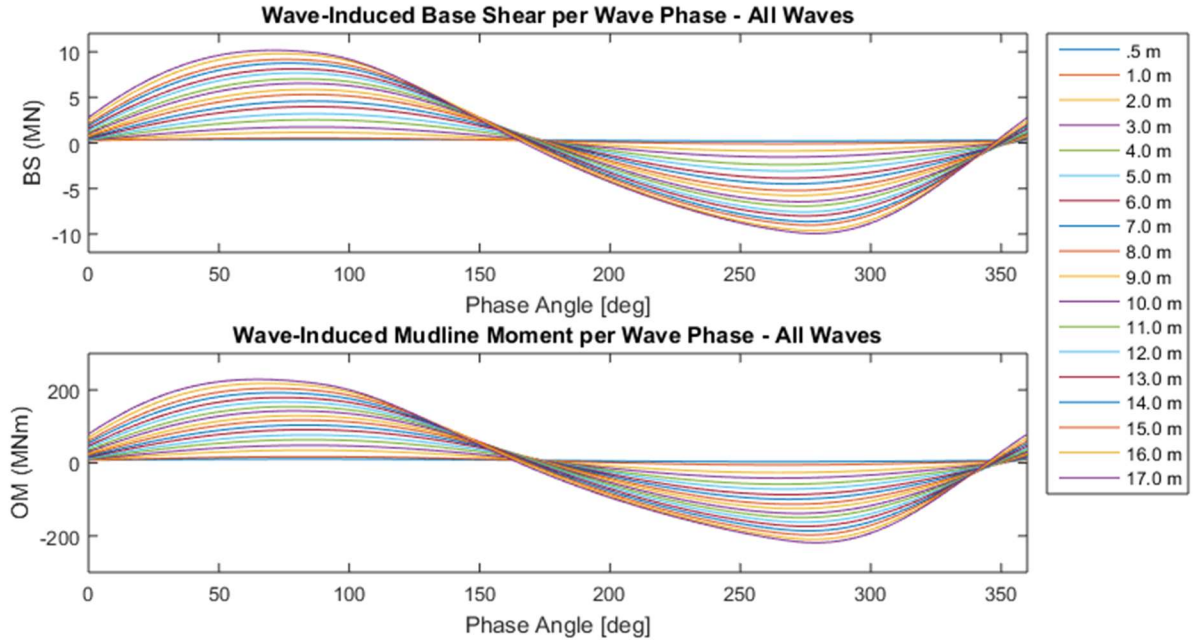

Figure 6-3: Wave induced base shear and mudline moment with respect to wave phase for each sea state

Since phase is a stochastically distributed random variable, and as previously discussed, response calculations performed in the frequency domain efficiently compute the potential response to all possible stochastic scenarios in a frequency range and the fluctuation in loading over the entire structure life is captured. This fluctuation is reduced to a single damage equivalent load, or DEL for each sea state. These DELs are determined using the established equivalent beam model and wave spectra to compute a transfer function and response spectrum for each sea state using a modified from of the method outlined by Seidel [8] to allow for the inclusion of aerodynamic damping and misaligned wave loads.

6.6. Simplified frequency domain approach

The method can be summarized in six steps.

1. The natural frequencies ω_n and mode shapes $\phi_n(z)$ are established using the mass and stiffness matrices of the equation of motion, as derived in earlier chapters. Per previous discussions, only the first mode is considered. Modal mass and stiffness are then determined for each mode using the eigenvalue matrix by:

$$Eig^T * \boldsymbol{M} * Eig = \quad \boldsymbol{modal}$$

$$\boldsymbol{K_{modal}} = \omega_n^2 * \boldsymbol{M_{modal}}$$

2. A damping ratio is selected as discussed in Section 6.2.2.

3. For each relevant sea state, the JONSWAP wave spectrum $S_{\zeta\zeta}(\omega)$ is calculated as previously described in Chapter 3.

4. Two transfer functions are computed, a hydrodynamic transfer function to translate the incoming wave to a force on the structure, and a mechanical transfer function to translate the excitation on the structure to a dynamic response.

The hydrodynamic transfer function $H_{a,n}(\omega)$, closely resembles the Morison equation.

$$H_{a,n}(\omega) = \frac{1}{2} * \rho * \omega_o * \int_0^d C_D * D(z) * \eta_o(z) * \Phi_o(z) * dz +$$

$$\rho * \omega_o^2 * \int_0^d C_{M(z)} * \left[\pi * \frac{D(z)^2}{4}\right] * \eta_o(z) * \Phi_o(z) * dz \; = constant$$

with $\eta_o(z)$ representing the decay in water particle acceleration with respect to depth.

$$\eta(z, \omega_0) = \eta_0(z) = \frac{\cosh(k_0 \cdot (z+d))}{\sinh(k_0 \cdot d)}$$

For large monopiles the drag term may be omitted, but as previously mentioned, the inclusion of the thinner Hybrid brace members warrants keeping the drag term included.

The mechanical transfer function $H_{n(\omega)}$ computes the degree to which the applied loads may be amplified, as a function of the wave forcing frequency ω, due to the structure modal stiffness K_n and its natural frequency ω_n.

$$H_{n(\omega)} = \frac{1}{1 - \left(\frac{\omega}{\omega_n}\right)^2 + 2 * i * \zeta_n * \frac{\omega}{\omega_n}} * K_n^{-1}$$

As is apparent in the formulation, $H_{n(\omega)}$ is maximized when the wave forcing frequency is either equal to or very close to that of the structure modal frequency. This will result in a narrow-banded response spectrum, concentrated at the frequency where this amplification occurs.

A combined transfer function for any location of interest along the length of the structure can be calculated by multiplying the product of the transfer function and the modal displacement $\Phi_o(z)$ such that:

$$H_{a,n}(z,\omega) = \sum \Phi_o(z) * H_{a,n}(\omega) * H_n(\omega)$$

5. The response spectrum, for an elevation z, is then determined by multiplying the wave spectrum by the combined transfer function, as described in Chapter 3:

$$S_{response}(\omega) = \left|\sum \Phi_o(z) * H_{a,n}(\omega) * H_n(\omega)\right|^2 * S_{JW}(\omega)$$

6. This response spectrum can then be used to compute either extreme or fatigue loads at the designated elevation, typically mudline or MSL. Figure 4-14 shows the normalized wave amplitude and corresponding response spectra for a sea state with a significant wave height of 3.0 meters and a peak period of 6.9 seconds, and only include 1% structural damping.

As anticipated, the response spectrum is narrow-banded, containing all energy at or adjacent to the first natural frequency of the structure.

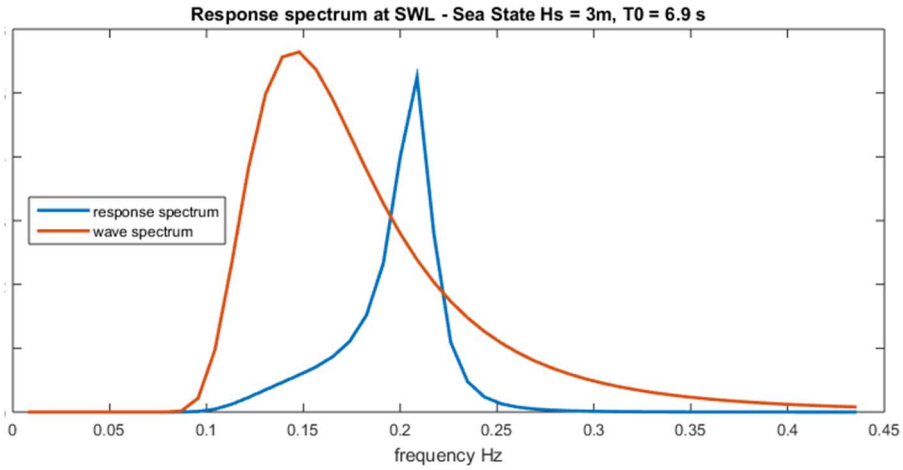

Figure 6-4: Wave excitation and structure response spectra for a typical fatigue sea state

For the narrow-banded spectrum, the value of the response spectrum at the peak can be used to calculate the standard deviation of the bending response at the tower base. Assuming a Rayleigh probability distribution for the mudline bending moment, the equivalent bending moment range is taken as:

$$\Delta M_{bending} = 3.363 * \sigma_{bending}$$

This bending moment range, or damage equivalent load, is what is known as a 1-Hz DEL is then translated to fatigue damage using the steps outlined in Section 6.1. It should be noted that using the Rayleigh distribution neglects any negative moment values, and may result in a conservative calculation. These loads are therefore not tied to a specific structure lifetime, but to a 1-second interval, and may be easily scaled to any time interval of interest. Using this procedure, response spectra and the associated damage equivalent load ranges are determined for each sea state and six different wave approach angles.

6.7. Response to misaligned waves

Met-mast and wave buoy data for a North Sea location near the hypothetical Hybrid Monopile test site was processed to plot the probability distributions of wind and wave approach direction, for the first five sea states, over a 20-year period. These probability distributions were plotted with respect to direction to form what are known as wind and wave roses, shown in Figure 6-5.

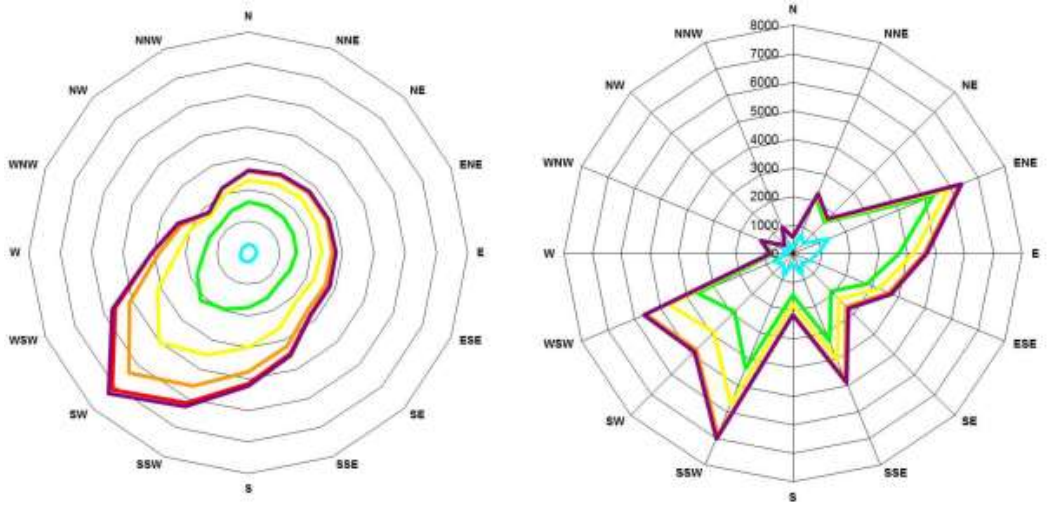

Figure 6-5: Wind and wave alignment roses for reference site- sea states 1-5

From the rose diagrams, it is apparent that wind direction is very consistent, justifying the previously stated assumption that wind loads always approach at 0-degree misalignment. Incoming waves show a wider distribution, spreading somewhat evenly, and independent of wave height, over a 150-degree section of the rose. The wave misalignment for this site can be captured in six 30-degree bins. For the fatigue assessment, the following occurrence probabilities and damping ratios are assigned to each wave approach direction.

Table 11: Total damping ratio associated with wave misalignment bins

	0 degrees	30 degrees	60 degrees	90 degrees	120 degrees	150 degrees
$P(bin)$	.21	.19	.17	.13	.12	.17
ζ_{total}	6.0%	4.7%	3.3%	2.0%	3.3%	4.7%

The effects of the variable wind-wave misalignment and damping ratio on the response spectrum can be seen in Figures 6-6 through 6-8, which depict the normalized response spectra for wave approaches of 0, 30, and 90-degrees respectively.

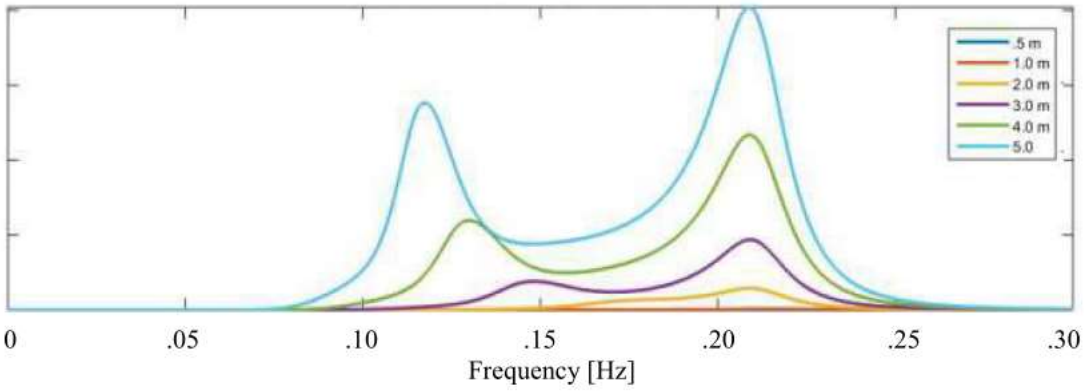

Figure 6-6: Normalized mudline bending response spectrum with total damping of 6%

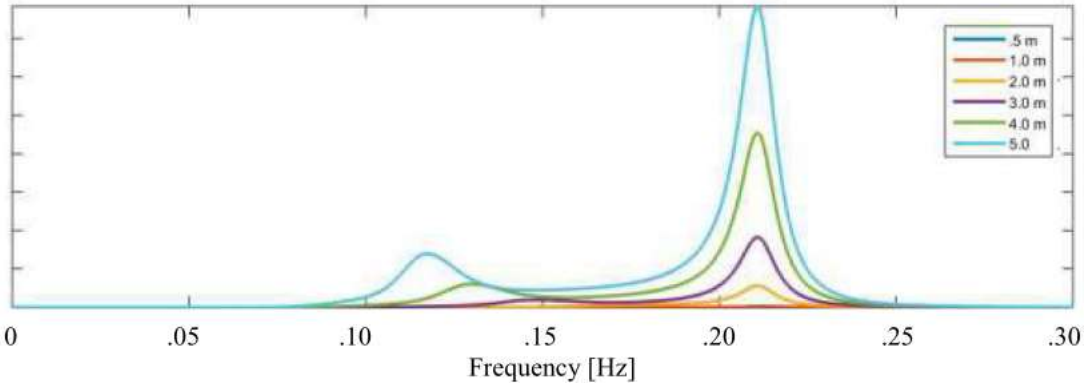

Figure 6-7: Normalized mudline bending response with total damping of 4.67%

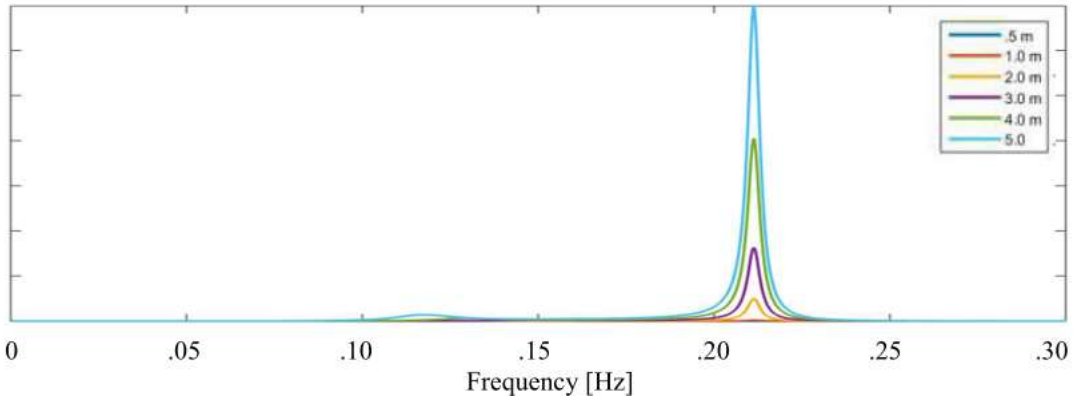

Figure 6-8: Normalized mudline bending response with total damping of 2%

In the side-side direction the response spectrum exhibits a single-peak narrow banded response due to relatively low system damping, but the higher damping ratio in the fore-aft direction causes the response

spectrum to be less narrow banded and results in multiple peaks, as explained by Van der Tempel [14] and Seidel [8]. The secondary peaks visible in the high damping response spectra occur at the frequency of the forcing wave. To determine the damage equivalent bending load for each sea state over then entire life of the structure, the DEL is calculated for each misalignment response spectrum and combined as a weighted average based on the occurrence probability of each directionality bin.

6.8. Computing response to wind loads

Wind-induced fatigue damage is handled in the time domain due to the non-linearity of the thrust loads on the rotor with respect to wind speed. This non-linearity is illustrated in Figures 6-9 and 6-10. Figure 6-9 shows a time series of turbulent wind speeds, produced from the Kaimal spectrum for a mean wind speed of 12 meters per second, and the corresponding thrust force on the rotor calculated using the BEM method discussed in Chapter 3. As is apparent in the thrust load time history, a plateau appears in portions of the load history corresponding to wind speeds that are consistently above the 12 m/s rated wind speed of the 8 MW turbine. At these speeds, the turbine operations at its optimum efficiency, and the thrust on the rotor is at is maximum.

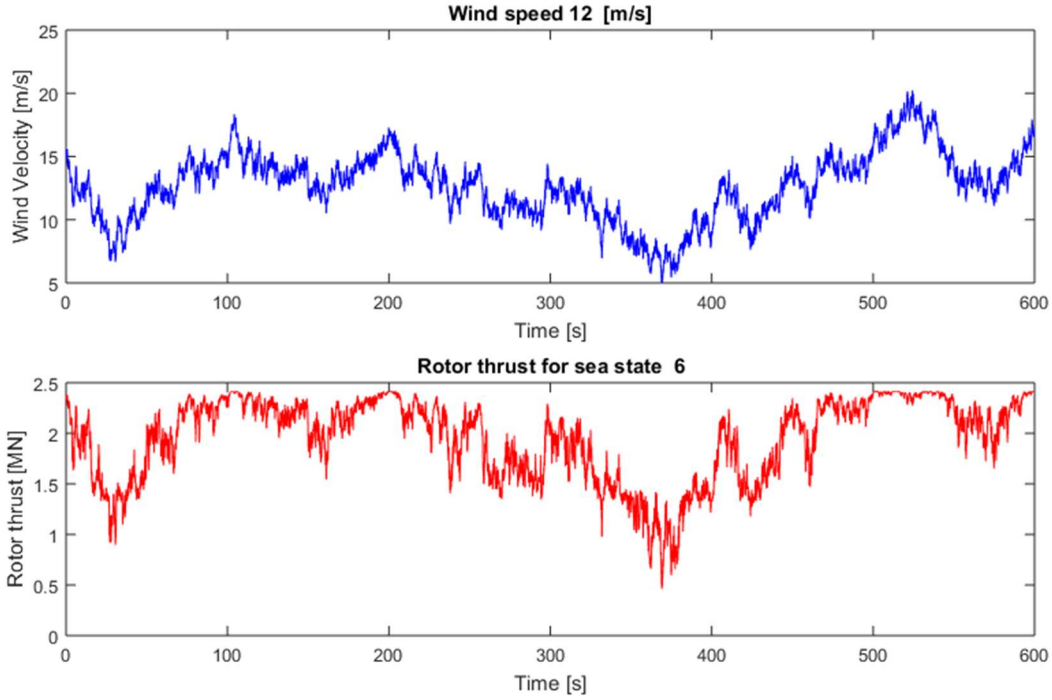

Figure 6-9: Time series of wind speeds and tower top loads for an 8 MW turbine produced from turbulent Kaimal spectrum (at rated wind speed)

When the rotor is operating in its rated condition, an increase in wind speed no longer corresponds to the increase in the thrust loads on the rotor. This non-linearity works in the opposite direction as well. At speeds above the cut-out wind speed, the turbine will enter an idling condition and an increase in wind speed then results in a *decrease* in the thrust at the rotor. This phenomenon is shown in Figure 6-10.

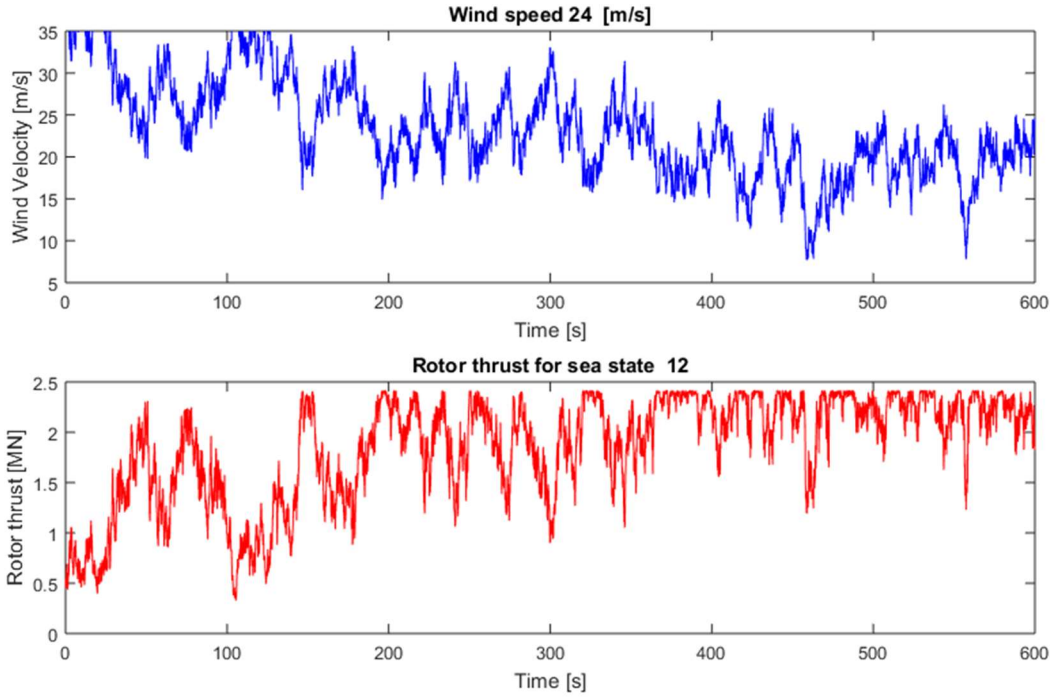

Figure 6-10: Time series of wind speeds and tower top loads for an 8 MW turbine produced from turbulent Kaimal spectrum (above cut-out wind speed)

Handling the wind-induced fatigue damage in the time domain means that the lifetime structure response cannot be captured by a single response computation, but must be extrapolated from several randomized sample simulations. Due to time and computation constraints inherent to this project, it was not feasibly to perform the thousands of simulations that are technically recommended for assessing an offshore turbine. Since the primary goal of the support structure is to minimize fatigue damage incurred due to waves, and not wind, the process is streamlined, using six 600 second simulations, with six different randomized turbulence seeds, to compose a 3600 second time history of thrust loads for each of the 17 sea states, all considered to approach from the same direction.

6.9. HSSRs and Rainflow counting

To simply translate this time history of thrust loads on the rotor, to a time series of moments at the mudline, it is assumed that the structure is considered to be completely rigid. Using the rigid structure assumption thrusts are converted to moments by multiplying them by the distance between the hub and seabed. These mudline moments are then converted to the Hot Spot Stresses using the same stress concentration and equivalent thickness factors presented in Section 6.1. A sample HSSR series for sea state 3, wind speed 8 m/s, is shown below in Figures 6-11.

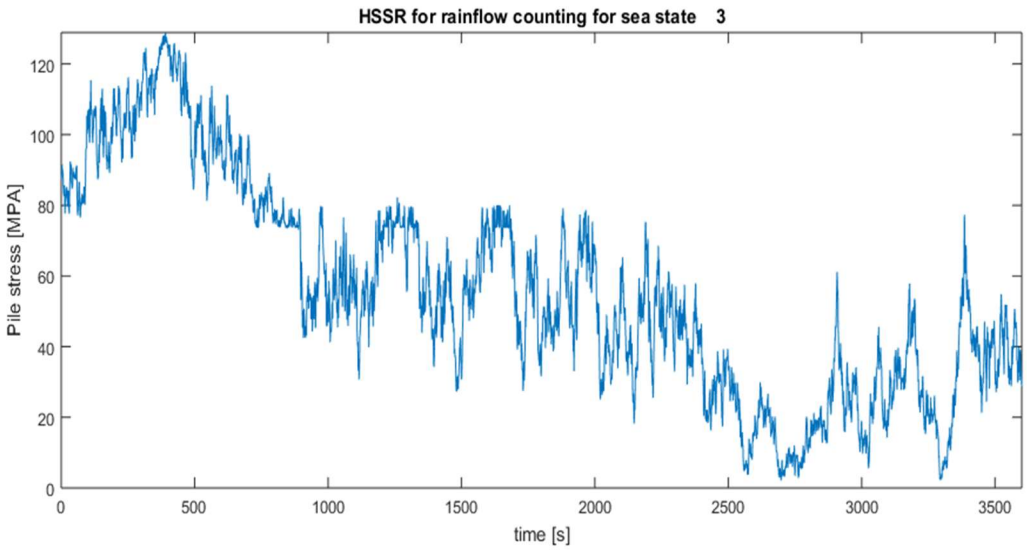

Figure 6-11: Hot spot stress range for combined wind and wave loading, sea state 3

The stress signal is then fed through a rainflow counting algorithm that identifies the turning point in the time-series and creates a histogram of the corresponding stress amplitude between each pair of turning points. Bin frequency for each stress range in the histogram is known as the cycle rate. Figure 6-12 shows the resulting rainflow histogram from the signal in 6-8. The y-axis of the rainflow plot depicts the stress amplitude at the mudline cross section in MPa and the x-axis counts the number of time steps between turning points. Since wind loads fluctuate at a very high frequency, the histogram is heavily skewed towards the minimum x-value.

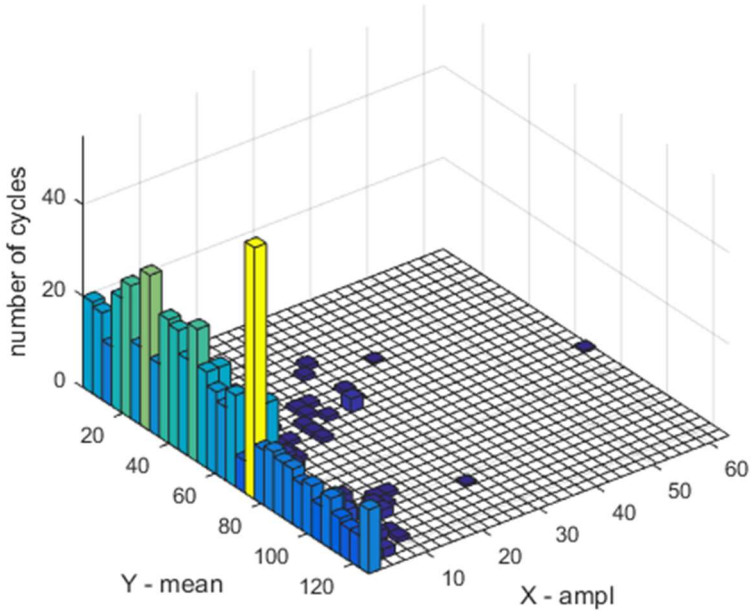

Figure 6-12: Rainflow count histogram of stress time series, sea state 3

These stress ranges can then be directly translated into accumulated damage. Damage for each stress amplitude in the time signal is calculated by:

$$damage(\sigma) = \left(\frac{CycleRate}{N_k}\right) * \left(\frac{\sigma}{\sigma_{yield}}\right)^m$$

with

σ	Hot Spot Stress	[MPa]
$CycleRate$	Number of cycles in bin	[-]
N_k	Knee-point of SN curve	[-]
σ_{yield}	Yield stress of steel	[MPa]
m	Slope of SN curve	[-]

This damage is summed for every histogram bin and then multiplied by the number of anticipated cycles for that sea state in the structure life:

$$\frac{StructureLife\ (27\ years)}{SignalLengt\quad(600\ seconds)} * N_{cycles}(Sea\ State)$$

This procedure is repeated for each sea state to determine the damage accumulation from the wind loading. However, to efficiently combine this damage with that caused by the wave loads, it is beneficial to reverse the damage calculation to a 1-Hz DEL equivalent by reversing the last five computations in section 6.1.

6.10. Combining wind and wave loads

Once the 1-Hz DELs for the decoupled wind and wave loads are obtained, they can be combined through quadratic superposition such that,

$$DEL_{total} = \sqrt{DEL_{wind}^2 + DEL_{wave}^2}$$

Owing to the rigid structure assumption used to compute the wind loads, the wind DELs for the reference monopile and the Hybrid Monopile are identical. Table 13 gives these damage equivalent loads from wind, the wave-induced damage equivalent loads for the reference structure and the Hybrid alternative, as well as the combined DELs resulting from the quadratic superposition and the resulting fatigue life.

Table 12: Mudline DELs under combined wind and wave loading [MNm]

Sea State	$DELs_{wind}$	$DELs_{wave}$ (Reference)	$DELs_{wave}$ (Hybrid)	$DELs_{total}$ (Reference)	$DELs_{total}$ (Hybrid)
1	3.7	0.1	0.0	3.7	3.7
2	4.0	5.2	1.7	6.1	4.3
3	9.6	32.7	13.1	33.6	16.3
4	38.5	46.4	20.4	60.2	43.5
5	52.6	68.7	32.0	86.5	61.6
6	52.8	87.9	42.4	102.6	67.7
7	62.8	108.1	53.2	125.0	82.3
8	47.8	125.8	62.7	134.6	78.8
9	53.6	143.8	72.4	153.5	90.1
10	61.2	158.7	80.3	170.1	101.0
11	68.1	173.5	88.3	186.4	111.5
12	70.5	186.7	95.0	199.6	118.3
13	86.2	200.7	102.6	218.5	134.0
14	91.3	212.4	108.4	231.2	141.7
15	100.2	224.7	115.0	246.0	152.5
16	104.2	236.1	124.2	258.0	162.1
17	101.9	247.8	130.5	267.9	165.6
18 (ULS)	85.0	261.6	141.4	275.1	165.0
Resulting Fatigue Life (years)	**(R) 348 years** **(H) 140 years**	**86 years**	**349 years**	**55 years**	**92 years**

It should be noted that though the wind DELs in this case are identical, the resulting fatigue life in the reference and Hybrid cases differs due to the difference in shell thickness in the analysis. As discussed in the basis of design the reference case monopile has a shell thickness of 84 mm and the Hybrid Monopile shell has a thickness of 55 millimetres. From the table, it is apparent that even with more than a thirty percent reduction in shell thickness, the expected fatigue life of the Hybrid Monopile is nearly double that of the base case. If the Hybrid structure were to have the same thickness as the reference case, the expected fatigue life increases to 174 years. Additionally, the Hybrid Monopile is clearly an effective measure to reduce wave-induced fatigue damage, increasing the expected fatigue life under wave loading by 400% compared to the reference case. Based on this result, pile fatigue at the mudline is no longer the governing load case for the structure, and therefore the focus of the analysis is shifted to the behaviour of the individual members.

6.11. Individual brace fatigue

The section focuses on evaluating the fatigue life of the individual members. In practice, the most critical location at which to assess the brace fatigue would be at the welded connection. However, the specifics of the connection weld detailed at being handed as part of another ongoing research effort. Since the connection detail itself is outside the scope of this project, the location of interest for the fatigue assessment was selected as the brace cross section just above the weld location. This location is selection for the purposes of verifying the selected dimensions of the brace cross section are sufficient to resist fatigue failure from cyclic bending. During the brace fatigue assessment, for each load case, applied loads are distributed across the 8 members using the method developed in Chapter 4, and affirmed in Chapter 5.

6.12. Wave spectrum modifications

The previously calculated wave response spectra are easily modified to shift the focus to this new location. This modification is performed by truncating the mode shape vector, mechanical transfer function, and hydrodynamic transfer function, to the mid-brace elevation, and maintaining the previously established aerodynamic damping convention. Wave fatigue contributions to fatigue at the brace elevation are very small compared to those from wind, since at the elevation of interest along the brace members, the moment arm for the applied wind load is 20-50 times longer than that of the wave load.

6.13. Response to wind – brace members

To re-evaluate the fatigue damage from wind loading at the location of interest, the time series of bending moments from rotor loads previously calculated are easily translated to a new elevation, and then the procedure for determining the HSSR is repeated using an updated distance to the neutral bending axis for each member, and updating the area moment of inertia for the section.

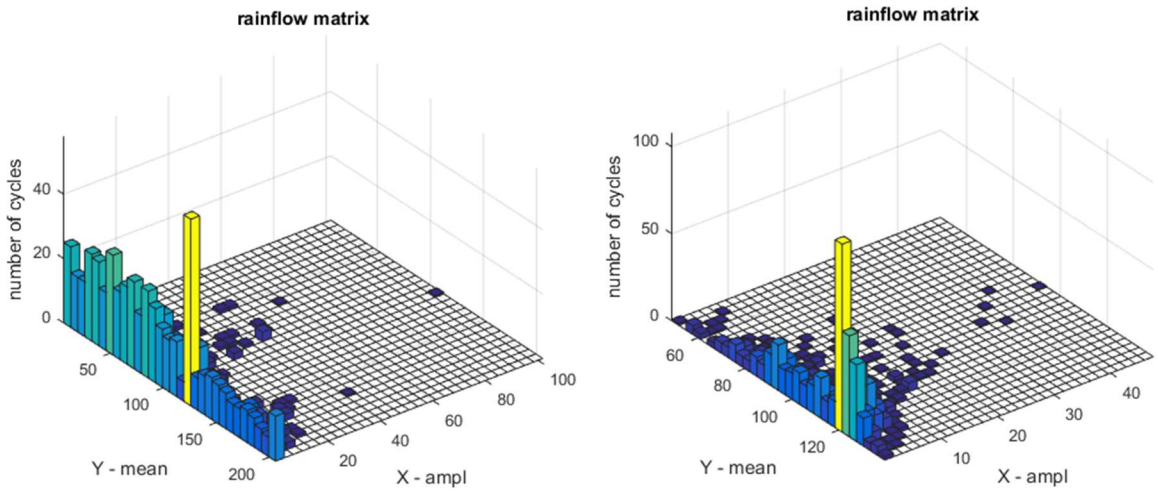

Figure 6-13: Rainflow histograms for two most probable sea states

The rainflow histogram on the left in Figure 6-10 shows the stress in a brace member for the sea state corresponding to a 4 m/s wind speed. Since the wind in this sea state fluctuates about the cut-in speed,

stresses are widely distributed across the range from 0 to 200 MPa. For the next sea state, where the wind speed is slightly higher and the turbine operates consistently, brace stresses are less variable.

6.14. Fatigue under combined loading

These updated stresses can once again be backtracked to DELs and combined using quadratic superposition, just as in the case of the mudline loads. Table 14 shows the resulting expected fatigue life for each brace member.

Table 13: Brace fatigue life under combined wind and wave loading

Brace ID	Fatigue Life (years)
1	16.6
2	16.9
3	16.9
4	16.6
5	40.9
6	42.3
7	42.3
8	40.9

The initial fatigue check shows that based on the initial dimensions, with a member diameter of .85 meters and a thickness of 42 mm, the four members furthest from the primary bending axis, will fail in fatigue. Though it should be noted that this is likely an underestimation of the fatigue life, since the assumption that the peak stress continuously falls at the same point on the brace shell, and the assumption that wind loads are always fully aligned, result in a conservative estimation.

6.15. Design iteration

Continuing with the conservative methodology, member dimensions were subsequently iterated to determine a configuration in which every member will have an expected fatigue life of at least 50 years, the standard threshold for support structure design, without modification to the assessment method. Increasing the member diameter for .95 meters and maintaining the D/t ratio of 20 for a thickness of 48 mm, gives the following fatigue results in which all 8 braces show sufficient fatigue life. It would also be possible to only increase the dimensions of the most vulnerable members to limit steel usage, but for the purposes of this assessment, members will be kept identical.

Table 14: Updated brace fatigue life under combined wind and wave loading

Brace ID	Fatigue Life (years)
1	51.2
2	52.1
3	52.1
4	51.2
5	122.7
6	126.5
7	126.5
8	122.7

Up to this point, it has been assumed that, like the traditional monopile, the Hybrid Monopile design will be fatigue driven. With respect to the brace members, though the dimensions had to be iterated to pass the fatigue check, it is not clear whether the brace design is FLS or ULS driven. Chapter 7 revisits the NORSOK unity check for the brace members, performed in Chapter 4, but with the updated brace dimensions and the incorporated of wind-wave misalignment.

7. Updated ULS assessment - Hybrid Monopile members

Design checks under ULS loads, performed at the mudline in Chapter 4, need not be repeated to account for wind-wave misalignment, since the combined mudline moment resulting from a misaligned wind-wave load will not exceed that of the fully-aligned load used in the original assessment, even when changes in the available wave loading area due to differing degrees of sheltering in different structure orientations, is accounted for.

Based on the fatigue life assessment in Chapter 6, the dimensions of the brace members were increased to have an outer diameter of .95 meters and thickness of 48 mm. Though the dimensions have been increased, they must still be re-assessed under extreme loading, since different load alignment combinations will change what proportion of the total load is born by each member. The NORSOK criterion must be satisfied for each member for each possible wave approach angle. The total wave load from each of the six approach bins assigned in Chapter 6 is recomputed to include variations in the available wave loading area due to member overlap. Using the magnitude of the individual wind and wave loads, and the angle between them, the location of the neutral bending axis can be approximated.

From the locations of brace centerlines in relation to this neutral bending axis, the load sharing factors for each brace in each orientation can be estimated. Table 15 shows the distribution of the factors based on the six-bin analysis. For each of the six load cases, the brace member or members with the largest sharing factor is considered to govern the design and is assessed using the NORSOK unity criteria for combined axial and bending loads.

Table 15: Load sharing factors in brace members for misaligned extreme waves

Brace/Alignment	**0**	**30**	**60**	**90**	**120**	**150**
1	.1426	.1606	.1781	.1932	.1246	.1047
2	.1426	.1246	.1047	.0919	.1606	.1781
3	.1426	.1246	.1047	.0919	.1606	.1781
4	.1426	.1606	.1781	.1932	.1246	.1047
5	.1074	.1313	.1545	.1747	.0836	.0603
6	.1074	.0836	.0603	.0402	.1313	.1545
7	.1074	.0836	.0603	.0402	.1313	.1545
8	.1074	.1313	.1545	.1747	.0836	.0603

Since the magnitude of a structure response to a dynamic load can be significantly larger than that of a static load, the previously calculated static loads are augmented by a dynamic load factor, or DLF.

For the purposes of this assessment, the DLF is related to the ability of the structure to dissipate energy through damping by [36]:

$$DLF = 1 + e^{-\zeta * \pi}$$

With the inclusion of this factor, the third load case from the condensed set of ULS checks presented in Chapter 3, corresponding to a wind velocity near the cut-out speed and a 50-year wave, results in the largest applied loads.

7.1. NORSOK results

Table 16 shows the maximum unity check result for each member resulting from all six iterations of the analysis. Results of the unity check show that the all eight braces successfully pass the ULS check, and that braces 1 and 4 effectively "govern" the design from the ULS perspective. Also apparent is each member has a corresponding mate with the same maximum load. This is attributed to the symmetry of the 4x2 arrangement, whereby regardless of the orientation of the neutral bending axis, it is assumed to bisect the centerline of the structure such that opposite pairs of members will be equidistant from that line.

Table 16: NOROSK unity check results under ULS wind and worst-case ULS wave direction for each brace member

Brace ID	Unity Check
1	.888
2	.852
3	.852
4	.888
5	.831
6	.672
7	.672
8	.831

7.2. Design iteration

Though no further adjustments to the brace dimensions were required at this stage, a handful of test iterations were performed to examine the sensitivity of the design to the member dimensions, It was discovered that increasing the section length to from 22 to 24 meters would result in failure of members 1 and 4. Further increasing the length to 25 meters caused members 2 and 3 to also fail on the second unity criteria, which as mentioned in Chapter 4, is highly sensitive to changes in the slenderness ratio of the braces. The updated brace dimensions, validated in this section, undergo an additional validation step using finite element modelling in Chapter 9.

7.3. Resulting structure weight

Having finalized the dimensions for brace members and monopile shell through the analyses performed in the previous chapters, the overall weight of the Hybrid support structure can be calculated. The weight

reduction potential, compared to a traditional monopile, is the most commercially attractive design element of the Hybrid Monopile concept. Though the Hybrid Monopile requires additional welding, costs associated with the welded connections may be offset lower quantities of raw steel potentially lower installation costs.

With respect to the installation of large offshore support structures, transport of the structures to project sites continues becomes increasingly challenging as the weight of these structures grows faster than the carrying capacity of the installation vessels. For support structures weighing more than 1500 tons, the selection of capable vessels in scant. In water depths greater than 40 meters, nearly all standard monopile structures will fall into this heavyweight category. By comparison, a Hybrid Monopile structure suitable for water depths up to 50-meters will weigh in at approximately 1300 tonnes. Table 17 compares the complete support structure weights for a traditional monopile and a corresponding Hybrid Monopile, for water depths of 30, 40 and 50 meters.

Table 17: Total weight for each structure option

Structure weight, pile tip to transition piece	**Standard Monopile**	**Hybrid Monopile**
30 meters	1279 tons	1012 tons
40 meters	1491 tons	1151 tons
50 meters	1849 tons	1270 tons

As shown in the table, the Hybrid Monopile provides a weight reduction of 25-30%, primarily attributed to the reduction in foundation pile thickness made possible by the reduced wave-induced fatigue damage.

If installation vessel selection is a matter of hook height limitations, pending the availability of an underwater connection, the Hybrid Monopile would have the added versatility of modular transport and installation as two distinct parts. In this case, the split weight of the upper section, from 3.0 meters below the braced members up to the transition piece platform, would weigh approximately 655 tons, increasing the range of possible installation vessels.

8. Concrete-filled members

Due to the apparent sensitivity of the members to buckling, and the required increase in member dimensions stemming from the FLS check, the option of filling the members with a high strength concrete mixture was introduced. The introduction of the concrete mixture presents an opportunity to increase brace resistance to buckling, without adding additional steel, and allow for a reduction in the outer diameter, further minimizing available wave loading area.

Concrete filled steel tubes (CFST) potentially offer numerous benefits, both in terms of structure cost and dynamic performance [16]. Concrete fill within the tube will delay inward buckling of the steel under high bending loads, such as those experienced by an offshore wind turbine. Additionally, the strength of the concrete fill may be increased by up to 10% due to the confining effects of the steel tube [16]. This lateral pressure imposed by the steel tube prevents concrete spalling and provides increased shear capacity as well as improved performance under compression and bending [19]. From a cost standpoint, filling the tubes with concrete would allow for thinner shells, and therefore less steel fabrication costs. The tube itself acts as the concrete formwork, so installation costs are minimal. Filled columns have been shown to perform well under dynamic and seismic loading in high-rise, bridge, and offshore applications [19]. Eurocode IV for composite columns [42], provides a design method for this type of structure.

8.1. Concrete parameters

The relevant material properties for the proposed concrete fill are shown in Table 18.

Table 18: Concrete properties for CFST members

Young's modulus	35000	[MPa]
Density	2600	[kg/m^3]
Volumetric fraction of reinforcing fibres	1.00	[%]
Weight fraction of fibres	3.14	[%]

To address concerns regarding brittle behaviour of concrete-fill, reinforcing fibres are added to the mix design at a volumetric fraction of 1% (weight fraction of 3.14%), which literature review [20] indicates may improve the ductility of the encased concrete under cyclic loading by upwards of thirty percent. Since the addition of the concrete fill is predicted to improve the bearing capacity of the braces, the D/t ratio for the steel shell of the CFST members is increased from 20 to 30.

8.2. Equivalent beam model – Concrete-filled members

An updated equivalent beam model was created, once again using the finite-difference derivation of the Euler-Bernoulli beam, and the same soil springs as the previous model. The addition of the concrete-fill to the braced elements of the equivalent beam model is handled by recalculating the mass and stiffness of each element.

Mass per unit length of the composite member is calculated by:

$$\rho A = \ _{steel} * A_{steel} + \rho_{concrete} * A_{concrete}$$

In accounting for the corresponding stiffness EI of the composite member, Eurocode IV dictates that only 80% of the added stiffness from concrete be included in the design calculations. Though CFST structures have been shown to perform well under a variety of cyclic loading conditions [19], there is still limited knowledge regarding the dynamic interaction between the concrete and the steel, reflected by this scaling factor. Therefore, the composite stiffness EI of the hybrid sections are calculated as follows,

$$E_{section}I_{section} = E_{stee} \ * I_{steel} + .8 * E_{concrete} * I_{concrete} + E_{fibers} * I_{fibers}$$

Identical to the methodology employed in Chapter 4, the parallel axis theorem is used to determine the relevant second area moments of inertia. The addition of concrete will affect the anticipated fatigue life computations from Chapter 6 by altering the structure natural frequency, mode shape, and further reduced the available wave loading area near the waterline. To determine the extent of this area reduction, the members are assessed under ULS conditions to determine the minimum allowable dimensions, prior to performing any further analysis on the full structure.

8.3. Concrete-filled member loads – ULS

To perform the ULS checks on the concrete-filled members, the NORSOK standard is replaced with the condensed version of the Eurocode 4 [42] design method for composite columns. A complete guide to this methodology can be found in [56], but the most relevant aspects are covered in this section.

8.4. Summary of Eurocode IV for composite members

The proposed method accounts for the increased strength of the concrete due to the confinement effects of the tube, and determines what proportion of the applied load may be carried by the concrete core and steel shell respectively. In the condensed method, the tensile strength of concrete is completely neglected, as is any increase in strength from tensile cracking in the concrete, since both are insignificant compared to the tensile strength of the encasing steel.

Three potential failure modes are checked [56].

I. Failure due to exceeding the strain limit of concrete along the strong axis, crushing of the concrete

II. Failure of the concrete from excessive strain along the weak axis, cracking of the concrete

III. Failure of the steel tube, either by fraction on the tensile axis or buckling on the compressive axis

Displacement of the member resulting from bending loads leads to long term creep of the concrete, and a long-term reduction in strength. Long-term reduction is a function of the relative slenderness of the members, and is expressed as a reduction in the modulus of elasticity of the confined concrete. For

assessing the ULS and FLS load cases on the Hybrid Monopile brace members, a long-term strength reduction of 50% is prescribed.

It is important to note that since little is known about the interaction behaviour between the concrete core and steel shell under dynamic conditions, frictional forces between the concrete and steel casing are not explicitly addressed. Instead, the member resistance to loading is scaled using interaction curves that are assigned based on the ratio of steel and concrete areas within the composite member. The proposed concrete-filled tubes have a reinforcing steel ratio of less than 3%, corresponding to interaction curve a.

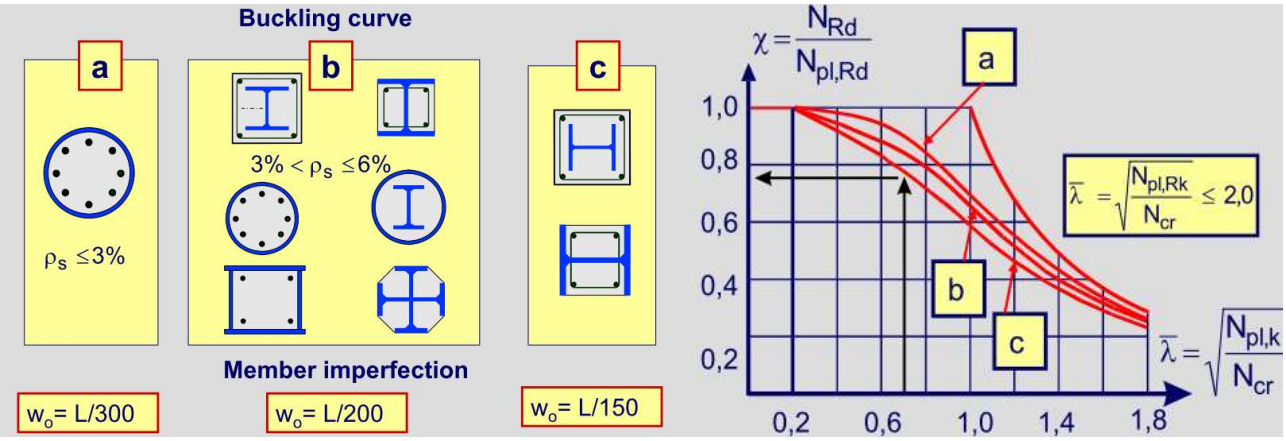

Figure 8-1: Buckling curve assignment for composite cross-section [56]

The scaling factor χ from the interaction curve is a function of the relative slenderness λ of the composite tubular. In the expression for λ, $N_{pl,Rk}$ is the characteristic value of the plastic resistance to compressive forces such that,

$$N_{pl,Rk} = A_{steel} * f_{y,steel} + A_{concrete} * f_{y,concrete} + A_{fiber} * f_{y,fiber}$$

and N_{cr} is the critical Euler buckling normal force in the member. EI_{comp} refers to the composite section properties as described in the previous section.

$$N_{cr} = \frac{\pi^2 EI_{comp}}{L^2}$$

Scaling factor χ is applied to the axial compressive loads, and an additional scaling factor α_m is applied to the bending loads. This factor α_m is material dependent, taken as .9 for S355 steel [56]. The final scalar, μ is a function of the ratio between the axial and bending loads. This factor is determined using the curve shown in Figure 8-2. The application of these scalars leads to the following unity check expression.

$$\frac{N_{applied}}{N_{resistance} * \chi} + \frac{M_{applied}}{M_{resistance} * \alpha_M * \mu} \leq 1.0$$

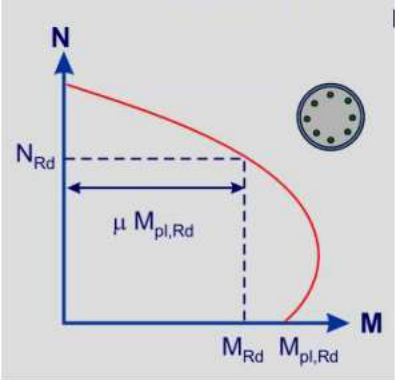

Figure 8-2: Determining scaling factor under combined axial and bending loads

Results of the unity check according to Eurocode 4, shown in Table 19, indicate that all eight braces successfully pass the unity check under ULS loads, and that as in the hollow case, braces 1 and 4 effectively "govern", with members 2, 3 also being significant.

Table 19: Utilization ratios for brace members (ULS) – worst-case wave misalignment

Brace	Unity Check
1	.965
2	.892
3	.892
4	.965
5	.869
6	.731
7	.731
8	.869

Like the NORSOK unity summary in Chapter 7, Table 18 shows the worst-case unity check resulting from the six possible wave approach directions.

8.5. Member dimension sensitivity

As in the case of the hollow brace members, a quick iteration of design dimensions was performed to assess the sensitivity of the check to changes in member design. This check revealed that the concrete-filled members are less sensitive to increases in length that the hollow steel tubulars, resisting failure for braces of up to 28 meters in length, attributed to the compressive strength of the concrete and that the allowable deflection w_o is a function of the member length. Alternatively, CFST members were shown to be more sensitive to changes in diameters. An outer diameter of .82 meters resulted in the failure of members 1,2,3 and 4. Having determined the appropriate member dimensions, the fatigue life assessment for the concrete-filled version of the Hybrid Monopile may be performed.

8.6. Effects on FLS assessment

Changing to the concrete-filled option is assumed to have a negligible effect on the accumulated fatigue damage from wind loads. Updating the damage calculations associated with wave loading is a simple matter of replacing the mode shape vectors, natural frequency values, and effective wave loading area in the wave-fatigue procedure given in Chapter 6.

The additional stiffness from the addition of the concrete fill results in an increase in the structure natural frequency from .205 Hz in the hollow case up to .216 Hz for the Hybrid option. Damage calculations for the concrete-filled Hybrid monopile are summarized in Table 20.

Table 20: Mudline fatigue life for Hybrid structure with concrete-filled members

Sea State	Wind Damage	Wave Damage	Total Damage
1	5.27E-05	1.44E-11	6.06E-05
2	3.77E-04	2.40E-05	4.35E-04
3	2.69E-03	6.28E-03	7.26E-03
4	3.33E-02	4.84E-03	3.87E-02
5	1.96E-02	4.62E-03	2.31E-02
6	5.16E-03	2.87E-03	6.65E-03
7	2.43E-03	1.64E-03	3.27E-03
8	3.11E-04	7.80E-04	8.90E-04
9	1.30E-04	3.61E-04	4.06E-04
10	5.82E-05	1.47E-04	1.68E-04
11	2.44E-05	6.01E-05	6.88E-05
12	8.46E-06	2.32E-05	2.62E-05
13	4.94E-06	9.39E-06	1.13E-05
14	1.93E-06	3.61E-06	4.38E-06
15	8.15E-07	1.38E-06	1.72E-06
16	3.44E-07	6.62E-07	7.98E-07
17	1.07E-07	2.57E-07	2.96E-07
18 (ULS)	3.12E-08	1.65E-07	1.77E-07
TOTALS	6.42E-02	2.17E-02	8.10E-02
Fatigue Life	**140 years**	**415 years**	**112 years**

The decrease in wave-induced fatigue damage results in an additional 22% increase in the overall fatigue life compared to the hollow case, and an over 200% increase in expected fatigue life at the mudline compared to the reference case monopile. This further increase in fatigue life compared to the hollow-case is attributed to the shift in the natural frequency further into the low energy portion of the wave forcing spectrum. As previously shown, for a Hybrid configuration, the mudline is no longer the governing location for structure fatigue.

8.7. Concrete-filled member loads – FLS

Shifting attention to the individual members, the decoupled fatigue methodology used to assess the hollow members is repeated for the concrete-filled option. To modify the method for the CFST braces, Eurocode IV is used to determine the bending moments, stresses, and subsequent Hot Spot Stresses in the members. Per Eurocode IV, as in the case of the ULS assessment, only ½ of the concrete area may be utilized to carry fatigue load. Inclusion of the concrete fill results in approximately a 25% reduction in the member stress ranges. The results of the fatigue-life calculations for the concrete filled members using the initial dimensions of D = .85 meters, and t = 28 mm, are shown below

Table 21: Concrete-filled brace fatigue life (initial dimensions)

Brace	Fatigue Life
1	138.3
2	138.7
3	138.7
4	138.3
5	328.2
6	329.9
7	329.9
8	328.2

All eight members clearly have more than adequate fatigue life, but further iteration of the member dimensions is not possible based on the results of the unity check in Section 8.3. It is apparent from these results that the design of the CFST braces is ULS driven.

8.8. Discussion on the use of CFST braces

It must be noted that these results are highly simplified assessments the do not adequately account for any dynamic interaction between the concrete and steel. The important assumption is also made that the concrete is perfectly flush with the steel shell at the top and bottom of the brace to distribute axial loads, but imperfect initial pouring of the concrete, crushing slumping or shrinkage of concrete over time, or expansion due to tensile cracking in the concrete core, would all invalidate this assumption. Ultimately the benefits of this configuration would be more commercial, due to the reduction in the required amount of steel, than structural. Serious consideration of this design option would require extension further analysis that is outside the scope of this project.

8.9. Overall structure weight – CFST option

The addition of concrete fill increases the overall structure weight, but allows for a further reduction in the required steel, due to the thinner member shells. Compared to steel, concrete is an inexpensive material, so though the concrete-filled design may not have additional significant structural benefits, it could still be a commercially attractive option. Table 22 compares the complete support structure weights

for a standard monopile, Hybrid Monopile, and CFST Hybrid, for water depths of 30, 40 and 50 meters. It should be noted that since the brace length is kept constant for these three cases, the mass of the concrete fill is independent of depth.

Table 22: Total weight for each structure option

Structure weight, pile tip to transition piece	**Standard Monopile**	**Hollow-Steel Hybrid**	**Concrete-filled Hybrid**	
			Steel	***Concrete***
30 meters	1279 tons	1012 tons	813 tons	227 tons
40 meters	1491 tons	1151 tons	912 tons	227 tons
50 meters	1849 tons	1270 tons	1083 tons	227 tons

Adding concrete fill provides a further 10% steel reduction, and a total weight reduction when compared to the reference monopile of approximately fifteen percent.

9. Finite element model analyses

In the previous chapters, the brace members have been assessed using design codes and standards that were not written with this type of unique brace configuration in mind. Additionally, the applied methods treat the individual members in isolation, neglecting their relationship with each other and with the largest structure, aside from the assignment of load factors. As a validation step to affirm that the selected brace dimensions are sufficient under extreme loads, finite element models of the updated Hybrid Monopile configuration and the reference monopile were prepared in ANSYS and meshed using Shell181 -type elements [3]. The model was also used to further validate the results of the Matlab-based modal analysis, given the sensitivity of the fatigue calculations to the structure natural frequency.

9.1. Modal analysis verification

Verification of the modal analysis results requires full length models of the base case monopile and hollow-steel 22-meter Hybrid configurations. The rotor-nacelle mass and flanged connections are represented by added mass elements at the appropriate locations. Spring elements were added to the pile section below the seabed in accordance with the previously calculated PY-curves from Chapter 4. Due to the uncertainty regarding the connection detail at the time of modelling, overlapping areas between the Hybrid section braces and the monopile sections were fixed with rigid elements. The resulting first mode shape of each model is shown in Figure 9-1, and the 1st and 2nd calculated natural frequencies are compared to the Matlab-based model results in Table 23..

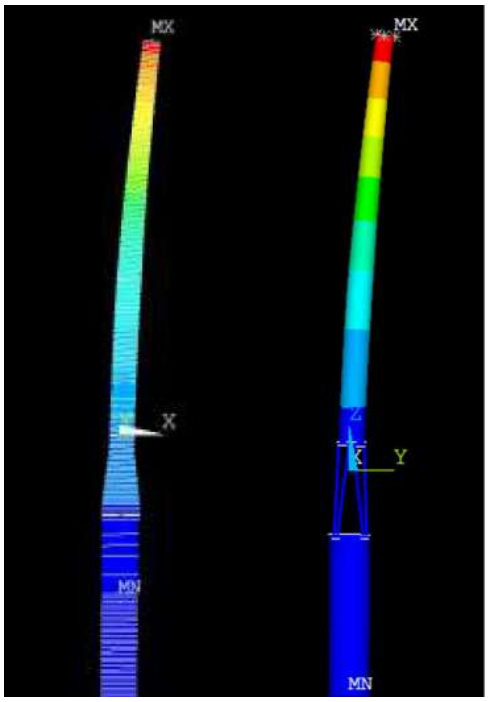

Figure 9-1: 1st mode shape, reference monopile and Hybrid counterpart

Table 23: Natural frequency result, ANSYS model

	Base Case (ANSYS)	Base Case (Matlab)	Hybrid Case (ANSYS)	Hybrid Case (Matlab)
1st freq.	.223	.226	.196	.205
2nd freq.	.799	.823	.856	.789

The resulting natural frequencies for the base case agree well with those determined by the equivalent beam model in Matlab, showing differences of 1.3% and 2.8% for the 1st and second natural frequencies respectively. In the Hybrid case, the first natural frequency is approximately 4% lower than expected. This could be attributed to the artificial constraints placed on the model in lieu of a proper welded connection. As previously mentioned, the welded connection detail between the brace member and monopile shell is still under development at the time of this work, so in the ANSYS model, the overlapping elements are rigidly fixed using MPC-184 rigid link beam elements.

9.2. ULS loads expressed as displacement

To validate the survival of the brace members under the ULS load cases using the ANSYS model, loads must be applied a distance away from the brace ends to avoid the distortion of the results by high stresses at the point of direct application. To manage this, the full-size model used in the modal analysis reduced to a truncated section extending 3.0 meters above and below the point where the brace members overlap the monopile shells.

Loads and degree of freedom constraints are then applied to the end sections of the truncated model. Since the ULS checks allow for a static assessment of the structure, the combined effects of the extreme wind and wave loads can be efficiently applied to the structure as simple displacements of the cut cross sections.

The magnitude of the displacement under ULS conditions at the relevant cross sections are obtained from time simulations using the equations of motion for the Euler-Bernoulli beam model under an external force, computed for nodes 1 to N.

$$\rho A * \begin{bmatrix} 1 & 0 & 0 \\ 0 & 1 & 0 \\ 0 & 0 & 1 \end{bmatrix} \begin{bmatrix} \ddot{u}_1 \\ .. \\ \ddot{u}_N \end{bmatrix} + [\boldsymbol{C}] * \begin{bmatrix} \dot{u}_1 \\ .. \\ \dot{u}_N \end{bmatrix} + \frac{EI}{l^4} * \begin{bmatrix} 1 & -4 & 6 \\ 0 & 1 & -4 \\ 0 & 0 & .. \end{bmatrix} * \begin{bmatrix} u_1 \\ .. \\ u_N \end{bmatrix} = \begin{bmatrix} F_{Morison}(t) \\ .. \\ F_{Wind}(t) \end{bmatrix}$$

Damping matrix [**C**] has not been used up to this point, but the derivation was provided in Chapter 2 such that.

$$[\boldsymbol{C}] = 2\boldsymbol{\zeta}\sqrt{\boldsymbol{K} * \boldsymbol{M}})$$

Where $\boldsymbol{K}$ and $\boldsymbol{M}$ are mass and stiffness matrices from the beam equation. The $[\boldsymbol{C}]$ matrix is the same size as the $\boldsymbol{K}$ and $\boldsymbol{M}$ matrices, and is populated by performing the above operation for each entry.

The diagonal mass matrix $\boldsymbol{M}$ will produce a diagonal damping matrix as well. Displacement of each element is then found as the steady state response of the system at each timestep of the series found by:

$$\begin{bmatrix} u_1(t) \\ .. \\ u_N(t) \end{bmatrix} = \begin{bmatrix} F_{Morison}(t) \\ .. \\ F_{Wind}(t) \end{bmatrix}^{-1} * \left(\rho A * \begin{bmatrix} 1 & 0 & 0 \\ 0 & 1 & 0 \\ 0 & 0 & 1 \end{bmatrix} + [\boldsymbol{C}] + \frac{EI}{l^4} * \begin{bmatrix} 1 & -4 & 6 \\ 0 & 1 & -4 \\ 0 & 0 & .. \end{bmatrix} \right)$$

$$\begin{bmatrix} u_1(t) \\ .. \\ u_N(t) \end{bmatrix} = \begin{bmatrix} F_{Morison}(t) \\ .. \\ F_{Wind}(t) \end{bmatrix}^{-1} * \left([\boldsymbol{M}] + [\boldsymbol{C}] + [\boldsymbol{K}] \right)$$

Displacements $u_{50}(t)$ and $u_{80}(t)$ are extracted as the section displacements 3.0 meters above and below the welded connection details at the brace ends. The displacement signal at each of these points of interest may also be determine by solving the equation of motion at each time step using Duhamel's integral, treating the applied force at each timestep as an impulse load. Displacements $u_{50}(0)$ and $u_{80}(0)$ from the matrix equation are used as the initial condition x_o at timestep t = 0 in the equation for each location. Initial velocity is set equal to zero at the first timestep. At each subsequent time step:

$$x_o = x_n(t - dt)$$

$$v_o = (x_n(t - dt) - x_n(t - 2dt))/dt$$

$$\omega_1 = \omega_o * \sqrt{1 - \zeta^2}$$

$$m = \sum_{i=1}^{i=n} [\boldsymbol{M}(\boldsymbol{i}, \boldsymbol{i})] \qquad F(t) = \sum_{i=1}^{i=n} [\boldsymbol{F}(\boldsymbol{i})]$$

$$x_n(t) = e^{-\zeta \omega_o t} * \left[x_o \cos(\omega_1 t) + \left(\frac{\zeta x_o \omega_o}{\omega_1} + \frac{v_o}{\omega_1} \right) * \sin(\omega_1 t) \right] + \int \frac{1}{m * \omega_1} * F(t) * e^{-\zeta \omega_o} * \sin(\omega_1 t)$$

The time histories of the displacement at the points of interest produced using the two different methods show very similar results. The difference in displacement between the two points of interest, calculated both with the matrix equation of motion and with Duhamel's integral, is plotted in Figure 9-2.

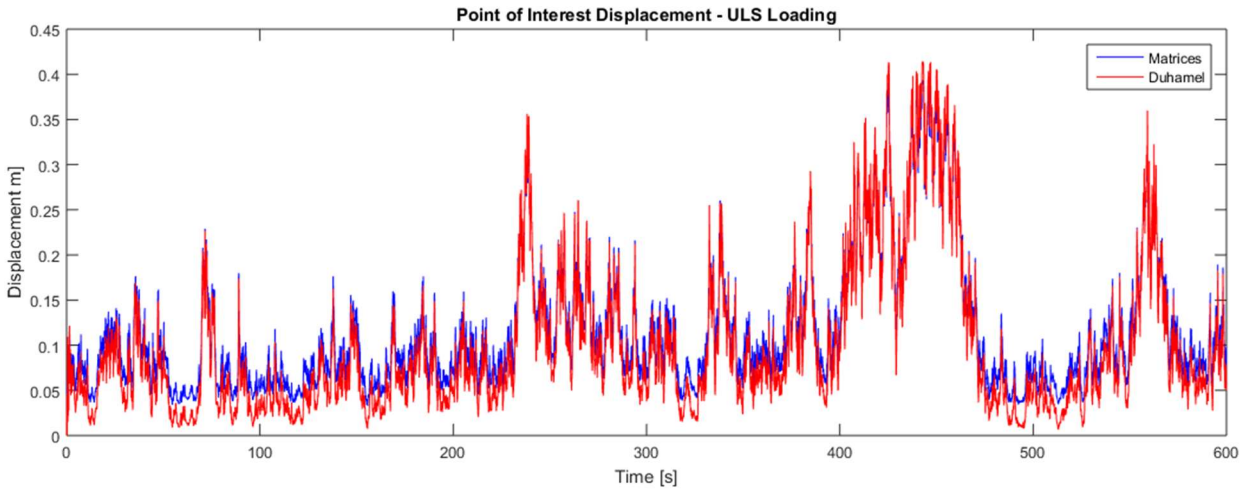

Figure 9-2: Cut section displacement under ULS loading

To apply these displacements to the truncated finite element model, the lower cross section is rigidly fixed in all translational degrees of freedom, and a displacement, corresponding to the maximum displacement difference between the top and bottom sections, is applied to the upper cross section. Figure 9-3 shows the resulting stress distribution in the truncated model that results from the applied displacement. An overhead view of which is given in the adjacent figure.

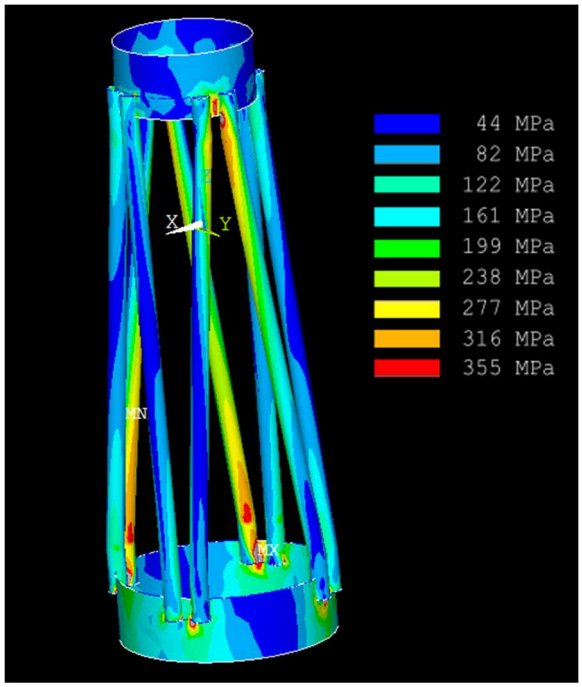

Figure 9-3: Stresses resulting from ULS load case

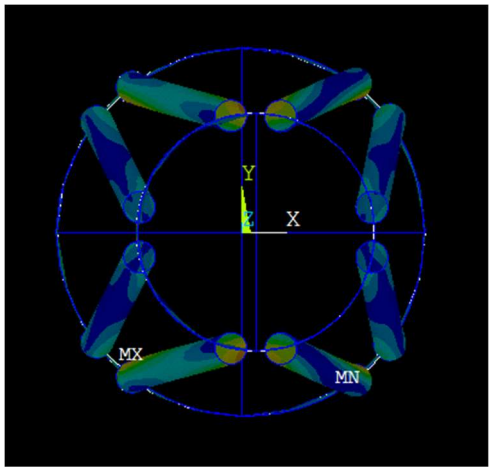

Figure 9-4: Top view of Hybrid under ULS loading

In Figure 9-3, it is apparent that there are certain locations in the structure where the stress exceeds the 355 MPa yield stress of steel. The points where the yield stress is exceeded correspond to the locations where rigid MPC element links are used, and at the locations on the member braces where the straight brace bends into a vertical stub to accommodate the weld detail. The use of rigid links is known to result in localized stresses at the link location [3]. Time permitting it would be advisable to refine the mesh in these areas to avoid those apparent high stresses. Stresses at the stub are more problematic, a goal of the ongoing connection detail research is to potentially eliminate this bend from the design entirely. Given the status of that work at the time of this report, the high stresses at the brace bends are not addressed further. In the straight sections of the brace members, the peak stress appears to be between 277 and 316 MPa, neglecting the effects of the localized connection stresses. This would correspond to a brace strength utilization ratio between .780 and .890, showing good agreement with the NORSOK results for the same ULS load case, given in Chapter 7.

9.3. Other load cases

The ANSYS model of the structure is also used to evaluate the structure under two additional load cases, a ship impact to evaluate the accidental limit state, and an installation load representative of that applied by the Fistuca BLUE Piling hammer.

9.4. Accidental Limit State

The accidental limit state check assesses the resistance of the structure to an inadvertent collision with a maintenance vessel. To examine the worst-case scenario for this impact, it is considered that the full impact force of the vessel is applied to a single member. During detailed design of an offshore wind turbine, design codes provide methods that account for specific dimensions and features of a specific vessel. In the absence of this ship specific information, codes instead prescribe an impact force, an area on which to apply the load, and a parameter to describe the duration of the impact, in the form of rise and decay time steps.

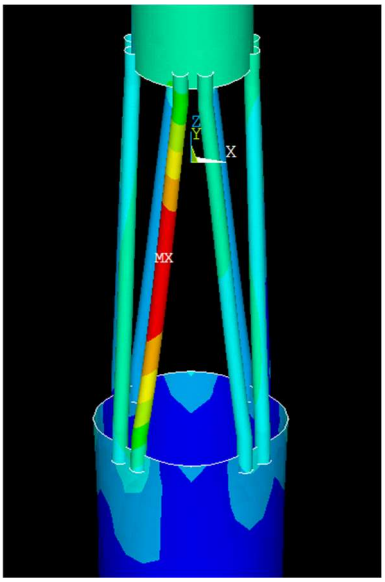

Figure 9-5: Accidental boat impact load – resulting displacement

To assess the Hybrid Monopile, the impacted brace is assessed using the procedure for a jacket leg given in DNV-RP-C204 [69]. The local concentrated collision force is considered evenly distributed over a rectangular area. For a vertical leg, a force of 5.4 MN is applied to a contact area with dimensions of .20 meters x 1.15 meters [69]. The load is applied in the ANSYS modelled as a transient pressure on the specific area for a period of .34 seconds.

Figure 10-2 shows the element displacements in the FE model after the applicable of the load. The maximum displacement of the brace member is extracted from the results and used to determine whether the maximum allowable strain is exceeded. For S355 steel, a critical strain value of 20% is assigned. The maximum displacement corresponds to a strain of 12% and satisfies the basic criteria.

9.5. Installation

Discussed in Chapter 1, a challenge to the practicality of the Hybrid Monopile is determining a feasible installation method. The ideal option would be to install the complete structure, from the transition piece to the embedded pile, as a single unit, since the alternative two-part installation is dependent on an underwater connection still in the early stages of development. Strike loads on the top flange from a traditional hydraulic piling hammer would catastrophically damage the slender brace members. Even if the brace members could endure the hammer strike, the rapid change in cross sectional properties at the Hybrid section would likely result in the emission of excessive noise, violating environmental protection measures.

However, low-intensity driving, using Fistuca BLUE Piling Technology, is a viable alternative. The BLUE Piling Hammer consists of a large cylindrical water tank, placed directly on the top flange, which houses a small combustion chamber in the base. Controlled, intermittent combustion of pressurized gas, accelerates the water column upwards, and induces a downward reaction force onto the pile, the gravity of the water column falling back into place then provides a secondary blow. The low frequency, low-intensity blows more closely resemble pushing the pile into place as opposed to striking it, resulting in minimal vibratory response in the pile and up to 80% less noise production.

Internal reports from Fistuca BV indicate that the high-end of the anticipated hammer load is approximately 200 MN. This expected load is applied to the truncated finite-element model as a series of twenty 10 MN point loads distributed evenly around the circumference of the top cut section. The bottom cut section is restricted from translation in the X, Y, and Z directions, to mimic the worst-case scenario in which a pile is stuck during installation and must absorb the full hammer load.

The installation analysis using the truncated finite element model applies the low-frequency hammer force as a static vertical load. Figure 10-1 shows the resulting stress in the truncated structure section caused by this applied load. From the results, it is confirmed that the limit stress is not exceeded in the brace members. Use of the BLUE Piling Hammer will depend on the resulting stresses in the connection details once finalized, as that will be the governing design location.

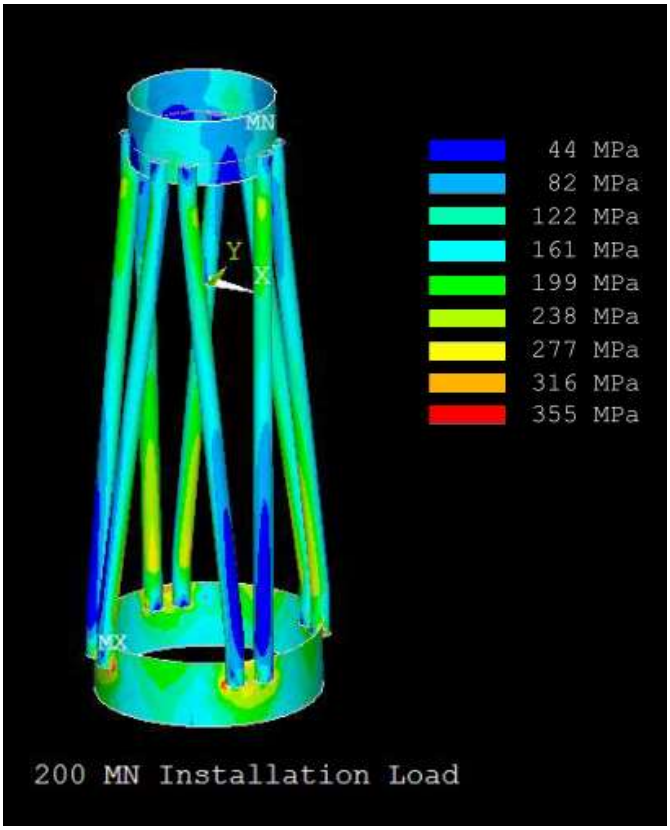

Figure 9-6: Stress resulting from 200 MN installation load

10. Sensitivity Analysis

Based on the first two design phases, which have been presented in Chapters 4 thru 9, the Hybrid Monopile appears to be an attractive alternative support structure concept, for a large offshore wind turbine, at a North Sea site with a water depth of 40 meters. However, to be a competitive option in the offshore support structure market, the design must be suitable for use within a range of different wind farm conditions, with minimal modification, to allow for cost effective mass production. In the third design phase, the Hybrid Monopile design process outlined in this report is performed for a range of locations and turbine sizes to approximate new "optimal" Hybrid set-up for each condition. Data from these site-specific Hybrid optimizations are then used to identify the critical variables that drive the structure dimensioning. Finally, that information is used to guide the condensing of all possible iterations of the Hybrid Monopile, into a limited number of possible arrangements for each turbine size, which can easily be selected for a wind farm based on the water depth and wave spectra.

10.1. Variables for design iteration

With the current offshore wind industry trends in mind, a set of 6 variables are defined from which to iterate the Hybrid monopile. Turbine sizes were selected to cover the range from the largest currently available commercial turbine at 8.0 MW, up to 20 MW, which the DNV predicts will be available in the market prior to 2050. Base diameters were selected based on a similar rationale. A limited number of monopile production facilities are currently capable of producing 10.0-meter dimeter piles, and there is word of investment in equipment to produce 12.0-meter piles. Top diameter sizes are predicted to be more stable, but 8.0-meter diameter tower base are currently being discussed for accommodating larger turbines [52].

Table 24: Variable ranges for sensitivity analysis

Variable Name	***Range***				
Turbine Size (MW)	8.0	10.0	12.0	15.0	20.0
Water Depth (m)	30	40	50	60	
Base Diameter (m)	10	12	14		
Top Diameter (m)	6.5	8			
Metocean Condition [region]	North Sea	US East Coast			
Concrete fill [yes/no]	Yes	No			

The six variables in Table 24 make up 480 unique combinations for which a potential Hybrid Monopile configuration is determined.

10.2. Site selection

The sensitivity analysis focuses on sites with water depths of 40 to 60 meters, where traditional monopiles have not yet been attempted, as well as water depths between 30 and 40 meters, where monopiles are feasible but possibly undesirable. Figure 10-1 highlights where there potential development areas are located within the North Sea.

The first map depicts the bathymetry of the North Sea, with the areas where the water is less than 30 meters deep highlighted in pink. Largely, the viable wind farm sites in these highlighted areas have already been developed, or are leased for future development.

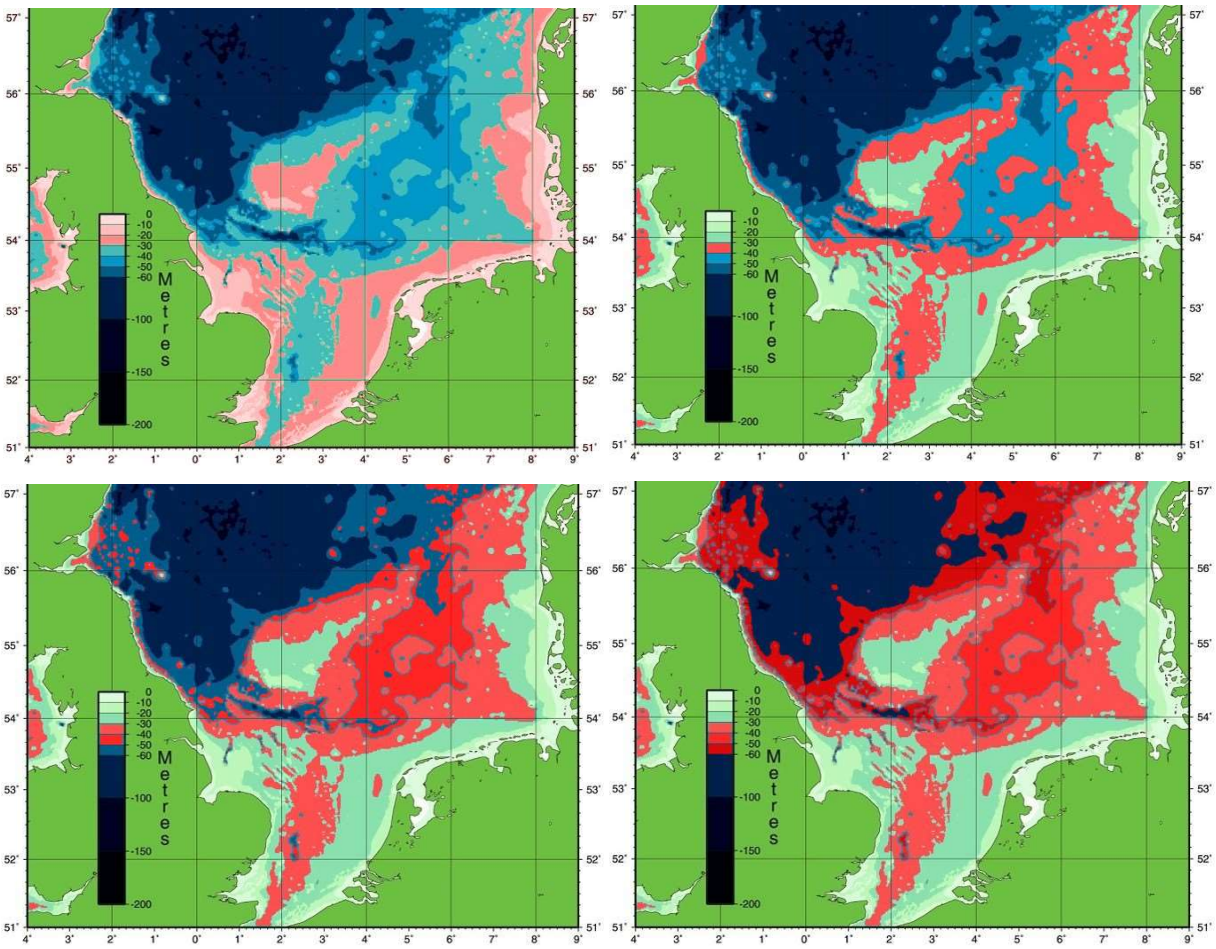

Figure 10-1: North Sea areas with water depths less than 30 meters and potential North Sea regions for Hybrid Monopile applications with water depth from 40 to 60 meters

Subsequently, the following three maps highlight the regions that may be "unlocked", or made more attractive targets for wind park development, using the Hybrid Monopile. To avoid unintendedly skewing the Hybrid design towards metocean conditions present in the North Sea, sites in other geographic regions were also used in the assessment.

Though the United States is has just recently entered the offshore wind industry, the east coast of the United States is a particularly interesting area for the Hybrid Monopile, as an estimated 628 GW of wind-farm potential are available in coastal regions within water depths of 30-60 meters, as shown in Figure 10-2.

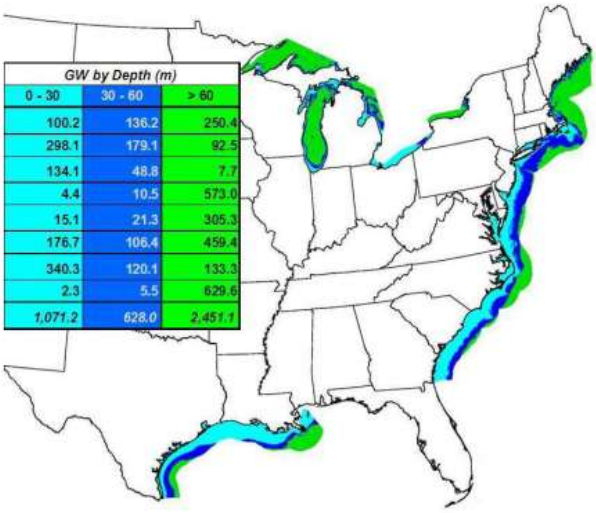

Figure 10-2: Eastern US offshore wind potential – modified form [5]

The late entry of the United States into offshore wind has been partially attributed to citizens aversion to wind farms that are visible from shore, making approval for farms in the 0 to 30-meter depth range difficult to obtain. However, as European developers continue to push wind farms further offshore, the 30 to 60-meter range becomes even more attractive.

10.3. Turbine size

To compute the necessary design parameters for the hypothetical 10, 12, 15, and 20 MW turbines, historical data for current wind turbine models was compiled, and used to extrapolate the required information. It was decided to limit the turbines used for the data extrapolation to offshore turbines between 3.6 and 8.0 MW, and to three of the leading manufacturers of offshore wind turbines, Siemens, Vestas, and General Electric. Data was analysed for both blade radius per rated capacity, and top mass per rated capacity, both of which are increasing at a decreasing rate, as the wind energy generators become more efficient. A logarithmic trendline was fit to the rotor radius data yielding the following:

$$R = \frac{56.77 * \ln(MW) + 45.48}{2}$$

Once the rotor radii were calculated, the corresponding increased hub height was computed using a DNV recommended safety gap of 6.0 meters from the blade tip at its lowest passing point, and the transition piece platform. During the scaling process, to determine the relevant operational frequency ranges, the tip speed was kept constant at 100 m/s, considered optimal based on current materials [50]. It should be noted that at the restricted tip speed, and with the increased blade length, the 1P frequency zone of the

turbine overlaps further with the environmental excitation spectra, and subsequently also moves the structure frequency further into that range. Tower top mass, expressed as tons/MW, was approximate using the same sample turbines.

The cut-in wind speed and cut-out wind speed, for each of the four turbines is kept constant, and the rated wind speed reduced by .5 meters per second for each turbine larger than the 8 MW reference, since larger turbines reach their rated power at lower wind speeds. These parameters provide enough information to reemploy the turbine calculator tool used in Chapter 6 to compute rotor loads for each at sea state on the three mega turbines [70].

Table 25: Assumed turbine properties for design iteration

Rated Power	Blade Radius [m]	Tower Height [m]	Top Mass [ton]	Max Thrust
8.0 MW	82.0	109.0	460	2.4
10.0 MW	87.0	114.0	530	2.8
12.0 MW	92.0	119.0	600	3.2
15.0 MW	98.0	125.0	690	3.7
20.0 MW	106.0	133.0	840	4.3

The turbine tower dimensions of the reference 8 MW turbine are subsequently scaled to accommodate the new turbine. Tower top and bottom diameters and D/t ratios are adjusted such that when the dimensions are linearly interpolated along the tower, as done in Chapter 4, the yield check will not exceed 250 MPa at any point on the tower. Since the tower is outside the jurisdiction of the support structure designer, no further design checks are performed.

10.4. Alternate locations

In addition to the 40-meter sample site, three additional sites were selected from the Central North Sea with in the 30, 50 and 60-meter depth areas highlight in 11-1. Historical wind and wave data for the formulation of sea states at the selection locations is obtained from a 2001 offshore technology report for the region [57]. Many of the measurement stations in the North Sea are owned and manged by private industry, so more recent comprehensive data is not publicly available. For prospective sites on the east coast of the United States, data obtained by National Oceanic and Atmospheric Administration measurement stations is readily available [18]. Figure 10-3 shows the locations of three of the locations considered, a 4th, off the coast of Virginia is located further South.

10.4.1. Note on the discretization of sea states

Buoy data for the alternative locations was then discretized into equally spaced bins of wave height, wind speed, and peak period. However, as wave loads begin to dominate the fatigue damage on larger support structures, it becomes apparent that this somewhat random discretization of the sea states can lead to drastic over or underestimations of the resulting fatigue damage [53]. This is attributed to the fact that a substantial portion of the fatigue damage will result from excitation occurring at or near the structure

natural frequency. Using the current discretization methods, this frequency block may fall entirely into only one or two bins, and the dynamic amplification factor associated with that bin may be over, or underestimated, depending on the difference between the peak period bin edge and structure period.

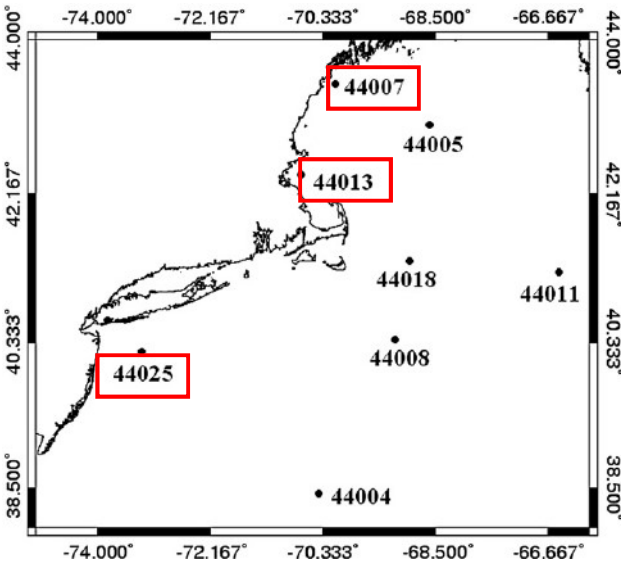

Figure 10-3: NOAA buoy locations for alternate Hybrid analysis locations

It has been suggested that instead of equally spaced bins, bins with edges near the natural frequency should be broken up into much smaller segments, and bins further away, where there is less energy in the response spectrum, may be stretched. Due to time constraints, this updated discretization method was not applied to the data used in this sensitivity analysis, but is recommended as a future check considering the high level of sensitivity of the structure to changes in location/wave spectra.

10.5. Design procedure

The iterative Hybrid optimization is performed using a Matlab-based program. The analysis of uses a series of design building blocks, or modules, which are then looped and revisited until reference monopile and hybrid monopile designs are produced, which meet all the design criteria discussed thus far in this report, are achieved, or a maximum allowable number of iterations is reached without a successful design.

Results at the end of each building block are checked, and if they fall above or below a specified value, may trigger a new iteration of the design and a return to the geometry definition module to adjust dimensions before resuming. Each time a change is made to the geometry, all previous blocks are revisited to ensure that no previously successfully design checks are at risk of failure based on the changes. If earlier design checks fail, the changes are reverted and the process moves to the next module.

The role of each module in the design procedure is as follows.

Module 1: Takes user inputs and selects the corresponding wind/wave spectrum and array of sea states

Module 2: Generates time-series of wind speed from the spectrum fetched in block 1. Calculates the corresponding rotor loads, and builds arrays that store the tower elements of the equivalent beam model

Module 3: Builds the arrays of equivalent beam properties for the reference monopile, performs the modal analysis, and checks that the 1st natural frequency does not fall below the 1P blade passing frequency.

Module 4: Follows the same procedure as Module 3, but for the Hybrid structure.

Module 5: Runs the three ULS load cases, calculates the base shear, overturning moment, pile penetration, and computes the NORSOK criteria for the brace members.

Module 6: Computes the combined mudline fatigue under wind and wave loading.

Module 7: Calculates the brace fatigue life for each member.

Module 8: Approximates the capital costs of the structure using different factors of Euro/kilo for different types of sections.

Module 9: Summarizes the results of interest, save them to a results files, and prepares plots of the chosen data.

The flow chart serves to illustrate how the procedure moves through these modules.

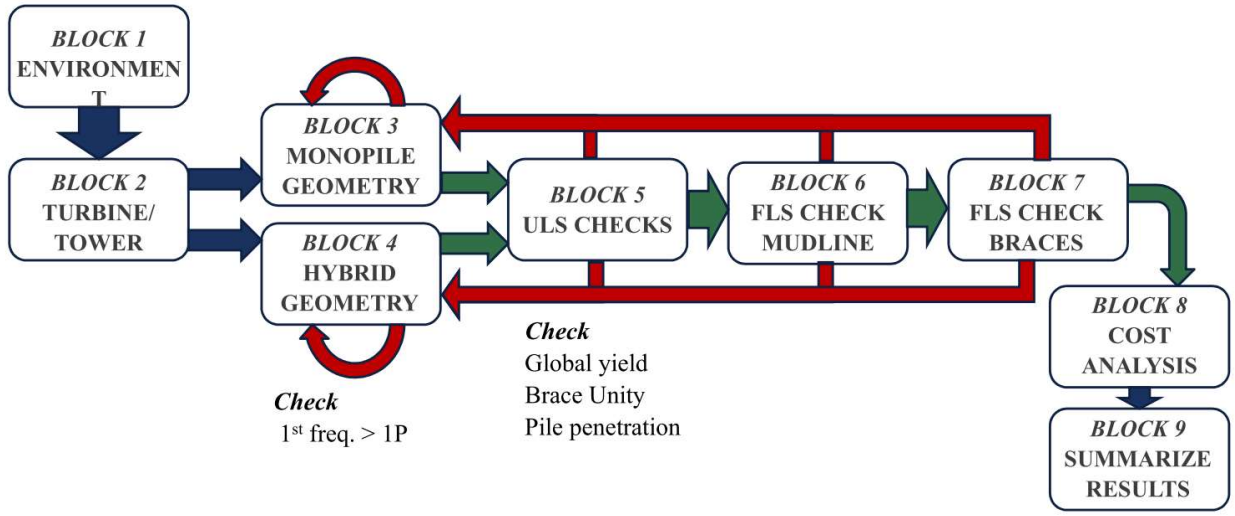

Figure 10-4: Hybrid monopile design procedure flow chart

The first design checks occur when Modules 3 and 4 are reached. If the 1st natural frequency of the structure falls within the 1P operating range, the pile embed depth and shell thickness will be incrementally increased until that criteria are satisfied. Each time the program loops back to the geometry

modules, additional adjustments are made based on what triggered the failure. Modules 5,6, & 7 also contain criteria to identify when the structure may be overdesigned, and can prompt a geometry adjustment without failing a design check.

Failure in module 5 may prompt:

- Pile lengthening/shortening
- Increase/decrease in monopile D/t ratio
- Increase/decrease in brace outer diameter

Failure in module 6 prompts:

- Increase/decrease in monopile D/t ratio

Failure in module 7 prompts:

- Increase/decrease in brace outer diameter

The geometric modules are set up in such a way that the geometry of the entire structure can be defined from the user inputs for turbine size, monopile top diameter and monopile bottom diameter, kept constant in the procedure, and the additional program-assigned variables of pile length, pile D/t ratio, and brace outer diameter, which are subsequently optimized. After several iterations, these optimized properties will be determined as a function of specific trigger counts, i.e. if the monopile was shown to be overdesigned in Module 5, but then fail a yield check the first time it passes through Module 6, the D/t ratio may look like

$$Monopile\left(\frac{D}{t}\right) = 120 + 10 * (Trigger_5) - 5 * (Trigger_6)$$

Where there "Trigger" terms are a count of the iterations prompted by a certain behaviour of interest. Defining the geometry in this fashion allows for ULS and FLS to be addressed concurrently during the optimization. The design of the monopile shell is considered "optimized" when the expected mudline fatigue life falls between 50 and 70 years. For the brace members, which are ULS driven, the optimization corresponds to a unity check result great than .80 for the governing member. The results for each simulation are saved directly to an Excel file for further analysis.

10.6. Insight from initial results

In the first round, approximately 1 out of every 5 variable combinations failed to produce a Hybrid design which passed all the necessary design checks. Of this failing group, three quarters of them either included a top diameter of 6.5 paired with a turbine size of either 15 or 20 MW. Intuitively this is logical. The 6.5-meter top diameter is inadequate to distribute the extreme bending moments produced by the supersize 15 and 20 MW turbines, and the larger brace dimensions required to support the turbine, do not sufficiently reduce the wave loading near the waterline when tightly spaced to the smaller top diameter. The remaining "failed" attempts involved parring a 10-meter diameter base and either a 15 or 20 MW

turbine water of 50 meters deep or more. in 50 or 60-meter water depths. Once again, this in unsurprising as, like the 6.5-meter top diameter, the 10-meter base diameter in these failing casings is insufficient to distribute the large bending moment from the turbine. Figure 10-5 shows the percent reduction of five key variables, for the configurations which successfully met all required design checks.

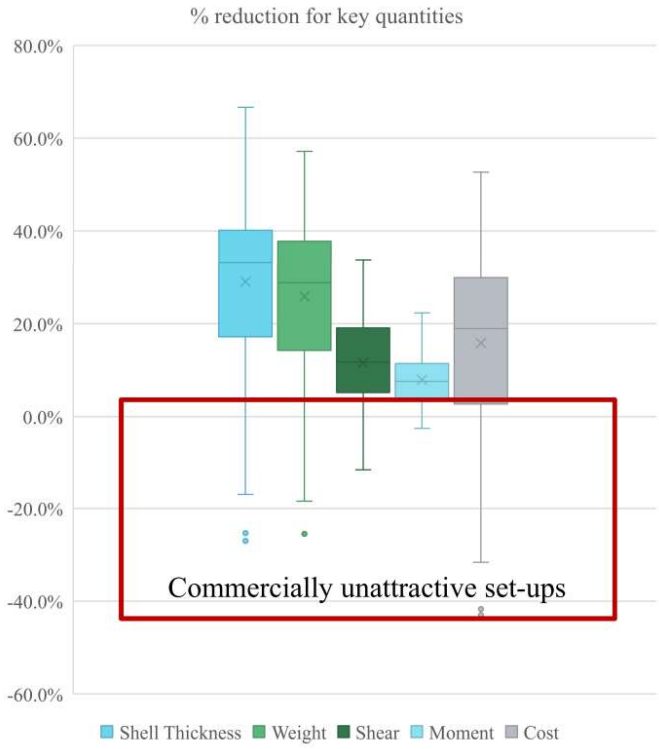

Figure 10-5: Reduction % for key quantities - passing configurations

As shown in the figure, there are certain structure configurations which pass all required design checks, but do so without offering any shell thickness, or steel weight reduction compared to a traditional monopile, thus losing the commercial advantage. For example, to accommodate a 20 MW turbine at a 40-m site on the East Coast, with a top diameter of 6.5 and a bottom diameter of 8.0 would require braces on the order of 1.3 meters in diameter with a 67-mm thickness. This results in a 52% increase in structure weight compared to the reference monopile, and an *increase* in wave loading, requiring a thickness monopile shell compared to the reference case. Overall, 85% of the passing simulations showed a possible reduction in monopile shell thickness for the Hybrid case. Figure 10-6 compares the resulting shell thickness for the reference and Hybrid monopiles, and the anticipated fatigue life in the shell at the mudline for each case.

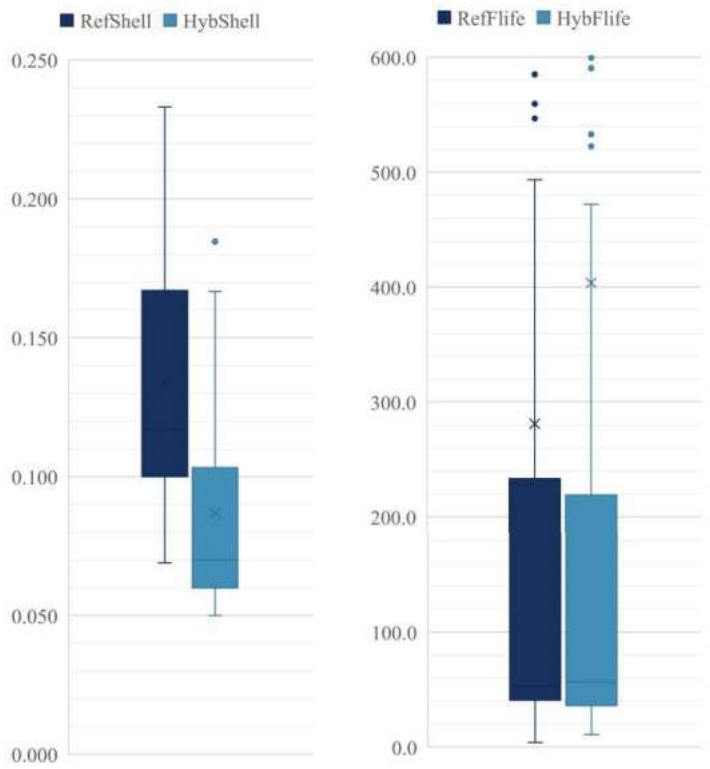

Figure 10-6: Comparison of sensitivity analysis results shell thickness and fatigue life

As previously discussed, a reduction in shell thickness is the most attractive aspect of the Hybrid Monopile design. The resulting box and whisker plots clearly depict that implementation of a Hybrid Monopile support structure facilitates a reduced shell thickness without a reduction in the expected fatigue life in that shell. Mean simulation results of other key variables, excluding results for configurations that did not pass the required design checks, are shown in the table below.

Table 26: Average results of initial sensitivity analysis simulations

Monopile shell reduction	30.7 %
Mean D/t Ratio (reference pile)	107
Mean D/t Ratio (Hybrid pile)	156
Weight reduction	27.41%
Cost reduction	17.6 %
Base Shear Reduction	12.4 %
Moment Reduction	8.3 %
Pile penetration reduction	2.0 meters

The full set of results from this set of simulations was used to establish a limited set of Hybrid Monopile configurations for each turbine size, creating a design template for the support and a scaling plan for future eras of turbine.

10.7. Recommended dimensions for a standardized Hybrid Monopile

In industry practice, both jacket and monopile support structures are custom designed for each turbine within a wind farm, under the rationale that designing all structures for the worst-case scenario within a farm would leave to expensive overly conservative design. However, in discussing the Hybrid monopile concept with industry experts, the consensus was that to maximize the commercial viability of the structure, standardization of the brace member section would be vital. The popular opinion is that cost savings from the standardization of the section, a combination of reduced engineering and production efforts, would far outweigh and losses associated with overdesign.

To establish the reduced set of the Hybrid Monopile configurations, each turbine size was assigned an "era", or range of years within which it was predicted to be the largest available turbine size. The assigned years are based on the latest DNV predictions for the evolution of offshore turbines [35]. Diameters of the tower base and monopile are then assigned to each era as well, based on projected manufacturing capabilities. For instance, it is illogical to pair a 14-meter diameter monopile base with an 8 MW turbine, since by the time a 14-meter pile is readily available, 8 MW turbines will likely have been superseded by a larger model. For each era, the assigned base diameter may not exceed the foreseeably available size. Additionally, a larger base diameter is not assigned purely based on availability, but out of necessity to accommodate large overturning moments from large turbines or deep-water conditions. Table 27 shows the prescribed top and bottom diameters for the reduced set of era-based Hybrid Monopile configurations. The appropriate brace dimensions for each configuration are determined by further reducing the complete results set from the initial optimized simulations, and selected the largest brace dimension corresponding to the diameter/turbine combinations in Table 27.

Table 27: Hybrid monopile dimension assignments for each turbine era

Turbine [MW]	*Era [years]*	*Top D [m]*	*Base D [m] depth 30/40*	*Base D [m] depth 50/60*	*Brace Size [m/mm]*
8.0	Present - 2020	6.5	10.0	10.0	.95 / 48
10.0	2020-2025	6.5	10.0	10.0	1.00 / 50
12.0	2025-2035	8.0	10.0	12.0	1.05 / 53
15.0	2035 – 2045	8.0	12.0	14.0	1.10 / 55
20.0	2045 - 20??	8.0	12.0	14.0	1.15 / 58

Brace lengths are fixed at 22 meters for the 30 and 40-meter sites, and extended to 26 meters for the 50 and 60-meter sites. Figures 10-7 and 10-8 illustrate the standardized configurations for the 8.0 MW and 20 MW turbine eras.

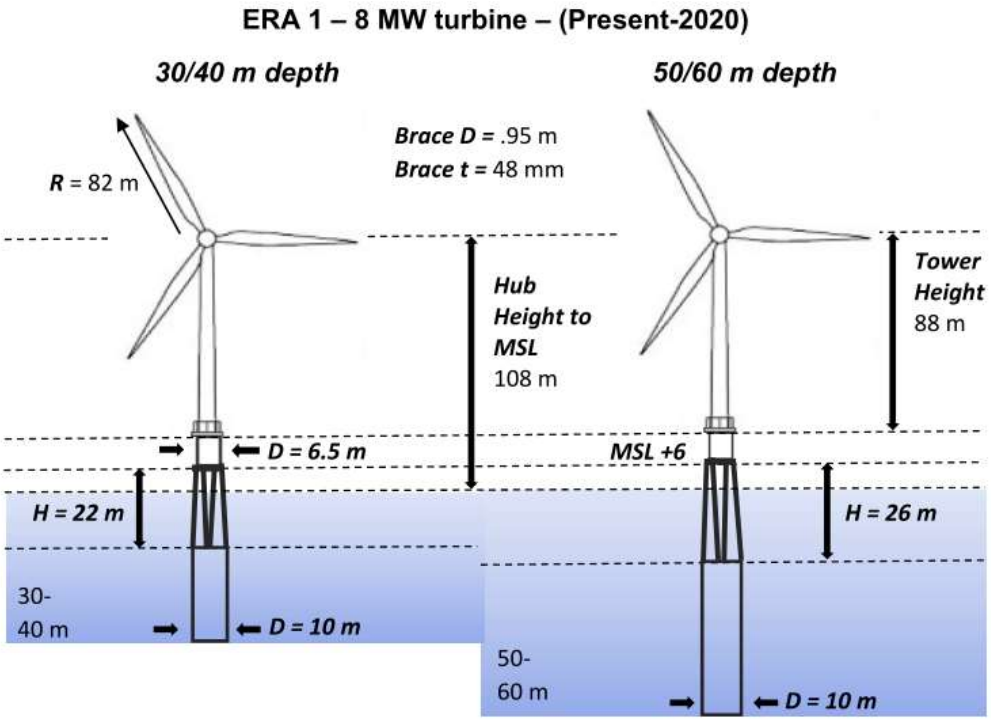

Figure 10-7: Era 1 standardized Hybrid Monopile

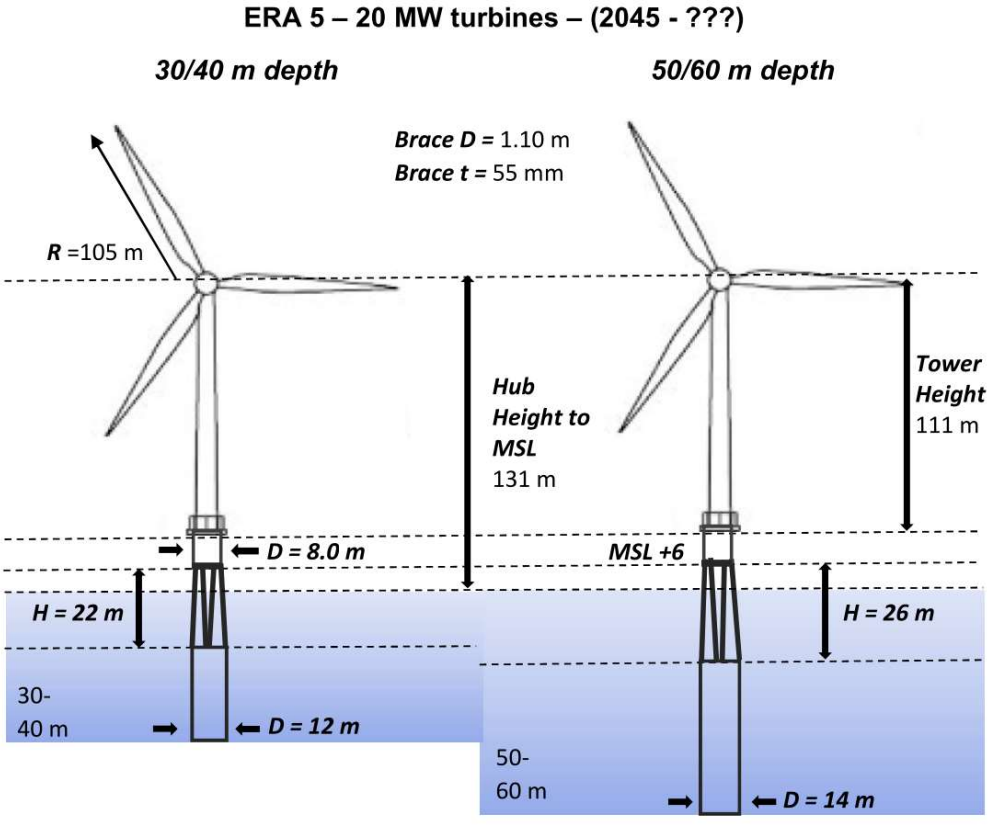

Figure 10-8: Era 5 standardized Hybrid Monopile

To quantify the effect of this standardization on the structure effectiveness, the design procedure used for the original optimization is repeated, but for the reduced set of variable combinations, and without any iteration of the brace dimensions. To quantify the degree of overdesign which may result from this standardization, an additional output was added to the results file, designated the brace design factor. This factor is calculated as:

$$brace\ design\ factor = minim \left(\frac{1.0}{Unity_{brace}}, \frac{FatigueLife_{brace}}{50.0} \right)$$

A resulting factor less than 1.0 would indicate that the brace fails either the ULS or FLS check, a perfectly optimized brace would result in a factor value of 1.0. The degree to which the design factor exceeds 1.0 can be used to give an indication of how "overdesigned" the standardized brace is. An identical procedure was performed to analyse the data for the concrete-fill design option and determine the appropriate brace dimensions for each era.

10.8. Updated simulations with era definitions

Having reduced the original 480 variable combinations to a set of 40 each for the hollow-steel and concrete filled options, the design procedure was repeated. The full results summary for each remaining variable combination, for both material options, can be found in Appendix A. Tables 28 and 29 provide an overview of the most critical variables, averaged for each turbine era.

Table 28: Key results per era - standardized Hybrid Monopile

ERA	*Ref. D/t*	*Hybrid D/t*	*Shell Reduction*	*Weight Reduction*	*Mudline life (R)*	*Mudline Life (H)*	*Cost Diff*	*Unity*
8	107	145	25.9%	20.0%	69	100	-13.3%	0.91
10	102	131	21.2%	16.3%	53	67	-5.8%	1.00
12	91	138	33.8%	31.2%	51	63	-28.8%	0.99
15	125	174	30.2%	25.1%	83	92	-21.9%	0.87
20	122	158	24.2%	18.5%	66	69	-11.3%	0.81

Table 29: Key results per era - CFST Hybrid Monopile

ERA	*Ref. D/t*	*Hybrid D/t*	*Shell Reduction*	*Weight Reduction*	*Steel Reduction*	*Mudline life (R)*	*Mudline Life (H)*	*Unity*
8	107	153	32.9%	19.1%	33.0%	69	108	0.91
10	102	138	26.4%	10.1%	28.2%	53	80	1.00
12	91	142	36.1%	23.9%	37.7%	51	62	0.99
15	125	170	26.5%	14.0%	28.6%	83	106	0.87
20	122	161	24.3%	10.1%	25.6%	66	74	0.81

The results show that the design appears to scale well when adjusted to accommodate larger turbines. Even without fully optimizing the brace dimensions, monopile shell reductions of 20-30% are consistently achievable, without a reduction in the expected fatigue life. Though the addition of the concrete-fill to the members provides an additional shell reduction of approximately 7%, it is unclear whether this additional reduction is worth the added uncertainty associated with that option, and the added challenge to design a connection detail that can accommodate the concrete.

The results for the reduced set of simulations also provide insight into the choice of base diameter. Though the selected base diameters for each era allow for a structurally sufficient design in each case, fatigue life estimates for the 12 MW era appear to be skewed slightly downward due to the continued use of a 10-meter diameter base in shallower waters, and results for the 15 MW era show the inverse, skewed slightly in the opposite direction, due to what may be a premature implementation of the 14.0-meter base diameter. Sensitivity of the era based results to changes in the selected base diameter could be an interesting area for additional research.

11. Conclusions and recommendations

11.1. Remaining Challenges

The initial design concept, optimized for a specific test site, not only proved suitable for the selected test location, but allow for the extrapolation of the design to several alternative test sites, and projected future turbine sizes. Despite this early success, technical and non-technical challenges remain that must be addressed further after the conclusion of this project to ensure that to market product is still innovative, reliable, and profitable.

Though the results of the mathematical models are promising, to realistically consider deploying a Hybrid Monopile requires that the two concurrently developed technologies, the underwater interface and alternative welded joint, reach a greater level of maturity. It is known that the welded connection will be the critical location for ULS stress and fatigue assessment, which for the purposes of this report was neglected. Similarly, though the analytical assessments of the concrete-filled member option show promise, the logistics of sealing the concrete into the tube, and any undesirable interactions that may occur between the concrete and steel surface have not been investigated.

Transport and installation of the complete structure must also be considered, especially for larger configurations. Behemoth monopiles of a similar scale may be floating into place, but the open brace area and weight distribution of the Hybrid would make this difficult or impossible. Even with the substantial weight reduction from a standard monopile to a Hybrid Monopile configuration, complete structure dimensions for deeper water sites may exceed to the crane capacity, hammer size, or lifting reach of current installation vessels. The ability of the structure to endure driving forces during the installation process is somewhat irrelevant until the installation fleet advances to match the required capacity.

From a non-technical perspective, existing legislative and certification frameworks may slow the advancement of the Hybrid concept to market. Determining which design standards the structure is governed by, or how to apply the current procedures when it is less than intuitive, needs to be considered. Unique designed often carry a high-risk perception, which can make interfacing with regulatory bodies even more challenging. Standards that are not well adapted to deeper environments or larger structures – may have to wait for codes to “catch up” to the design accurately quantify the viability.

11.2. Recommendation for future work

Further investigation of the Hybrid Monopile support structure should focus on dynamic finite-element analyses. The results presented in this report, are promising, and using for comparing the relative benefits of several design options, but are based on simplified design methods, and in some cases, outdated design codes. It is also unclear at this stage how the connection detail between the brace members and monopile shell will affect the applicability of the common design standards.

Additionally, the extrapolation of wind forcing data was based on some significant assumptions regarding the evolution of offshore wind turbines over the next few decades. Projections for the timeline of turbine growth, and the size of those future turbines, vary substantially between sources, and it is recommended

that any future work into scaling the Hybrid Monopile for theoretical future turbines, be done in collaboration with a major turbine manufacturer to validate the critical assumptions affecting the support structure design. With respect to environmental loading, as previously mentioned, future work should also include more randomization of wind loads, additional time series simulations, and consider better discretization of sea states near the structure frequency.

11.3. Conclusion

As the offshore industry continue along its current path towards larger turbines and harsher environments, cost reduction will remain a high priority, with support structures offering the largest opportunity to make financial strides. A standardized Hybrid Monopile is an attractive option, both structurally and commercially. This thesis has taken the first steps towards a detailed design and numerical validation of the concept. Using industry design codes, Matlab-based modeling, and finite-element modelling, the Hybrid monopile has been shown to be advantageous both structurally and commercially compared to the traditional monopile, noticeably reducing the effects of wave loading, under both extreme and fatigue sea state conditions and allowing for reduced structure weight. Pending continued research, the Hybrid Monopile may play a key role in unlocking new and profitable wind farm development opportunities around the world for decades to come.

References

[1] Arany, L., Bhattacharya S., Macdonald, J.H.G., Hogan, S.J. (2016) Closed form solution of Eigen frequency of monopile supported offshore wind turbines in deeper waters incorporating stiffness of substructure and SSI**.** *Soil Dynamics and Earthquake Engineering*, *83*, 18–32

[2] Adhikari, S., Arany, L., Bhattacharya S., Macdonald, J.H.G., Hogan, S.J. (2015) An analytical model to predict the natural frequency of offshore wind turbines on three-spring flexible foundations using two different beam models. *Soil Dynamics and Earthquake Engineering, 74,* 40-45.

[3] ANSYS, Inc. (2017) ANSYS Mechanical APDL Modelling and Meshing Guide.

[4] Seidel, M. 6 MW turbines with 150M+ rotor diameter – what is the impact on substructure. *In: Conference Proceedings DEWEK 2012.* Bremen, DEWI 2012.

[5] Breton, S.P., Moe, G. (2009) Status, plans and technologies for offshore wind turbines in Europe and North America. *Renewable Energy, 34,* 646-654.

[6] Ragan, P., Manuel, L. (2007) Comparing estimates of wind turbine fatigue loads using time-domain and spectral methods. *Wind Engineering, Vol 31,* 83-89.

[7] Seidel, M. Substructures for offshore wind turbines: Current trends and developments. In: *Festchrift Peter Schaumann.* Hannover 2014.

[8] Seidel, M. (2014) Wave induced fatigue loads: Insights from frequency domain calculations. *Stahlbau, 83,* 535-541. doi:10.1002/stab.201410184

[9] Seidel, M. Feasibility of monopiles for large offshore wind turbines. *In: Conference Proceedings DEWEK 2010. Bremen:* DEWI 2010.

[10] Vestas Wind Systems A/S. (2016). V164 8.0 MW takes offshore to the next level. Product brochure.

[11] Det Norske Veritas (DNV), Design of offshore wind turbine structures, *DNV-OS-j101,* ed. Norway, 2013.

[12] Bhattacharya, S. (2014) Challenges in design of foundations for offshore wind turbines. *Institution of Engineering and Technology.* 1-9. doi:10.1049/etr.2014/0041

[13] Adhikari, S., Bhattacharya, S. (2012) Dynamic analysis of wind turbine towers on flexible foundations. *Shock Vib., 2012,* pp. 37-56.

[14] Van der Tempel, J., Salzmann, D.J. Cerda (2006) Aerodynamic damping in the design of support structures for offshore wind turbines. TU Delft.

[15] Tempel J. van der et al. (2005) Frequency domain calculation of offshore wind turbine response to wind and wave loads. DUWIND. *In: Proceedings of the Copenhagen Offshore Wind Conference,* Copenhagen 2005.

[16] Patel, V., Lande, P.S. (2016) Analytical behaviour of concrete filled steel tubular columns under axial compression. *International Journal of Engineering Research, 5(3),* 629-632.

[17] Groen, Rolf. (2016) Concept feasibility of 10 m Hybrid Monopile. *Project/MEMO No. 16023-MEM-RG-002.* Enersea

[18] National Oceanic and Atmospheric Agency, National Data Buoy Center. www.ndbc.noaa.gov. *Accessed*: May 2017.

[19] Xiamuxi, A., Hasegawa, A. (2012) A study on axial compressive behaviours of reinforced concreted filled tubular steel columns. *Journal of Constructional Steel Research, 76,* 144-154.

[20] Elremaily, A., Azizinamini, A. (2002) Behavior and strength of circular concrete-filled tube columns. *Journal of Constructional Steel Research, 58,* 1567-1591.

[21] Liang, Q.Q. (2011) High strength circular concrete-filled steel tubular slender beam-columns: Part 1: Numerical analysis. *Journal of Constructional Steel Research, 67,* 164-171.

[22] Van der Tempel, J. (2006) Design of support structures for offshore wind turbines. PhD thesis. TU Delft.

[23] International Electrotechnical Commission. IEC-61400-1. (2005).

[24] Kuhn, M. (2001) Dynamics and design optimization of OWECS, *Institute for Wind Energy,* Delft University of Technology.

[25] Pierson, W.J. Moskowitz, L. (1964) A proposed spectral form for fully developed wind seas based on similarity theory of S.A. Kitaigorodskij, *Journal of Geophysical Research,* 5181-5190.

[26] Morison, J.R. et al (1950) The fore exerted by surface waves on piles. *Petroleum Transactions,* AIME.

[27] MacCamy, R. and Fuchs, R. (1954) Wave forces on piles: A diffraction theory. *US Army Corps of Engineering, Beach Erosion Board:* Technical Memorandum No. 69.

[28] Fischer, T., de Vries, W., and Schmidt, B., (2010) Upwind Design Basis. *UPWIND*, Stuttgart, Germany.

[29] Ziegler. L, (2015) Probabilistic estimation of fatigue loads on monopile-based offshore wind turbines – application to sensitivity assessment & clustering optimization for support structure cost reduction. *Msc Thesis, EWEM*, NTNU & TU Delft.

[30] Dirlik, T. (1985). Application of computers in fatigue analysis. *PhD thesis*, *University of Warwick*, England.

[31] Borgman, L.E. (1965). The spectral density for ocean wave forces. *ASCE,* Santa Barbara specialty conference.

[32] Yeter, B., Garbatov, Y., Soares, C. (2014) Spectral fatigue assessment of an offshore wind turbine structure under wave and wind loading. *Developments in Maritime Transportation and Exploitation of Sea Resources,* 425-432.

[33] Gavriluta, C., Spataru, S. Mosincat, I., Citro, C. et al (2012) Complete methodology on generating realistic wind speed profiles based on measurements. In: *International Conference on Renewable Energies and Power Quality, 1(10).* Spain 2012.

[34] Branlard, E. (2010) Generation of time series from a spectrum. Technical University Denmark. *National Laboratory for Sustainable Energy.* February 2010.

[35] DNV Group GL (2014), Offshore wind: A manifest for cost reduction.

[36] American Petroleum Institute (API). Recommended Practice for Planning, Designing, and Constructing Fixed Offshore Platforms – Working Stress Design (2A-WSD). *American Petroleum Institute*, Washington, D.C., 2005.

[37] NORSOK standard N-004: Design of steel structures. *Rev 2.* February 2013.

[38] Det Norske Veritas. DVD-RP-C205: Environmental Conditions and Environmental Loads. (2014).

[39] Det Norske Veritas. DNV-RP-C202: Buckling Strength of Shells. (2013).

[40] R. Bergmann, C. Matsui, C. 1Meinsma, D. Dutta. (1995) Design guide for concrete filled hollow section columns under static and seismic loading. *Construction with Hollow Steel Sections 5.*

[41] Arany, L., Bhattacharya, S., Macdonald, J., Hogan, S.J. (2017) *Design of monopiles for offshore wind turbines in 10 steps.* Soil Dynamics and Earthquake Engineering, *Vol 92*, 126-152.

[42] European Union (2004) Eurocode No. 4: Design of Composite Steel and Concrete Structures, Part 1, 1.1: General Rules and Rules for Buildings, ENV 1994-1-1:1992.

[43] Heermans, K.W., Peeringa, J.M. Future XL monopile foundation design for a 10 MW wind turbine in deep water. *ECN-E-16-069,* December 2016.

[44] Campione, G., La Mendola, L., Sanpaolesi, L., Scibilia, G., Zingone, G. (2002) Behavior of fibre reinforced concrete-filled tubular columns in compressions. *Materials and Structures, Vol. 35*, July 2002, pp 332-337.

[45] Faltinsen, O. (1990) Sea loads on ships and offshore structure. *Cambridge University Press*, 1990.

[46] Twidell, J., Gaudiosi, G. (2009) Offshore wind power. *Multi-Science Publishing Company*.

[47] Germanischer Lloyd (2000), Rules & Guidelines 2000: IV Non-marine Technology – Regulations for the Certification of (Offshore) *Wind Energy Conversion Systems.*

[48] Jonkman, J. (2016) FAST User Manual. Version 8.16a. *National Renewable Energy Lab*.

[49] Jonkman, J. (2015) FAST theory manual. Version 8.15. *National Renewable Energy Lab*.

[50] Dykes, K., Platt, A., Guo, Y., Ning, A. et al. (2014), Effect of Tip-Speed Contracts on the Optimized Design of a Wind Turbine. *National Renewable Energy Lab*.

[51] de Vries, W.E. (2014) Foundation Pile Analysis Tool. *Section Offshore Renewables, TU Delft.*

[52] Phone meeting – DONG Energy, 28 June 2017.

[53] Kvaleid. J. Wave load sensitivity of XXL monopiles. In: *Offshore Foundations IQPC London.* February 2017.

[54] Heermans, K.W. (2014) Evaluation of modal parameters and damping from the structural response of an offshore wind substructure. *ECN-WIND-2014-242*.

[55] Keijdener, C., Jarquin-Laguna, A. (2016). W3.L1&2: Discretization in Space. *Introduction to Computational Dynamics for Offshore Structures. Lecture Note*s. TU Delft.

[56] Hanswille, G., (2008) Composite Columns: Dissemination of information for training workshop. *In proceedings. Eurocodes - Background and Applications*: Brussels 2008.

[57] Wind and wave frequency distributions for sites around the British Isles. (2002) *Prepared by Fugro GEOS for the Health and Safety Executive.*

[58] Det Norske Veritas. DNVGL-RP-C203, Fatigue Design of Offshore Steel Structures. April 2016.

[59] van der Male, P. (2017) MANUAL – Tool: Support Structures. *TU Delft*.

[60] International Standard (2007), NEN-ISO-19902

[61] Tsuchiya, Y., Yasuda T. (1981) A New Approach to Stokes Wave Theory. *Kyoto University*.

[62] Bureau of Ocean Energy Management (2016). *Offshore Wind Energy.*

[63] Ziegler, L., Voormeeren, S., Schafhirt, S., Muskulus, M. (2015) Sensitivity of Wave Fatigue Loads on Offshore Wind Turbines under varying Site Conditions. *In: Proceedings from the 12th Deep Sea Offshore Wind R&D Conference. EERA DeepWind'2015.*

[64] European Wind Energy Association. (2016). The European offshore wind industry – key trends and statistics 2015.

[65] European Wind Energy Association. (2015). The European offshore wind industry – key trends and statistics 2014.

[66] European Wind Energy Association. (2014). The European offshore wind industry – key trends and statistics 2013.

[67] European Wind Energy Association. (2013). The European offshore wind industry – key trends and statistics 2012.

[68] Wang K., Chunyan, J., Hongxiang, X., Tang, W. (2016) Fatigue damage characteristics of a semisubmersible-type floating offshore wind turbine at tower base. *Journal of Renewable and Sustainable Energy, 8, 053307;* doi: http://dx.doi.org/10.1063/1.4964366

[69] Det Norske Veritas. DVD-RP-C204: Design Against Accidental Loads. (2014).

[70] Turbine Calculator Tool Manual (2016). *In: Course Materials: Offshore Wind Farm Design. TU Delft*.

Appendix A

RESULTS SUMMARY: HOLLOW STEEL MEMBERS FOR ALL ERAS

Locations	Depths	Bases	Tops	Turbine	braceDs	braceTs	bLength	RefShell	Ref D/t	HybShell	Hyb D/t	ShellRed	RefWeigh	HybWeigh	WeightRed	RefShear	HybShear	ShearREd	RefMom	HybMom	MomRed	Ref Flife	Hyb Flife	LifeDiff	% Wind [R	% Wave [R]	% Wind [H	% Wave [H]	RefPile	HybPile	Pilediff	CostRef	CostHyb	Cost Diff	bFlife	Unity	BDF
1	30	10	6.5	8	0.95	0.048	22.14	0.059	169	0.050	200	15.3%	919.0	909.2	1.1%	9.2	6.6	28%	429.2	364.5	15%	147.4	137.1	-10.2	81.7	18.3	98.6	1.4	28	33	-5	$1,343,208	$1,175,797	12.5%	154	0.84	1.19
2	30	10	6.5	8	0.95	0.048	22.14	0.059	169	0.050	200	15.3%	919.0	909.2	1.1%	11.6	8.1	30%	474.3	381.6	20%	161.1	230.2	69.1	51.0	49.0	94.8	5.2	28	33	-5	$1,343,208	$1,175,797	12.5%	264	0.86	1.16
1	40	10	6.5	8	0.95	0.048	22.14	0.091	110	0.056	180	38.9%	1599.3	1058.1	33.8%	12.9	12.0	7%	563.7	498.2	12%	59.8	68.9	9.1	18.9	81.1	73.5	26.5	30	29	1	$1,545,591	$2,017,579	-30.5%	413	0.91	1.10
2	40	10	6.5	8	0.95	0.048	22.14	0.063	159	0.050	200	20.6%	1206.2	982.8	18.5%	12.9	10.5	18%	565.0	469.8	17%	66.4	136.2	69.8	21.3	78.7	78.2	21.8	30	29	1	$1,431,545	$1,523,715	-6.4%	996	0.90	1.11
2	50	10	6.5	8	0.95	0.048	26.12	0.167	60	0.091	110	45.6%	2935.4	1738.0	40.8%	12.8	12.2	5%	625.8	558.9	11%	31.9	50.4	18.4	7.9	92.1	57.6	42.4	30	30	0	$2,517,600	$3,663,368	-45.5%	252	0.94	1.07
1	50	10	6.5	8	0.95	0.048	26.12	0.167	60	0.125	80	25.1%	3016.2	2260.8	25.0%	14.6	12.3	16%	678.7	559.5	18%	20.9	59.4	38.5	5.7	94.3	36.1	63.9	32	30	2	$3,287,081	$3,760,370	-14.4%	225	0.94	1.07
1	60	10	6.5	8	0.95	0.048	26.12	0.167	60	0.167	60	0.2%	3300.9	3339.1	-1.2%	14.7	13.1	11%	761.1	650.7	15%	9.6	52.6	42.9	3.7	96.3	23.6	76.4	32	31	1	$4,752,505	$4,090,531	13.9%	4063	0.94	1.06
2	60	10	6.5	8	0.95	0.048	26.12	0.143	70	0.077	130	46.2%	2898.5	1710.7	41.0%	14.1	10.8	23%	762.4	601.9	21%	51.5	67.5	16.1	7.4	92.6	46.3	53.7	32	30	2	$2,425,985	$3,595,171	-48.2%	1650	0.93	1.07
1	30	10	6.5	10	1.00	0.050	22.14	0.059	169	0.053	190	10.8%	919.0	894.7	2.6%	9.7	7.3	25%	518.1	458.5	12%	74.8	69.9	-4.9	89.4	10.6	99.1	0.9	28	28	0	$1,340,701	$1,175,797	12.3%	138	0.93	1.08
2	30	10	6.5	10	1.00	0.050	22.14	0.059	169	0.050	200	15.3%	943.5	866.1	8.2%	12.1	8.9	27%	563.3	477.0	15%	97.7	111.9	14.2	64.7	35.3	96.2	3.8	30	28	2	$1,295,139	$1,205,243	6.9%	239	0.95	1.06
1	40	10	6.5	10	1.00	0.050	22.14	0.100	100	0.071	140	28.6%	1724.9	1326.1	23.1%	13.4	12.8	4%	657.9	603.1	8%	55.6	68.6	13.0	30.8	69.2	81.4	18.6	30	31	-1	$1,938,116	$2,175,412	-12.2%	383	1.01	0.99
2	40	10	6.5	10	1.00	0.050	22.14	0.071	141	0.050	200	29.6%	1324.7	1013.3	23.5%	13.4	11.3	15%	659.2	573.6	13%	68.2	72.3	4.2	34.5	65.5	84.6	15.4	30	30	0	$1,471,814	$1,672,190	-13.6%	969	1.00	1.00
1	50	10	6.5	10	1.00	0.050	26.12	0.167	60	0.143	70	14.5%	3016.2	2589.4	14.2%	15.2	13.1	13%	778.1	673.3	13%	18.6	54.9	36.3	10.6	89.4	50.2	49.8	32	31	1	$3,759,490	$3,760,370	0.0%	213	1.05	0.95
2	50	10	6.5	10	1.00	0.050	26.12	0.167	60	0.125	80	25.1%	3016.2	2312.8	23.3%	13.3	13.1	2%	725.2	672.8	7%	28.4	60.8	32.4	15.0	85.0	66.4	33.6	32	31	1	$3,353,802	$3,760,370	-12.1%	234	1.05	0.96
2	60	10	6.5	10	1.00	0.050	26.12	0.167	60	0.091	110	45.6%	3300.9	2026.2	38.6%	14.7	11.7	20%	867.1	720.8	17%	71.1	57.3	-13.8	15.5	84.5	52.5	47.5	32	32	0	$2,867,698	$4,090,531	-42.6%	1942	1.04	0.96
2	30	10	8	12	1.05	0.053	22.11	0.073	137	0.050	200	31.5%	1218.4	976.9	19.8%	15.3	9.4	38%	726.8	577.3	21%	83.5	62.1	-21.4	62.9	37.1	98.3	1.7	32	30	2	$1,452,514	$1,516,168	-4.4%	874	1.00	1.00
1	30	10	8	12	1.05	0.053	22.11	0.073	137	0.067	150	8.7%	1350.5	1151.6	14.7%	12.2	7.9	35%	663.7	559.4	16%	62.3	64.7	2.5	88.4	11.6	99.5	0.5	30	29	1	$1,739,355	$1,674,658	3.7%	531	0.99	1.01
1	40	10	8	12	1.05	0.053	22.11	0.143	70	0.083	120	41.7%	2606.9	1602.7	38.5%	16.3	13.5	17%	840.2	712.9	15%	54.9	57.8	2.8	25.6	74.4	89.5	10.5	32	32	0	$2,357,635	$3,208,982	-36.1%	663	1.08	0.92
2	40	10	8	12	1.05	0.053	22.11	0.091	110	0.059	170	35.4%	1842.2	1236.8	32.9%	16.3	11.9	27%	842.4	678.5	19%	57.4	67.3	9.9	28.5	71.5	91.7	8.3	32	31	1	$1,805,262	$2,271,637	-25.8%	1857	1.05	0.95
1	50	12	8	12	1.05	0.053	26.16	0.200	60	0.109	110	45.5%	4526.6	2591.2	42.8%	20.7	16.9	18%	1022.7	828.9	19%	30.9	50.1	19.2	6.9	93.1	52.7	47.3	35	34	1	$3,727,438	$5,675,057	-52.3%	427	0.94	1.06
2	50	12	8	12	1.05	0.053	26.16	0.200	60	0.100	120	50.0%	4526.6	2412.5	46.7%	18.1	16.8	7%	947.2	828.2	13%	50.8	65.1	14.3	10.3	89.7	71.2	28.8	35	34	1	$3,466,655	$5,675,057	-63.7%	478	0.94	1.06
1	60	12	8	12	1.05	0.053	26.16	0.200	60	0.171	70	14.3%	5056.4	4359.1	13.8%	20.7	18.1	13%	1139.2	955.5	16%	16.6	68.0	51.4	5.4	94.6	36.4	63.6	37	35	2	$6,163,159	$6,291,040	-2.1%	7697	0.94	1.06
2	60	12	8	12	1.05	0.053	26.16	0.133	90	0.075	160	43.6%	3609.8	2140.1	40.7%	20.0	15.0	25%	1142.8	890.4	22%	51.8	69.2	17.4	10.8	89.2	60.0	40.0	37	34	3	$3,011,767	$4,503,651	-49.5%	2745	0.94	1.07
1	30	12	8	15	1.10	0.055	22.19	0.073	164	0.060	200	17.8%	1439.4	1262.0	12.3%	13.4	9.7	28%	759.0	662.1	13%	131.0	98.4	-32.6	90.6	9.4	99.3	0.7	33	31	2	$1,876,468	$1,852,752	1.3%	361	0.86	1.17
2	30	12	8	15	1.10	0.055	22.19	0.073	164	0.060	200	17.8%	1439.4	1279.6	11.1%	16.8	11.8	30%	824.0	685.1	17%	172.8	180.9	8.1	67.3	32.7	97.3	2.7	33	32	1	$1,897,669	$1,852,752	2.4%	606	0.88	1.14
1	40	12	8	15	1.10	0.055	22.19	0.100	120	0.067	180	33.3%	2311.9	1610.0	30.4%	18.7	17.4	7%	954.8	853.0	11%	58.9	61.1	2.3	33.9	66.1	86.5	13.5	35	34	1	$2,328,481	$2,931,350	-25.9%	838	0.94	1.06
2	40	12	8	15	1.10	0.055	22.19	0.073	164	0.060	200	17.8%	1689.5	1491.6	11.7%	18.6	15.3	18%	956.8	812.9	15%	88.0	130.8	42.8	39.3	60.7	87.8	12.2	35	34	1	$2,152,081	$2,152,818	0.0%	2344	0.92	1.08
1	50	14	8	15	1.10	0.055	26.27	0.175	80	0.100	140	42.9%	4673.6	2863.6	38.7%	23.0	21.5	6%	1141.8	998.2	13%	55.2	61.1	6.0	10.7	89.3	49.4	50.6	38	37	1	$4,065,274	$6,002,035	-47.6%	666	0.84	1.19
2	50	14	8	15	1.10	0.055	26.27	0.140	100	0.082	170	41.2%	3768.3	2440.6	35.2%	20.2	21.4	-6%	1063.7	997.2	6%	54.5	63.2	8.7	16.1	83.9	69.0	31.0	36	37	-1	$3,458,074	$4,850,847	-40.3%	746	0.84	1.20
1	60	14	8	15	1.10	0.055	26.27	0.233	60	0.133	105	42.8%	6574.4	4161.3	36.7%	23.5	23.1	2%	1277.7	1158.1	9%	47.3	55.1	7.8	6.8	93.2	32.5	67.5	38	38	0	$5,809,116	$8,340,107	-43.6%	8374	0.84	1.19
2	60	14	8	15	1.10	0.055	26.27	0.097	144	0.070	200	27.8%	3156.2	2384.2	24.5%	22.5	19.0	16%	1277.3	1072.8	16%	60.2	89.3	29.1	17.0	83.0	56.9	43.1	38	37	1	$3,320,522	$4,028,636	-21.3%	4999	0.83	1.21
1	30	12	8	20	1.20	0.060	22.19	0.073	164	0.067	180	8.7%	1439.4	1441.6	-0.2%	14.0	10.8	23%	884.9	799.2	10%	74.6	67.6	-7.0	94.7	5.3	99.4	0.6	33	33	0	$2,135,889	$1,852,752	13.3%	721	0.80	1.24
2	30	12	8	20	1.20	0.060	22.19	0.073	164	0.060	200	17.8%	1474.7	1344.7	8.8%	17.4	13.0	25%	949.9	825.1	13%	113.9	99.8	-14.1	78.4	21.6	97.5	2.5	35	33	2	$1,985,257	$1,895,154	4.5%	1163	0.82	1.22
1	40	12	8	20	1.20	0.060	22.19	0.109	110	0.086	140	21.4%	2475.5	2045.2	17.4%	19.3	18.7	3%	1086.9	1008.3	7%	56.5	66.3	9.8	48.2	51.8	89.7	10.3	35	36	-1	$2,958,024	$3,138,119	-6.1%	1606	0.88	1.14
2	40	12	8	20	1.20	0.060	22.19	0.075	160	0.060	200	20.0%	1858.9	1556.7	16.3%	19.2	16.5	14%	1088.9	966.0	11%	67.5	74.4	6.9	52.2	47.8	90.8	9.2	35	35	0	$2,239,669	$2,358,533	-5.3%	4517	0.86	1.16
1	50	14	8	20	1.20	0.060	26.27	0.187	75	0.112	125	40.1%	4946.0	3245.1	34.4%	23.6	22.8	3%	1279.9	1163.9	9%	59.7	53.2	-6.6	18.4	81.6	57.8	42.2	38	38	0	$4,601,619	$6,351,097	-38.0%	1274	0.79	1.27
2	50	14	8	20	1.20	0.060	26.27	0.147	95	0.097	145	34.3%	4031.0	2870.2	28.8%	20.8	22.7	-9%	1201.8	1163.0	3%	53.1	55.6	2.6	25.5	74.5	72.9	27.1	38	38	0	$4,064,952	$5,179,040	-27.4%	1426	0.79	1.27
1	60	14	8	20	1.20	0.060	26.27	0.233	60	0.165	85	29.3%	6732.9	5135.6	23.7%	24.1	24.4	-1%	1421.9	1333.9	6%	45.7	61.6	15.9	12.0	88.0	39.4	60.6	40	39	1	$7,163,813	$8,530,231	-19.1%	17671	0.79	1.27
2	60	14	8	20	1.20	0.060	26.27	0.097	144	0.076	185	22.0%	3222.4	2622.1	18.6%	23.1	20.2	13%	1421.6	1244.3	12%	55.6	69.7	14.1	28.9	71.1	63.6	36.4	40	38	2	$3,649,330	$4,108,090	-12.6%	7184	0.78	1.28

TUDelft

RESULTS SUMMARY: CFST MEMBERS FOR ALL ERAS

Location	Depths	Bases	Tops	Turbines	braceD	braceT	Length	Ref Shell	Ref D/t	Hyb Shell	Hyb D/t	Shell Red	Ref Weight	Hyb Weight	Hyb Steel Weight	Weight Red	Hyb Concrete Weight	Steel Weight Red	Ref Shear	Hyb Shear	Shear Red	Ref Moment	Hyb Moment	Moment Red	Ref Flife	Hyb Flife	% Wind [R]	% Wave [R]	% Wind [H]	% Wave [H]	Ref Pile	Hyb Pile	Pile Diff	Brace Flife	Unity
2	30	10	6.5	8	0.85	0.028	22.14	0.059	169	0.050	200	15.3%	919.0	1039.7	813.1	11.5%	227	-13.1	11.1	7.7	31%	466.4	371.4	20%	238	257	59.5	99.9	40.5	0.1	28	33	-5	4570	0.83
2	40	10	6.5	8	0.85	0.028	22.14	0.059	169	0.050	200	15.3%	1088.1	1101.0	874.5	19.6%	227	-1.2	12.3	10.1	18%	553.6	454.4	18%	93	183	10.9	96.6	89.1	3.4	30	28	2	17655	0.87
1	40	10	6.5	8	0.85	0.028	22.14	0.083	120	0.050	200	39.8%	1491.2	1113.3	886.7	40.5%	227	25.3	12.3	11.5	7%	552.3	481.3	13%	69	76	5.8	94.7	94.2	5.3	30	29	1	7057	0.88
2	50	10	6.5	8	0.85	0.028	26.12	0.167	60	0.083	120	50.1%	2935.4	1771.9	1504.1	48.8%	268	39.6	12.2	11.7	5%	611.8	536.1	12%	46	63	1.0	83.1	99.0	16.9	30	30	0	3918	0.90
1	50	10	6.5	8	0.85	0.028	26.12	0.167	60	0.091	110	45.6%	3016.2	1887.4	1619.6	46.3%	268	37.4	14.0	11.7	16%	662.4	536.6	19%	29	50	0.5	48.3	99.5	51.7	32	30	2	3458	0.90
2	60	10	6.5	8	0.85	0.028	26.12	0.125	80	0.063	160	50.0%	2595.5	1606.4	1338.7	48.4%	268	38.1	13.5	10.4	23%	743.2	579.1	22%	57	68	0.9	63.1	99.1	36.9	32	30	2	211	0.90
1	60	10	6.5	8	0.85	0.028	26.12	0.167	60	0.143	70	14.5%	3300.9	3056.6	2788.8	15.5%	268	7.4	14.0	12.6	10%	741.6	624.5	16%	13	63	0.2	17.8	99.8	82.2	32	31	1	546	0.91
1	30	10	6.5	10	0.90	0.030	22.14	0.059	169	0.050	200	15.3%	919.0	1018.7	765.2	16.7%	254	-10.9	9.3	6.9	26%	511.8	449.1	12%	99	63	98.9	100.0	1.1	0.0	28	28	0	2687	0.85
2	30	10	6.5	10	0.90	0.030	22.14	0.059	169	0.050	200	15.3%	943.5	1018.7	765.2	18.9%	254	-8.0	11.6	8.4	28%	555.4	465.1	16%	140	123	82.0	99.9	18.0	0.1	30	28	2	4969	0.87
2	40	10	6.5	10	0.90	0.030	22.14	0.059	169	0.050	200	15.3%	1181.6	1166.0	912.4	22.8%	254	1.3	12.8	10.8	16%	647.8	555.7	14%	66	93	26.8	98.5	73.2	1.5	32	30	2	19912	0.92
1	40	10	6.5	10	0.90	0.030	22.14	0.083	120	0.063	160	24.7%	1531.9	1336.5	1082.9	29.3%	254	12.8	12.8	12.3	5%	646.5	583.3	10%	58	67	23.1	97.9	76.9	2.1	32	30	2	7517	0.94
2	50	12	6.5	10	0.90	0.030	26.21	0.120	100	0.071	170	41.2%	2624.6	1901.0	1601.3	39.0%	300	27.6	14.3	15.7	-10%	727.4	695.0	4%	58	65	3.7	82.9	96.3	17.1	33	33	0	6272	0.80
1	50	12	6.5	10	0.90	0.030	26.21	0.150	80	0.086	140	42.9%	3176.2	2191.1	1891.4	40.5%	300	31.0	16.2	15.8	3%	780.4	695.8	11%	55	62	1.2	40.4	98.8	59.6	33	33	0	5599	0.80
2	60	12	6.5	10	0.90	0.030	26.21	0.086	140	0.060	200	30.2%	2263.1	1874.1	1574.4	30.4%	300	17.2	15.9	14.0	12%	875.8	750.9	14%	66	91	3.4	59.3	96.6	40.7	35	33	2	439	0.80
1	60	12	6.5	10	0.90	0.030	26.21	0.200	60	0.109	110	45.5%	4616.2	2989.9	2690.2	41.7%	300	35.2	16.6	17.0	-2%	877.9	813.5	7%	53	50	0.6	16.6	99.4	83.4	35	34	1	588	0.81
1	30	10	8	12	0.95	0.032	22.11	0.073	137	0.067	150	8.7%	1218.4	1320.2	1038.1	14.8%	282	-8.4	11.7	7.5	36%	656.4	550.5	16%	84	66	98.9	100.0	1.1	0.0	32	29	3	9651	0.90
2	30	10	8	12	0.95	0.032	22.11	0.073	137	0.050	200	31.5%	1218.4	1136.2	854.1	29.9%	282	6.7	14.7	9.0	39%	717.6	566.3	21%	119	65	78.0	100.0	22.0	0.0	32	29	3	18581	0.91
2	40	10	8	12	0.95	0.032	22.11	0.077	130	0.056	180	27.8%	1635.1	1361.1	1079.0	34.0%	282	16.8	15.7	11.4	27%	829.4	662.2	20%	61	69	19.5	99.6	80.5	0.4	32	31	1	39383	0.96
1	40	10	8	12	0.95	0.032	22.11	0.111	90	0.077	130	30.7%	2138.9	1659.1	1376.9	35.6%	282	22.4	15.7	13.0	17%	827.2	694.8	16%	51	59	16.1	99.4	83.9	0.6	32	31	1	13526	0.99
2	50	12	8	12	0.95	0.032	26.16	0.171	70	0.086	140	49.9%	3966.8	2327.6	1994.2	49.7%	333	41.3	17.4	16.3	6%	930.6	807.1	13%	52	62	1.9	92.5	98.1	7.5	35	34	1	8724	0.87
1	50	12	8	12	0.95	0.032	26.16	0.200	60	0.100	120	50.0%	4526.6	2606.3	2272.9	49.8%	333	42.4	19.9	16.4	18%	1003.5	807.9	19%	43	63	0.7	70.7	99.3	29.3	35	34	1	7641	0.87
2	60	12	8	12	0.95	0.032	26.16	0.109	110	0.060	200	45.0%	3084.2	2000.7	1667.3	45.9%	333	35.1	19.2	14.5	24%	1120.1	869.4	22%	51	64	2.1	84.5	97.9	15.5	37	34	3	371	0.86
1	60	12	8	12	0.95	0.032	26.16	0.200	60	0.133	90	33.3%	5056.4	3683.3	3349.9	33.8%	333	27.2	19.9	17.6	12%	1116.2	931.4	17%	22	59	0.4	36.1	99.6	63.9	37	35	2	861	0.86
1	30	12	8	15	1.00	0.033	22.19	0.073	164	0.060	200	17.8%	1439.4	1452.9	1139.3	20.8%	314	-0.9	13.0	9.4	28%	751.5	653.5	13%	168	101	99.1	100.0	0.9	0.0	33	31	2	7575	0.78
2	30	12	8	15	1.00	0.033	22.19	0.073	164	0.060	200	17.8%	1474.7	1470.5	1157.0	21.5%	314	0.3	16.2	11.4	30%	814.6	674.2	17%	238	194	84.1	100.0	15.9	0.0	35	32	3	14546	0.80
2	40	12	8	15	1.00	0.033	22.19	0.073	164	0.060	200	17.8%	1689.5	1664.9	1351.4	20.0%	314	1.5	18.0	14.8	18%	943.3	796.6	16%	131	161	34.5	99.0	65.5	1.0	35	33	2	55470	0.84
1	40	12	8	15	1.00	0.033	22.19	0.086	140	0.063	190	26.6%	2055.5	1738.0	1424.5	30.7%	314	15.4	18.0	16.8	6%	941.4	835.1	11%	67	68	28.9	98.8	71.1	1.2	35	34	1	19198	0.86
2	50	14	8	15	1.00	0.033	26.27	0.117	120	0.074	190	37.0%	3245.7	2430.7	2060.2	36.5%	371	25.1	19.5	20.9	-7%	1046.7	975.8	7%	55	69	5.3	91.8	94.7	8.2	36	36	0	15186	0.77
1	50	14	8	15	1.00	0.033	26.27	0.156	90	0.088	160	43.9%	4228.9	2754.9	2384.3	43.6%	371	34.9	22.2	21.0	5%	1122.1	976.9	13%	63	65	2.0	57.9	98.0	42.1	38	36	2	13320	0.77
2	60	14	8	15	1.00	0.033	26.27	0.085	165	0.070	200	17.6%	2856.3	2608.7	2238.1	21.6%	371	8.7	21.7	18.6	15%	1253.8	1051.7	16%	69	133	5.6	76.1	94.4	23.9	38	37	1	1378	0.76
1	60	14	8	15	1.00	0.033	26.27	0.215	65	0.104	135	51.8%	6127.6	3560.7	3190.1	47.9%	371	41.9	22.7	22.6	0%	1253.9	1133.7	10%	56	50	0.7	32.7	99.3	67.3	38	38	0	981	0.77
1	30	12	8	20	1.05	0.035	22.19	0.073	164	0.067	180	8.7%	1474.7	1631.1	1286.0	12.8%	345	-10.6	13.6	10.1	25%	877.5	783.5	11%	92	69	99.7	100.0	0.3	0.0	35	33	2	8518	0.81
2	30	12	8	20	1.05	0.035	22.19	0.073	164	0.060	200	17.8%	1474.7	1535.5	1190.4	19.3%	345	-4.1	16.8	12.2	27%	940.5	805.2	14%	152	107	94.3	100.0	5.7	0.0	35	33	2	16307	0.82
2	40	12	8	20	1.05	0.035	22.19	0.073	164	0.060	200	17.8%	1689.5	1747.5	1402.4	17.0%	345	-3.4	18.6	15.6	16%	1075.3	936.2	13%	94	90	60.2	99.6	39.8	0.4	35	35	0	62153	0.86
1	40	12	8	20	1.05	0.035	22.19	0.092	130	0.080	150	13.0%	2170.3	2104.2	1759.1	18.9%	345	3.0	18.6	17.7	5%	1073.4	975.6	9%	60	69	57.5	99.4	42.5	0.6	35	35	0	21408	0.88
2	50	14	8	20	1.05	0.035	26.27	0.122	115	0.090	155	26.0%	3442.8	2907.9	2500.0	27.4%	408	15.5	20.1	21.8	-8%	1184.9	1124.0	5%	54	67	15.6	95.7	84.4	4.3	38	37	1	16961	0.80
1	50	14	8	20	1.05	0.035	26.27	0.165	85	0.097	145	41.5%	4438.9	3089.0	2681.1	39.6%	408	30.4	22.8	21.9	4%	1260.2	1125.0	11%	69	56	6.9	78.4	93.1	21.6	38	38	0	14922	0.80
2	60	14	8	20	1.05	0.035	26.27	0.085	165	0.070	200	17.6%	2914.6	2688.7	2280.7	21.7%	408	7.8	22.3	19.4	13%	1398.1	1205.8	14%	59	89	14.9	89.4	85.1	10.6	40	38	2	1153	0.80
1	60	14	8	20	1.05	0.035	26.27	0.215	65	0.122	115	43.4%	6274.0	4152.9	3745.0	40.3%	408	33.8	23.3	23.5	-1%	1398.1	1289.4	8%	56	53	2.5	54.8	97.5	45.2	40	39	1	5259	0.80